



ISSN 1028-8546

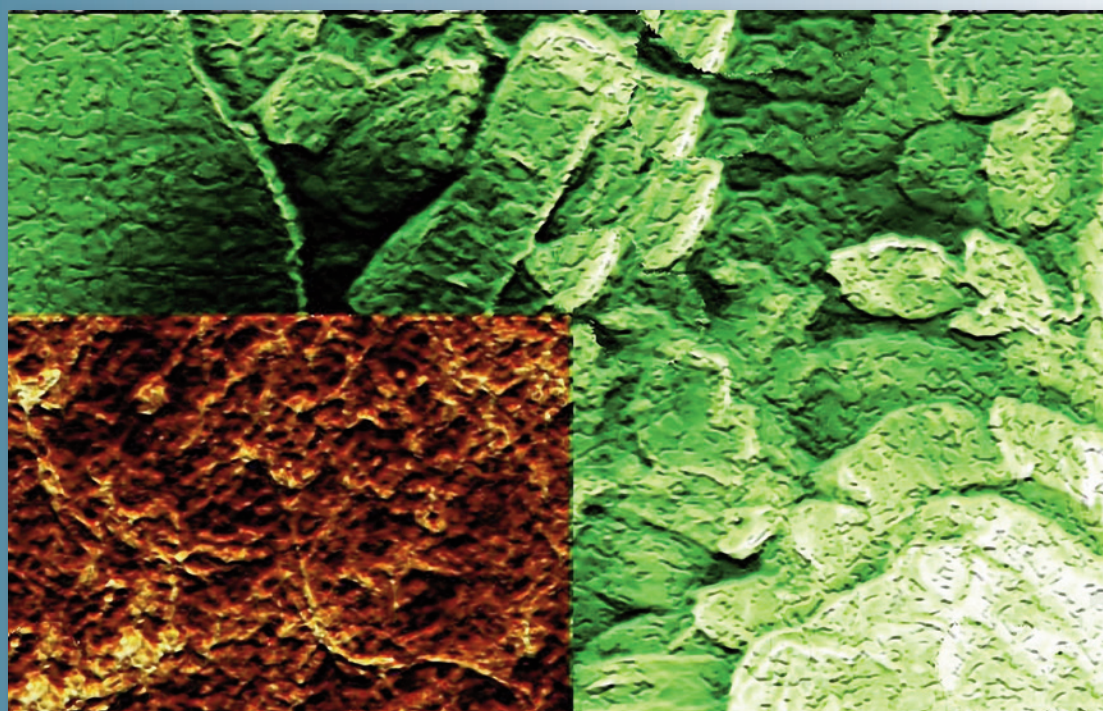
Volume XXII, Number 1

Section: En

April, 2016

# Azerbaijan Journal of Physics

# Fizika



[www.physics.gov.az](http://www.physics.gov.az)

G.M. Abdullayev Institute of Physics  
Azerbaijan National Academy of Sciences  
Department of Physical, Mathematical and Technical Sciences

## *Azerbaijan Journal of Physics*

# *FIZIKA*

*G.M.Abdullayev Institute of Physics  
Azerbaijan National Academy of Sciences  
Department of Physical, Mathematical and Technical Sciences*

### **HONORARY EDITORS**

Arif PASHAYEV

### **EDITORS-IN-CHIEF**

Nazim MAMEDOV

Chingiz QAJAR

### **SENIOR EDITOR**

Talat MEHDIYEV

### **INTERNATIONAL REVIEW BOARD**

Ivan Scherbakov, Russia  
Kerim Allahverdiyev, Azerbaijan  
Mehmet Öndr Yetiş, Turkey  
Gennadii Jablonskii, Buelorussia  
Rafael Imamov, Russia  
Vladimir Man'ko, Russia  
Eldar Salayev, Azerbaijan  
Dieter Hochheimer, USA  
Victor L'vov, Israel  
Vyacheslav Tuzlukov, South Korea

Majid Ebrahim-Zadeh, Spain  
Firudin Hashimzadeh, Azerbaijan  
Anatoly Boreysho, Russia  
Mikhail Khalin, Russia  
Hasan Bidadi, Tebriz, East Azerbaijan, Iran  
Natiq Atakishiyev, Mexico  
Maksud Aliyev, Azerbaijan  
Arif Hashimov, Azerbaijan  
Javad Abidinov, Azerbaijan  
Bagadur Tagiyev, Azerbaijan

Tayar Djafarov, Azerbaijan  
Talat Mehdiyev, Azerbaijan  
Vali Huseynov, Azerbaijan  
Ayaz Baramov, Azerbaijan  
Tofiq Mammadov, Azerbaijan  
Salima Mehdiyeva, Azerbaijan  
Shakir Nagiyev, Azerbaijan  
Rauf Guseynov, Azerbaijan  
Almuk Abbasov, Azerbaijan  
Yusif Asadov, Azerbaijan

### **TECHNICAL EDITORIAL BOARD**

Senior secretary Elmira Akhundova, Nazli Guseynova, Sakina Aliyeva,  
Nigar Akhundova, Elshana Aleskerova, Rena Nayimbayeva

### **PUBLISHING OFFICE**

131 H.Javid ave, AZ-1143, Baku  
ANAS, G.M.Abdullayev Institute of Physics

Tel.: (99412) 539-51-63, 539-32-23  
Fax: (99412) 447-04-56  
E-mail: [jophphysics@gmail.com](mailto:jophphysics@gmail.com)  
Internet: [www.physics.gov.az](http://www.physics.gov.az)

It is authorized for printing:

Published at "SƏRQ-QƏRB"  
17 Ashug Alessger str., Baku  
Typographer : Aziz Gulaliyev

Sent for printing on: \_\_.\_\_. 201\_  
Printing approved on: \_\_.\_\_. 201\_  
Physical binding: \_\_\_\_\_  
Number of copies: \_\_\_\_\_ 200  
Order: \_\_\_\_\_

## TECHNOLOGY OF ALUMINUM DEEP PURIFICATION BY ZONE MELTING METHOD USING ULTRASONIC WAVES

A.I. NADJAFOV, R.R. BABAYEVA

*Institute of Physics of NAS of Azerbaijan*

*AZ 1143, H.Javid ave.,131, Baku*

[a.najafov@mail.ru](mailto:a.najafov@mail.ru)

The method of three-stage zone melting for deep purification of A85 (99,85% Al) aluminum mark is used. The ultrasonic waves for intensification of liquid mixing and diffusion processes during zone melting are used. The optimal parameters of ultrasonic waves are defined by experimental methods. It is shown that the use of ultrasonic waves with frequency 20 kHz and intensity  $0,4\text{Vt/cm}^2$  allows us to increase the aluminum purity level up to 99,999% in comparison with usual process of zone melting.

**Keywords:** purification, aluminum, zone melting

**PACS:** 81.05 Rm

### INTRODUCTION

The modern industry can't be imagined without aluminum and its melts. The aluminum and its melts are used in many industry fields: aircraft building, shipbuilding, transport, technique, building, cable production, oil and chemical industries and etc.

The purer aluminum is mainly widely applied in electronics from electrolytic capacitors up to microprocessors, in cryoelectronics, cryomagnetics, in critical parts of chemical equipment working in corrosion-active mediums or at extremely low temperatures, modern radar engineering and especially critical products of atomic power engineering.

The purity of industrial aluminum (99,5 – 99,8%) in series of cases isn't enough, as the higher degree of industrial aluminum purification obtained by electrolysis for these goals, is required. Note that last time many investigations concerning to different methods of aluminum purification (electrolytic, crystallized, distillation) are carried out [1-3]. The zone purification method of pure aluminum obtaining is the more practical, industrial and effective one [2-7].

The zone melting principle is in multiple passing of molten zone along aluminum ingot. These impurities can be divided into three groups by values of distribution coefficients  $K=C_{sol}/C_{liq}$  (where  $C_{sol}$  is impurity concentration in solid phase and  $C_{liq}$  is impurity concentration in liquid one) which essentially define the purification efficiency from impurities. The impurities decreasing the aluminum melting point are to first group. They have  $K<1$ , locate in molten zone and are transferred by it to ingot end part at zone melting. Ga, Sn, Be, Sb, Ca, Th, Fe, Co, Ni, Ce, Te, Ba, Pt, Au, Bi, Pb, Cd, In, Na, Mg, Cu, Si, Ge, Zn belong to these impurities.

The impurities increasing the aluminum melting point are to second group. They have  $K>1$  and locate in solid part (heading) of ingot. Nb, Ta, Cr, Ti, Mo, V are to these impurities.

The impurities with distribution coefficient which is very close to 1 (Mn, Sc) belong to the third group. These impurities aren't practically scavenged at aluminum zone melting.

According to [8-9] the purification efficiency from impurities at zone melting depends on redistribution coefficient  $K=C_{sol}/C_{liq}$ . However, the crystallization front travel rate and liquid stirring rate before crystallization front essentially influence on impurity distribution between liquid and solid phases at crystallization. It may be shown that for impurity having  $K<1$  the moving crystallization front displaces the impurities with bigger velocity than their diffusions from liquid in growing crystal.

By this reason the region with increased impurity concentration forms before the crystallization front. The thickness of this layer, composition and impurity concentration determine the parameters of diffusion impurity from liquid in growing crystal. The thickness of this layer also depends on hydrodynamics of liquid metal and usually has the size about  $10^{-3}$ - $10^{-5}$  m. The diffusion coefficient has the value in limits of  $10^{-9}$  -  $10^{-8}$   $\text{m}^2/\text{sec}$ , although their values aren't determined for all impurity types. The component excess ( $K<1$ ) will increase in case of diffusion difficulty in liquid phase on crystallization front during zone travel. The forming solid phase is depleted by this component. This leads to solid phase crystallization not from the main phase but from the layer neighbouring to crystallization front in which impurity concentration increases that leads to decrease of impurity separation effect. Thus, the difficulty of the component diffusion in liquid state prevents to the separation or impurity purification at zone melting. The ultrasound is applied in works [5, 8-10] with the aim of impurity concentration decrease on crystal-melt boundary and intensity increase of impurity diffusion into melt depth. It is established that influence of ultrasonic waves of determined frequency increases the intensity of impurity diffusion into liquid depth and increases the purification efficiency [8-11]. The ultrasonic waves are used by us for the intensification of mixing of liquid and diffusion processes during aluminum zone melting. We give below the results of carried out experiments.

### EXPERIMENTAL PART

Taking into consideration the aluminum chemical activity, the aluminum zone melting is carried out in

crucibles, which are inertial ones for the process. The high melting point and inertia to cleanable material are the main requirements to the crucible material. The carbon-base glass is the more stable material to aluminum melt. The carbon-base glass has the high thermostability in inertial gas and vacuum up to 3000° C. The high-quality polished surface, maximal chemical stability and low acceptance by metal melts and other substances are the main advantages of carbon-base glass crucibles and boats. The boats from carbon-base glass of SIGRADUR mark (Germany) are used in our experiments.

The aluminum purification process is begun from metal surface purification on oxide film. Note that aluminum oxide forms the additional crystallization centers at solidification of a metal that leads to disturbance of impurity redistribution effect between ingot solid part and its molten zone. Besides, the aluminum oxide is the impurity active adsorbent that also badly influences on metal purification.

The metal ingots are cut by crucible sizes and the surface is etched by 10% hydrochloric acid at 60°C. Further, the ingots are washed in distilled water, swilled out by deionized water and dried in vacuum. Later, the metal degassing is carried out. The metal degassing before its zone melting is carried out by the way of melting and its endurance in vacuum  $10^{-3}$  mm of mercury.

Further, the preliminary aluminum vacuum remelting is carried out. The melting and endurance of aluminum in vacuum ( $\sim 10^{-3}$  mm of mercury) in melted state at 720-740°C essentially decrease (3-5times) the content of hydrogen and magnesium and zinc impurities [12-13]. The quantity of zinc impurity after the endurance during 2 hours is decreased in 4 times. Besides, the average gas content of initial aluminum 0,21cm<sup>3</sup>/100gr after endurance during one hour is decreased in more than 2 times and after 8 hours the gas content in metal isn't practically revealed. However, as analyses show the quantity of impurities of cuprum, iron and silicon aren't practically changed after melting and long endurance of aluminum.

The scheme of installation used for aluminum purification is shown in fig.1. It is carried out in horizontal variant. The device consists of two independent purification reactors. Each channel has three successive cascades of heaters. The two independent material purification processes in quantity 50-250gr in temperature interval 50-1050°C are carried out on the device.

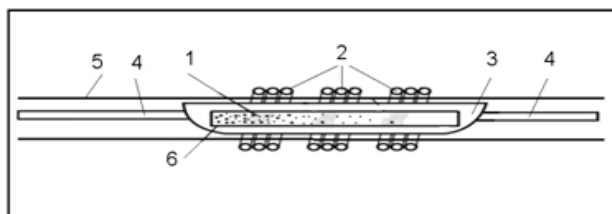


Fig.1. The scheme of installation of cascade zone melting.

1 is crucible with substance; 2 are heaters; 3 is vacuum-degassed ampoule; 4 are holders; 5 is guide tube.

The two similarly prepared and evacuated quartz ampoules with aluminum put into carbon-base glass crucibles are loaded on the device. It is shown in fig. 2.

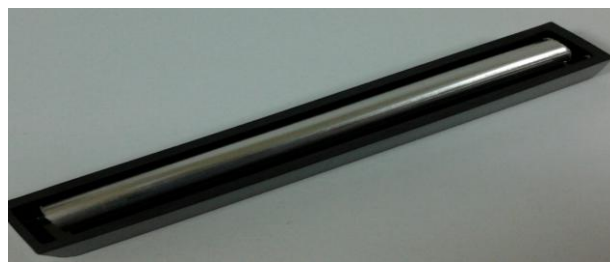


Fig.2. The boat from carbon-base glass for aluminum zone melting.

The prepared ampoules with substances are put into guide quartz tubes of the device. The heating resistors forming the narrow ingot molten zone, moving towards with heater, shift outside along ampoule with aluminum ingot. The zone temperature is 750° C. The device heaters are defended with oval screen allowing concentrating the thermal radiation inside the heating ring. Note that furnace electric resistances are comfortable ones in work and don't require the complex equipment for electric power supply and process regulation. The aluminum ingot length is near 250mm, the molten zone width is 30-35mm, the velocity of zone displacement is chosen on the base of experiment results and it is 20mm/h. The cascade passing number along ingot is 10.

The aluminum zone purification without external influences is carried out in first reactor. The same process of zone recrystallization is carried in second channel by ultrasonic oscillation influence. For this two soldered adaptations parallel each other are in ampoule ends and the ultrasonic vibrator sensor is attached to one of these ampoule ends. The ultrasonic generator of G3-109series with piezoelectric transformer is used in our case. The other end of this ampoule is put into device holder clutch filled by smooth silicon material of «Elstolux-M» mark for damping of ultrasonic oscillations.

The ultrasonic oscillation frequency is chosen in interval 15-20kHz with the fact that the cavitation threshold increase in melt takes place at frequency increasing more than 20kHz, i.e. minimal value of sound pressure enough for cavitation appearance at given conditions increases. The intensive mixing of melt components doesn't take place at frequency less 15kHz. The intensity of radiation is chosen in interval 0,3 - 0,5 Vt/cm<sup>2</sup>. Our results allow us to recommend the frequency given intervals and ultrasonic oscillation intensities.

The analyses of obtained ingot purity are carried out after 10 cycles of zone melting. The initial and end parts (approximately 20% of ingot length) are cut off the each ingot. The samples which are pressed up to necessary dimensions are cut off midsection of ingots (60% of length) and analyses on roentgen-fluorescent spectrometer "S8 TIGER" are carried out on them. The analysis results of purified aluminum ingots are given in Table1.

According to results given in table 1 the main substance purity increases almost on one order after 10 passes of aluminum purification of mark A85 on installation of cascade zone melting. Moreover, the content of Fe and Si decreases almost in 30 times, Zn decreases almost on one order and cuprum quantity decreases in three times. The titanium impurity quantity



becomes less roentgen-fluorescent sensitivity value ( $10^{-4}\%$ ).

The change of impurity content in aluminum after zone melting and after zone melting with application of ultrasonic waves is compared in table 1. These data show the significant decrease of impurity content in aluminum after application of ultrasonic waves during zone melting. According to carried out analyses the quantity of content of Fe and Si impurities in aluminum ingot decreases up to  $3 \cdot 10^{-4}\%$  level and content of Cu and Zn impurities

decreases up to  $2 \cdot 10^{-4}\%$  that exceeds the aluminum purity level obtained using the zone melting after 10 cycles of three-cascade zone purification and application of ultrasonic waves with frequency 20kHz and intensity  $0,4 \text{ Vt/cm}^2$ .

The obtained positive result of aluminum purification level by zone melting method with application of ultrasonic waves is the result of intensification of liquid mixing and diffusion processes during zone melting processes.

Table 1.

The analysis results of aluminum ingots purified by zone melting method.

Purification method	Chemical composition and impurity quantity in %					Main substance in %
	Fe	Si	Cu	Zn	Ti	
Initial aluminum of mark A85*	0,08	0,06	0,01	0,02	0,008	99,83%
Three-cascade zone melting (10 passes)	0,003	0,002	0,003	0,002	-	99,99%
Three-cascade zone melting (10 passes) with ultrasonic wave application	0,0003	0,0003	0,0002	0,0002	-	99,999%

\* Chemical composition of initial aluminum is given according to data State Standard RF 1069-2001.

## CONCLUSION

1. The deep purification of aluminum of A85 (99,85%Al) mark is carried out by three-cascade zone melting method. It is shown that the application of ultrasonic waves with frequency 20kHz and intensity  $0,4 \text{ Vt/cm}^2$  allows us to increase on one order the purity level of purified aluminum up to level 99,999% of main substance.

2. The method can be used in industrial production for obtaining of essentially pure aluminum.

## ACKNOWLEDGEMENTS

The work is supported by fund of "Scientific-investigation programs" of Azerbaijan National Academy of Sciences.

- |  |  |
|--|--|
| <p>[1] <i>Khimicheskaya entsiklopediya</i>. Gl. red. I.L. Knunyants. 1988, Izd. Sov. Entsikl. Moskva, (in Russian)</p> <p>[2] <i>A.I. Belyayev, G.E. Volfson, G.I. Lazarev</i>. Poluchenie chistogo alyumunuya. M., Metallurgiya, 1967, 268s. (in Russian)</p> <p>[3] <i>A.I. Belyayev</i>. Metallurgiya lyogkikh metallov. 1970, M, Metallurgiya, 368 s. (in Russian)</p> <p>[4] <i>Allyuminievie splavi. Metallovedenie allyuminiya i ego splavov. Алюминиевые сплавы. Spravochnik</i>. Otvet. red. I.N. Fridlyander. M, Metallurgiya, 1983, 277 s. (in Russian)</p> <p>[5] <i>V.N. Vigdorovich</i>. Ochistka metallov i poluprovodnikov kristallizatsiey. M, 1969. 296 s. (in Russian)</p> <p>[6] <i>S.G. Marayev i dr.</i> Trudi VAMI, 1970, vip. 680, s. 110. (in Russian)</p> <p>[7] <i>N. Parr</i>. Zonnaya ochistka i yeyo tekhnika. M., Metallurgizdat, 1963, 211 s. (in Russian)</p> | <p>[8] <i>Povishenie effektivnosti tekhnologicheskikh protsesov v pole akusticheskikh kolebaniy</i>. Sb. Pod redaktsiyey N.N. Khavskogo. M, 1981. (in Russian)</p> <p>[9] <i>O.V. Abramov</i>. Vliyaniye ultrazvuka na protses zonnay plavki naftalina. Akusticheskiy jurnal, 1967, t.13, v.2, s.161-168. (in Russian)</p> <p>[10] <i>B.A. Agranat, V.I. Bashkirov, Yu.I. Kitaygorodskiy</i>. Kavitatsionnoe razrusheniye poverkhnostnykh plyonok v akusticheskom pole pri povishennom staticheskom davlenii. Akusticheskiy jurnal, 1967, t. 13, s. 283-285. (in Russian)</p> <p>[11] <i>B.A. Agranat, M.N. Dubrovkin i dr.</i> Osnovi fiziki i tekhniki ultrazvuka. M., Visshaya shkola, 1987, 352 s. (in Russian)</p> <p>[12] <i>Allyuminievie splavi. Primeneniye allyuminievikh splavov. Spravochnoe rukovodstvo. Redaktsionnaya kollegiya I.V. Gorinin i dr.</i>, Moskva, "Metallurgiya", 1978. (in Russian)</p> <p>[13] <i>Allyuminiy. Svoystva i fizicheskoe metallovedenie. Spravochnik. J.E. Khetch</i>. "Metallurgiya", 1989. (in Russian)</p> |
|--|--|

Received: 20.11.2015

## IR SPECTRA OF (Ni, Zn) FERRITE MICROPOWDERS

Sh.N. ALIYEVA, A. KERIMOVA, T.R. MEHDIYEV

G.M. Abdullayev Institute of Physics of NAS, Azerbaijan

AZ-1143, Baku, H. Javid ave., 131

The results of experimental investigations of reflection spectra in near and far regions of infrared wavelength range of  $Ni_{1-x}Zn_xFe_2O_4$  ferrite micropowders with different content of Ni and Zn in them are given. The intensity dependence of IR-spectrum of these ferrites on concentration change of cations  $Fe^{2+}$  and  $Fe^{3+}$  in ferrite different compositions is established. The dependence of dispersion on ferrite compositions is determined and the presumptive interpretation of observable spectral structures is given.

**Keywords:** IR spectra, ferrite micropowders

**PACS:** 78.55.Am

## 1. INTRODUCTION

In spite of the fact that *Ni-Zn* ferrites are well-known, appeared in former century, they are of big scientific interest that is shown in big amount scientific publications, among which the investigations of IR and Raman spectra take the especial place. In works [1-2], devoted to investigations of neutron small-angle scattering, Mossbauer effect, EPR micropowder spectra and AFM magnetic profiles of thin films of  $Ni_{1-x}Zn_xFe_2O_4$  ferrites with different content of *Ni* and *Zn*, the effects connected with not only two types of B-sublattice ordering but additional magnetic ordering and declination of sublattice spin collinearity are revealed. To interpret these peculiarities it was necessary to study in detail IR and Raman spectra. The results of experimental investigations of IR spectra of  $Ni_{1-x}Zn_xFe_2O_4$  ferrite micropowders under consideration are given in present work.

## 2. SAMPLE PREPARATION

All compositions of ferrites are obtained by the way of high-temperature synthesis of ultrapure powders of  $ZnO$ ,  $NiO$ ,  $Fe_2O_3$  compounds. The synthesized  $Ni_{1-x}Zn_xFe_2O_4$  compositions are annealed at temperature  $960^\circ$  and grinded into micropowders with grid sizes about 20nm. The quality of synthesized compositions of ferrite micropowders is controlled by roentgen micropowder diffractograms on XRDD8 ADVANCE, Bruker, Germany and also by Raman spectra. The roentgen investigation results are published in [4]. IR spectra of  $Ni_{1-x}Zn_xFe_2O_4$  ferrites of  $x=0; 0,25; 0,4; 0,5; 0,6; 0,75; 1,0$  compositions are studied on infrared Fourier-spectrometer Vertex70 (Bruker, Germany) with attachment of diffuse reflection in vacuum camera in spectral range from  $4000\text{cm}^{-1}$  up to  $50\text{cm}^{-1}$ , the standard spectral resolution is better than  $0,5\text{cm}^{-1}$  (fig.1-2). The positions of genetically connected spectral lines determining the form of main absorption maximums are given in table 1. The sample temperature in all experimental investigations is equal to 300K.

The positions of spectral lines from experimental works [3,4,5] are also given in table 1.

By analysis of obtained spectra, it is established that their profiles have the complex structure and not only shift but the splitting into spectral components in process of "x" change are observed.

## 3. EXPERIMENTAL RESULTS AND DISCUSSION

It is well known that IR active triply degenerate modes of  $F_{1u}$  symmetry type should be observed in IR spectra of spinel reflection, i.e. oscillations are asymmetric ones in respect of inversion center and symmetric ones in respect of twofold axis or vertical reflection planes ( $\sigma_v$ ). On the other hand, masses of *Fe*, *Ni* and *Zn* ions consisting in the composition of investigated ferrite significantly exceed the oxygen ion mass. Moreover, the oxygen ion oscillations in respect of metal heavy ions practically don't influence on positions of heavy ions whereas heavy ion oscillations influence on oxygen ion ones. The shift of oxygen ion can take place either along the  $C_3$  triad axis order or perpendicular to it [5]. In first case the  $F_{1u}^1$  oscillation of  $Me^{2+} - O - 3Me^{3+}$  bond (where  $Me^{2+}$  is octahedral cation and  $3Me^{3+}$  are three tetrahedral cations) is observed. The high-frequency spectral band corresponds to this oscillation. In second case, the  $F_{1u}^2$  oscillation of  $Me^{3+} - O - 2Me^{3+}$  bond, in which only octahedral cations take part, is observed. The low-frequency spectral band corresponds to this oscillation. The cation oscillations  $F_{1u}^3$  ( $Me^{3+} - Me^{3+}$ ) and  $F_{1u}^4$  ( $Me^{2+} - Me^{2+}$ ) in respect of each other take part at more low frequencies and have the weak intensities. As the frequencies of these oscillations is determined by dimensions and ion masses then the shift of spectral lines towards to low frequencies will be observed at exchange of  $Fe^{2+}$  on  $Zn^{2+}$  or  $Ni^{2+}$  (masses of  $Zn^{2+}$  and  $Ni^{2+}$  ions are bigger than  $Fe^{2+}$  mass) in tetrahedral and octahedral spinel fragments  $Fe^{2+}Fe_2^{3+}O_4$ . The three wide bands associated with lattice oscillations of *Fe-O*, *Ni-O* and *Zn-O* bonds are observed for all ferrite compositions in IR spectrum long-range region. The obtained frequency values in IR spectrum long-range region for micropowders of all compositions of  $Ni_{1-x}Zn_xFe_2O_4$  ferrites are given in table 1. The light lines in tables correspond to spectral lines along compositions from  $NiFe_2O_4$  up to  $ZnFe_2O_4$ :  $604\text{-}542\text{cm}^{-1}$ ;  $425\text{-}388\text{cm}^{-1}$ ;  $249\text{-}241\text{ cm}^{-1}$ , which according to agreed classification are interpreted as oscillations of  $F_{1u}^1, F_{1u}^2, F_{1u}^3$  and  $F_{1u}^4$  symmetry type correspondingly. The presence of thin structure in IR spectra of investigated compositions and absorption maximum positions are established as a result of multiply carried out experiments.

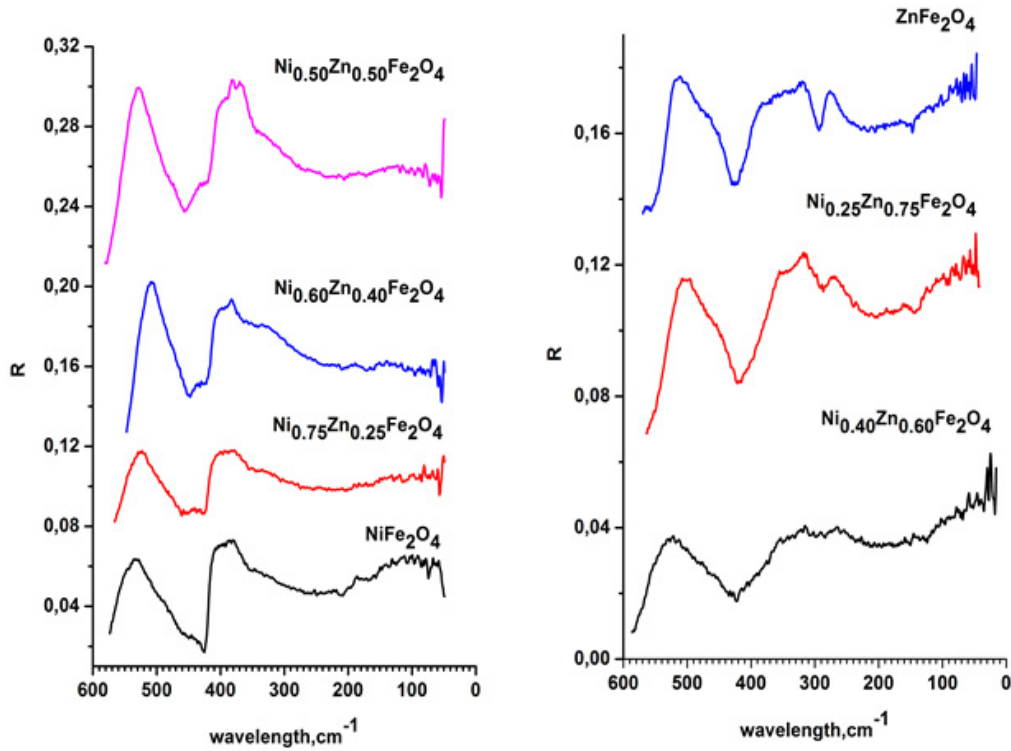


Fig. 1. IR spectra of  $Ni_{1-x}Zn_xFe_2O_4$  ferrites in FIR mode.

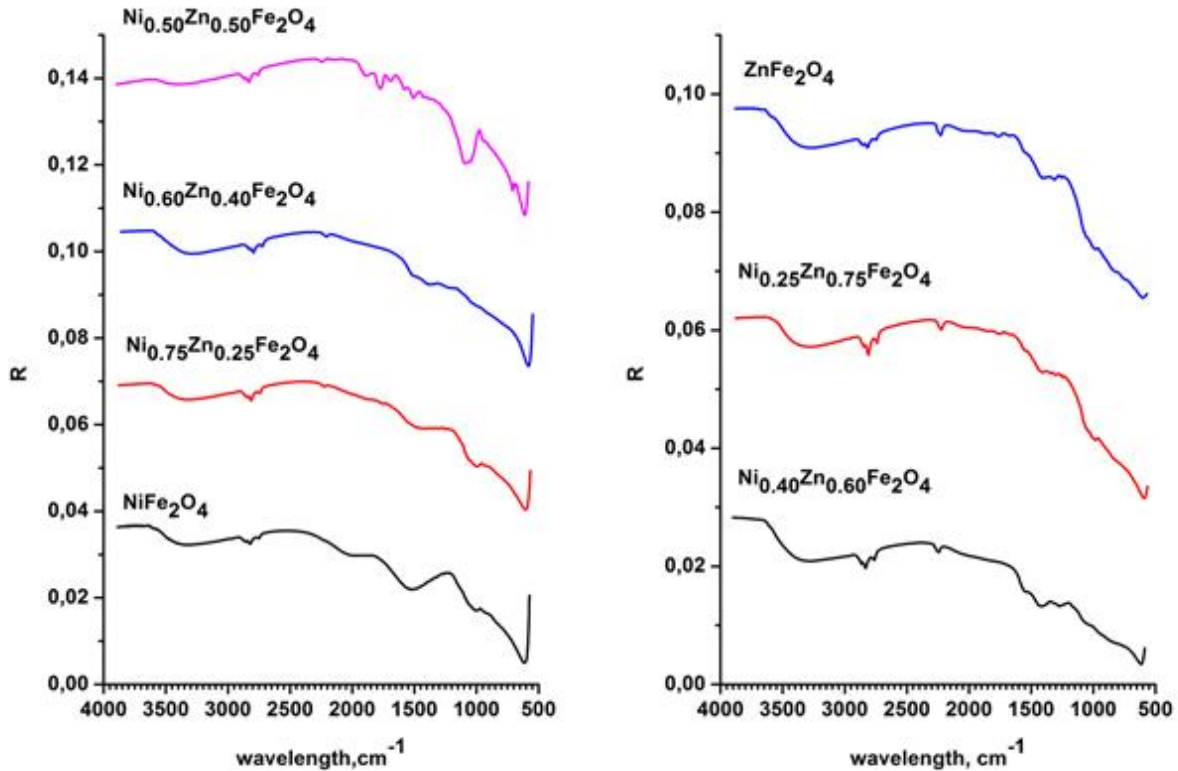


Fig. 2. IR spectra of  $Ni_{1-x}Zn_xFe_2O_4$  ferrites in MIR mode,  $x(Ni)=1;0.75; 0.6;0.5;0.4; 0.25; 0$

The absorption bands in frequency region with maximums in neighborhood of  $430\text{ cm}^{-1}$  and  $545\text{ cm}^{-1}$  which present themselves the oscillation combined bands of  $Fe-O$  valence bonds in octahedral positions with  $Zn^{2+}$  ions in nearest coordination surrounding  $Fe-O-Zn$

evidence on spinel structure formation, for example in  $ZnFe_2O_4$ . The absence or presence of wide intensive absorption bands at  $3440\text{ cm}^{-1}$  and  $1630\text{ cm}^{-1}$  shows the presence of adsorbed water or OH-groups [6, 7]. This fact is confirmed by absorption bands at  $823\text{ cm}^{-1}$  and

1045cm<sup>-1</sup>, which are to deformation oscillations of Zn–O–H and Fe–O–H bonds.

The role of Ni and Zn cation repropotioning in different compositions of  $Ni_{1-x}Zn_xFe_2O_4$  ferrites in formation of their IR spectra is established by experimental investigations. As it follows from experiments the shift, the appearance of new spectral lines and disappearance of “old” ones are observed in IR spectra of investigated compositions of  $Ni_{1-x}Zn_xFe_2O_4$  ferrites depending on  $Ni^{2+}$  and  $Zn^{2+}$  cation inclusions. The dependences of obtained IR spectra of investigated  $Ni_{1-x}Zn_xFe_2O_4$  compositions are easily interpreted within framework of model taking under consideration the changes of  $Fe^{3+}$ [3] and  $Fe^{2+}$ [8] cation concentrations in different ferrite compositions (fig.1). The comparison of these data with intensity taken for the example of experimental spectra band 425cm<sup>-1</sup> shows on the fact that decrease of  $Fe^{2+}$  and  $Fe^{3+}$  contents in ferrite composition leads to the decrease of absorption intensity of this band in IR spectra. The change of  $Fe^{2+}$  and  $Fe^{3+}$  contents in ferrite compositions obviously indicates on the change of “jump” electron number and consequently on the change of indirect exchange interaction [9]. Thus, the interconnection of elementary cell “a” parameter and shift of normal oscillation frequency at isomorphous substitutions becomes understandable one. The indirect exchange interaction value is necessary to take under the consideration besides the changes of elementary cell “a” parameter in calculations of shift of normal oscillation frequency at isomorphous substitutions. As it has to be expected, the shift of IR spectra of  $Ni_{1-x}Zn_xFe_2O_4$  ferrites

towards to low frequencies is observed depending on  $Ni^{2+}$  and  $Zn^{2+}$  cation repropotioning. It is established that spectral line 604cm<sup>-1</sup> observed in  $NiFe_2O_4$  spectrum depending on “x” and interpreted as oscillations of  $Me^{2+} - O - 3Fe^{3+}$  bonds ( $Me$  is Ni or Zn ions) related to  $F_{1u}^1$  symmetry type shifts to 542cm<sup>-1</sup> position in  $ZnFe_2O_4$ . At detail consideration, it is established that the form of considered spectral line has the complex structure. The shift and splitting of spectral components forming the given line profile is revealed in inclusion process of  $Ni^{2+}$  and  $Zn^{2+}$  ions in ferrite composition (see table 1). The profile change in neighborhood and maximums themselves from 425cm<sup>-1</sup> ( $NiFe_2O_4$ ) up to 388cm<sup>-1</sup> ( $ZnFe_2O_4$ ) more obviously demonstrates the process of substitution of  $Ni^{2+}$  by  $Zn^{2+}$ . Earlier this absorption maximum (in magnetite) is related to oscillations of  $Fe^{3+} - O - 2Fe^{3+}$  bond of  $F_{1u}^2$  symmetry type and oscillation frequency change takes place because of distance changes between  $Fe^{3+}$  cations. The analogous situation obviously should be observed for oscillations of  $F_{1u}^3$  and  $F_{1u}^4$  symmetry types influencing on the bonds between the same cations. This fact is seen by the behavior of spectral line 249 cm<sup>-1</sup> ( $NiFe_2O_4$ ), which shifts to the position 206cm<sup>-1</sup> ( $ZnFe_2O_4$ ). The continuous (at the decrease of concentration of Ni ions or at the increase of concentration of Zn ions) changes of absorption band form leading to the appearance of well marked maximum at 206 cm<sup>-1</sup> which corresponds to oscillations of Zn–O bond are observed in 200-300cm<sup>-1</sup> range. The analogous absorption maximum is shown in [10-14].

Table 1

Phonon frequency $Ni_{1-x}Zn_xFe_2O_4$ , cm <sup>-1</sup>							
	x=0	x=0.25	x=0.4	x=0.5	x=0.6	x=0.75	x=1.0
$F_{1u}^1$	604	592	584	578	582	570	-
	-	-	-	544	544	550	542
	533	538	522		535	-	-
	529	528	512	529	525	516	519
	-	524	508	-	518	506	507
	-	456	497	454	-	500	471
	443	442	437	436	-	-	-
	432	433		429	430	-	-
$F_{1u}^2$	425	426	426	424	-	421	426
	-	403	401	-	403	394	398
	392	391	389	389	388	391	388
	-	367	363	356	-	330	332
$F_{1u}^4$	349	345	346	343	324	-	-
	306	306	304	300	299	308	313
	273	275	270	266	284	287	294
$F_{1u}^3$	249	247	-	248	236	-	247
	-	204	204	206	195	206	206
	169	169	171	173	163	177	183
	96	93	95	95	128	81	84
	95	90	89	88	55	77	80
	-	85	84	83	52	73	76
	74	76	71	72	43	58	69



## IR SPECTRA OF (Ni, Zn) FERRITE MICROPOWDERS

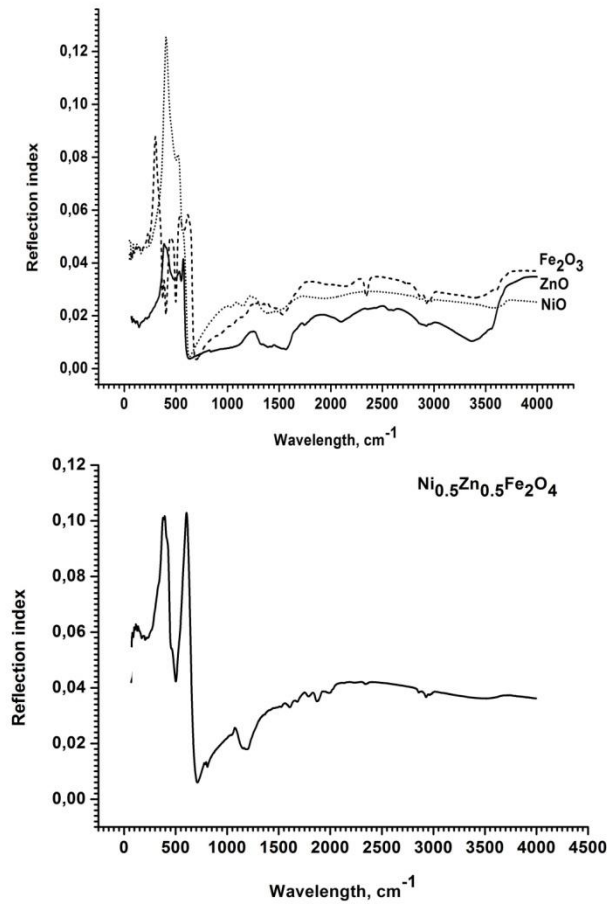


Fig.3. IR spectra of  $\text{Fe}_2\text{O}_3$ ,  $\text{NiO}$  and  $\text{ZnO}$  powders used in synthesis process of  $\text{Ni}_{1-x}\text{Zn}_x\text{Fe}_2\text{O}_4$  ferrites and  $\text{Ni}_{0.5}\text{Zn}_{0.5}\text{Fe}_2\text{O}_4$  composition chosen for example.

The analysis of IR spectra of investigated compositions of  $\text{Ni}_{1-x}\text{Zn}_x\text{Fe}_2\text{O}_4$  ferrites in  $4000\text{cm}^{-1}$  -  $500\text{cm}^{-1}$  range shows that the information about IR spectra of  $\text{ZnO}$ ,  $\text{NiO}$  and  $\text{Fe}_2\text{O}_3$  components is necessary for interpretation of spectral peculiarities (see fig.3). As it was shown earlier  $\text{Ni}_{1-x}\text{Zn}_x\text{Fe}_2\text{O}_4$  ferrites don't solve the excess quantity of  $\text{NiO}$  and  $\text{ZnO}$ . The excess quantity of  $\text{Fe}_2\text{O}_3$  leads to formation of solid solution consisting of magnetite  $\text{Fe}_3\text{O}_4$ . By other hand for achievement of stable state in spinel structures the different forms of disorder appear in the form of point defects and vacancies (for example  $\text{ZnO}$  and  $\text{NiO}$ ), the stability and concentration of which practically don't change until to thermodynamic equilibrium doesn't disturb. The concentration of these defects is enough to reveal them in IR spectra.

The weakly intense absorption band in  $(3627-3500)\text{cm}^{-1}$  range corresponds to the contribution in spectrum from OH ions and oxygen. The spectral band  $(2852-2829)\text{cm}^{-1}$  corresponds to the contribution from  $\text{Ni}^{2+}$  and  $\text{Zn}^{2+}$  ions in spectrum. The exchange process can be divided on stages: 1) composition change from  $\text{NiFe}_2\text{O}_4$  up to  $\text{Ni}_{0.5}\text{Zn}_{0.5}\text{Fe}_2\text{O}_4$  (the line  $2852\text{cm}^{-1}$  shifts to  $2829\text{cm}^{-1}$  decreasing in intensity; 2) composition change from  $\text{Ni}_{0.5}\text{Zn}_{0.5}\text{Fe}_2\text{O}_4$  up to  $\text{ZnFe}_2\text{O}_4$  spectral line shifts to  $2850\text{cm}^{-1}$ , earlier in  $\text{ZnFe}_2\text{O}_4$  this line haven't been registered). Note that this line is the doublet, the second

component of which has very weak intensity. The analogous line  $2904\text{cm}^{-1}$  is observed in  $\text{NiO}$ . The spectral structure observed in  $\text{ZnO}$  ( $1577\text{cm}^{-1}$  and  $1409\text{cm}^{-1}$ ) is revealed in spectral band  $(1550-1400)\text{cm}^{-1}$  in compositions of  $\text{Ni}_{1-x}\text{Zn}_x\text{Fe}_2\text{O}_4$  ferrites gradually appear in exchange process of  $\text{Ni}^{2+}$  by  $\text{Zn}^{2+}$ . Note that the spectral lines  $1586\text{cm}^{-1}$  and  $1585\text{cm}^{-1}$  are always observed in IR spectra of  $\text{Ni}^{2+}$  and  $\text{Fe}^{2+}$  ions correspondingly.

## 4. CONCLUSION

The reflection spectra of  $\text{Ni}_{1-x}\text{Zn}_x\text{Fe}_2\text{O}_4$  ( $x=0, 0.25, 0.4, 0.5, 0.6, 0.75, 1.0$ ) ferrite micro-powders in range from  $4000\text{cm}^{-1}$  up to  $50\text{cm}^{-1}$  are investigated. The phonon frequencies for each ferrite composition and their changes with "x" change are established. It is shown that observable changes in reflection spectra of these ferrites connect with reportioning of  $\text{Ni}^{2+}/\text{Zn}^{2+}$  ion concentration.

## 5. ACKNOWLEDGMENT

The present work is supported by Scientific Development Fund under the President of Republic of Azerbaijan. Grant № EIF02013-9(15)-46/05/1

- 
- [1] Sh.N.Aliyeva, A.I.Nadjafov, T.R. Mehdiyev. *AJP Fizika* **XIX**, 107 (2013). (In Russian).
- [2] Sh.N.Aliyeva, Y.N.Aliyeva, A.I.Nadjafov, I.S.Hasanov, E.K.Huseynov, T.R. Mehdiyev. *Phys. Status Sol.(c)* **12**, 615 (2015).
- [3] F. Shahbaz Tehrani, V. Daadmehr, A. T. Rezakhani, R. Hosseini Akbarnejad, S. Gholipour. *Journal of Superconductivity and Novel Magnetism* **25**, 2443 (2012).
- [4] Jiaqi Wan, Xuehui Jiang, Hui Li, Kezheng Chen *Facile*. *Journal of Material Chemistry* **22**, 13500 (2012).
- [5] M. Kalyan Raju. *Chemical Science Transactions* **4**, 137(2015).
- [6] J.T. Keiser, C.W. Brown, R.H. Heidersbach. *J. Electrochem. Soc.* **129**, 2686 (1982)
- [7] Ming Ma, Yu Zhang, Yu Wei, Hao-ying Shen, Hai-qian Zhang, Ning Gu and Yu.N. Mixaylov, V.A. Kazanchev. *FTT* **52**, 894, (2010). (In Russian).
- [8] S. Jadhav Santosh, E. Shirsath Sagar, B. G. Toksha, S. J. Shukla, K. M. Jadhav. *Chinese Journal of Chemical Physics* **21**, 381 (2008).
- [9] K.P. Belov. *UFN* **166**, 669 (1996). (In Russian).
- [10] J.L.M. Vidales, A.L. Delgado, E. Vila, F.A.Lopez. *J. Alloys Comp.* **287**, 276 (1999).
- [11] Paramita Das, Arghya Dutta, Asim Bhaumik and Chhanda Mukhopadhyay. Heterogeneous ditopic ZnFe<sub>2</sub>O<sub>4</sub> catalyzed synthesis of 4*H*-pyrans: further conversion to 1,4-DHPs and report of functional group interconversion from amide to ester, Electronic Supplementary Material (ESI) for Green Chemistry, This journal is © The Royal Society of Chemistry 2013, 13p
- [12] M. Thomas and K.C. George. Infrared and magnetic study of nanophase zinc ferrite, *Indian J. Pure Appl. Phys.*, 2009, 47, 81
- [13] F.A. Lopez, A.L. Delgado, M.Vidales J.L. and E. Vila. Synthesis of nanocrystalline zinc ferrite powders from sulphuric pickling wastewater, *J.Alloys Comp*,1998,265, 291
- [14] M.A. Ahmed, E.H. El-Khawas, M.Y. Hassan and El-Desoky M. IR Spectroscopy, Magnetic Susceptibility, Mössbauer and ac Resistivity of Co-Zn Ferrite, *Indian J. Phys.*, 2000, 74A, 567.

Receivied: 11.12.2015

## OPTIMIZATION OF SYNTHESIS CONDITION FOR HIGH QUALITY CARBON NANOTUBES

S.H. ABDULLAYEVA<sup>1,2</sup>, N.N. MUSAYEVA<sup>1,2</sup>, C. FRIGERI<sup>3</sup>, A.B. HUSEYNOV<sup>2</sup>  
R.B. JABBAROV<sup>1,2</sup>, R.F. HASANOV<sup>1</sup><sup>1</sup>*G.M. Abdullayev Institute of Physics of NASA, Azerbaijan**AZ-1143, Baku, H. Javid ave., 131*<sup>2</sup>*Research & Development Center for Hi-Technologies, MCHT, Baku, Azerbaijan*<sup>3</sup>*IMEM, CNR, Parma, Italy*

High quality Multi Wall Carbon nanotubes (MWCNTs) have been synthesized in Aerosol –CVD reactor by the optimization of the synthesis process.

Scanning and Transmission electron microscopes have been used for characterization of CNTs, grown under different synthesis conditions (different values of reaction temperature and ferrocene/cyclohexane relation).

It was established that the reaction temperature between 840-950°C and 15-18 mg/ml ferrocene/cyclohexane relation are optimal conditions for the synthesis of long (up to 650 µm) MWCNTs, which diameters range between 10 and 85 nm.

**Keywords:** CNTs, Aerosol-CVD, SEM, TEM, ferrocene.

**PACS:** 61.48.De, 81.15.Gh, 81.20.Ka, 68.37.Hk, 68.37.Og

## 1. INTRODUCTION

The outstanding properties of carbon nanotubes (CNTs) as a functional material for electronic devices, computation, power generation, catalysis, medicine and drug delivery causes a great interest to understand what factors control the nanotube sizes, number of walls, the helicity and the defectiveness of the tubular structure during synthesis process; this is due to the fact that different structure of the tubes may result in great changes in their mechanical and electrical properties [1-4]. In general, CNTs are synthesized by arc discharge, laser ablation, chemical vapor deposition (CVD) and spray pyrolysis [5-8]. Although first two methods from above mentioned can produce high quality SWNTs, the available quantity from both arc discharge and laser ablation is limited. The other problem is to develop cost effective, eco- friendly method synthesis of high quality CNTs with good parameters and large scale.

In this paper we report about the characterization of CNTs, synthesized by Aerosol assisted Chemical Vapor Deposition (A-CVD) method, using various temperatures and catalyst concentration. Have been analyzed the influence of different technological conditions to structural and physical properties of the synthesized CNTs.

## 2. EXPERIMENT

To synthesize CNTs have been used horizontal quartz reactor (2 m length quartz tube) covered by movable electric furnace with 35 cm long and 22 cm in diameter. This technology is based on the injection of the solution in the reactor as an aerosol and its decomposition under high temperature (830-1000°C). Cyclohexane (C<sub>6</sub>H<sub>12</sub>) and ferrocene (Fe(C<sub>5</sub>H<sub>5</sub>)<sub>2</sub>) were used as chemical raw material and catalyst, respectively. The solution with different ferrocene/cyclohexane relation was transformed into an aerosol by the ultrasonic transducer (frequency - 800 kHz). The aerosol was injected to the quartz reactor,

which equipped with high temperature movable furnace by using transport gas (Ar/H<sub>2</sub> mixture). Each sample of the CNTs with different synthesis condition has been analyzed. Scanning electron microscopy (SEM) and transmission electron microscopy (TEM) have been used to observe morphology, and characterize geometric parameters (diameter, length, number of shells) of the obtained CNTs and Fe position in the CNT.

## 3. RESULTS AND DISCUSSION

To find optimal technological condition was changed some of parameters of the reaction: decomposition temperature, Fe content in the solution, gas flows, et.al. The temperature dependence was determined in the range of 830-1000°C. Lower synthesis temperatures result to low carbon nanotube yield and SEM observations show that the increasing temperature led to formation of other carbon structure or pyrolytic carbon, which relative weight to CNTs is increasing in high temperatures (higher than 950°C). At 1000°C on quartz tube was deposited other carbon structures or pyrolytic carbon. Fig. 1 shows SEM pictures of carbon structures, grown at 840 and 1000°C for comparison. It is observed that, increasing of reaction temperature near limit led to formation of more straight, smooth and longer CNTs, compared with low synthesis temperature (at 830°C ~90 µm, 950°C ~630 µm (see fig. 2).

Most of the CVD techniques require presence of metallic catalyst during the growth of CNTs, because it may affect not only successful growth, and also morphology, number of walls of the grown nanotubes. Several metals used as catalyst, but shown that among of them Fe is more suitable for crystallization of the nanotubes and same time it is interesting for application point of view [9-11].

Has been varied the different volume of Fe catalyst in cyclohexane solvent in order to understand how influence the catalyst quantity to the end product. If ferrocene is absent in the cyclohexane solvent is not

observed any deposition on quartz surface (was not grown CNTs). The volume of deposited product is increased by increasing ferrocene quantity in the solution. This process

is limited, because more than 20 mg/ml in ferrocene/cyclohexane relation lead to saturation of solvent.

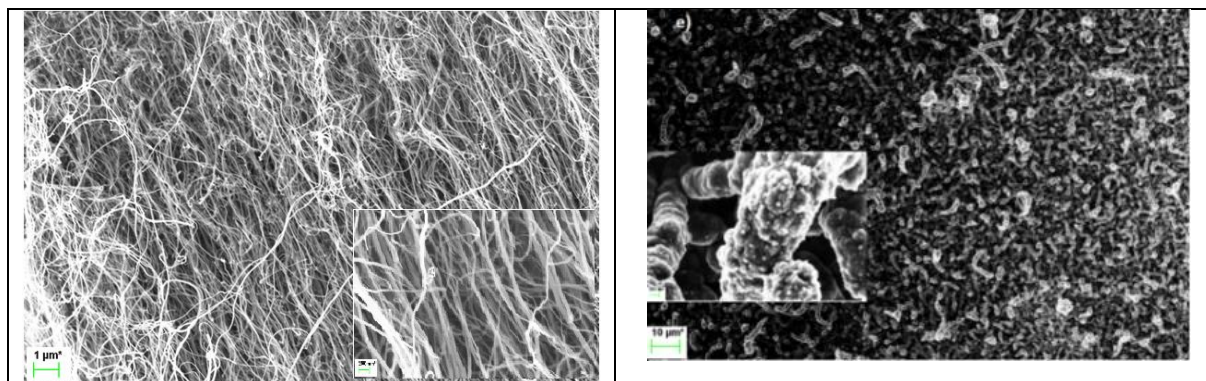


Fig.1. SEM pictures of CNTs grown by Aerosol CVD method: left – growth temperature -840°C; right- growth temperature -1000°C

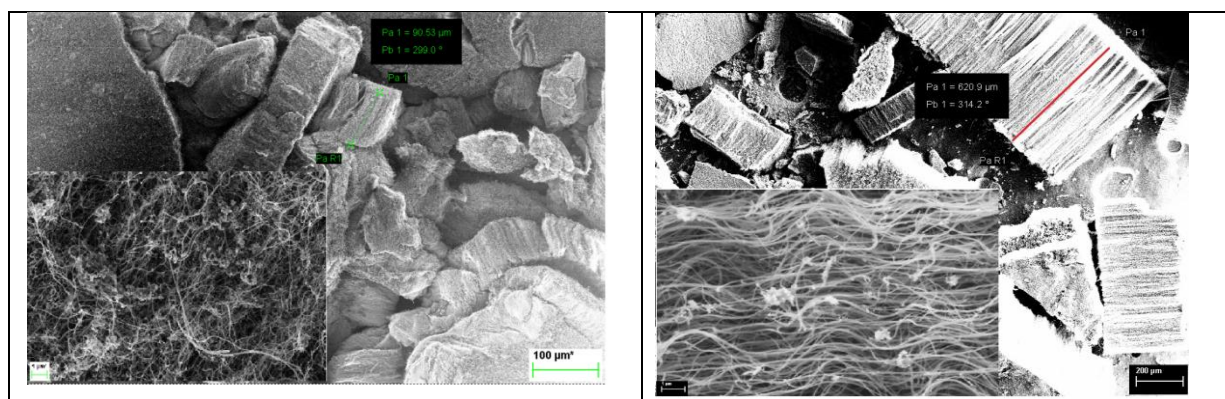


Fig.2. CNTs, grown at 830°C (left) and 950°C (right)

It was observed that relative concentration of other carbon structures or pyrolytic carbon to CNTs is increasing with increasing Fe concentration in the solution. It can be assumed that due to increasing the numbers of the catalyst centers, which were involved in growth of carbon nanotubes, after decomposition by temperature the carbon atoms were seeking after new catalytic centers instead of continuing the growth of

CNTs, which has already begun. This process is chaotic. TEM observations of CNTs have provided with more detailed information about diameter, number of walls, structure and position of the catalyst in the CNTs. The number of the walls increases with increasing CNT diameter. The C layers are nicely visible for all CNTs (fig. 3).

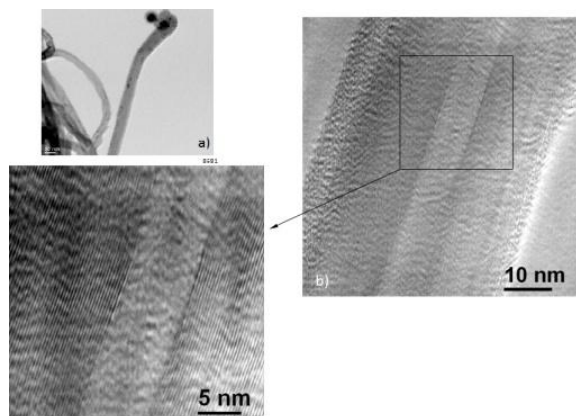


Fig.3. a) CTEM image of a CNT with diameter  $D \approx 45$  nm. b) HR-TEM image taken along the CNT. c) High magnification of the squared area of b).



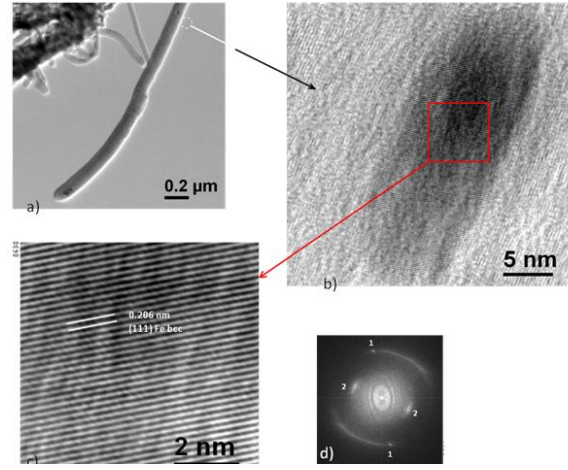


Fig.4. HR-TEM results of CNTs. b) is the HR-TEM image of the dash-circled area of a) with its magnification in c).

A HR-TEM study of a Fe-rich area of the CNTs is presented in fig. 4. The fringes of the lattice planes have a spacing of 0.206 nm which pretty agrees with the spacing of the (111) planes of Fe bcc. The FFT (fast Fourier transform), i.e. electron diffraction pattern, from the Fe-rich area and surrounding matrix (fig. 4d) confirms that conclusion. In fig.4d the spots 1 are due to the (111) planes of Fe bcc, whilst spots 2 give  $d_{hkl} = 0.340$  nm that pretty agrees with the spacing of the (002) planes of graphite ( $d_{002} = 0.3395$  nm, according to the WebEMAPS)

For the smaller thicknesses, only some discontinuous segments of C layers are visible (fig. 5

right). This anyway may be sufficient to confirm that also the small NTs have a MW (6-8 layers) structure although quite irregular and discontinuous.

The inner channel also increases from  $\sim 2.2$  to  $\sim 15$  nm for D increasing from 11 to 60 nm but then drops to  $\sim 6$  nm for D=85 nm (fig. 6).

TEM results show that MWCNTs, which is observed, are partially filled by pure Fe and it was also found at different positions along the CNT, not only at the CNT tip (fig.7). This has been concluded by applying several operation modes of the TEM: X-EDS, EF-TEM, HAADF, HR-TEM.

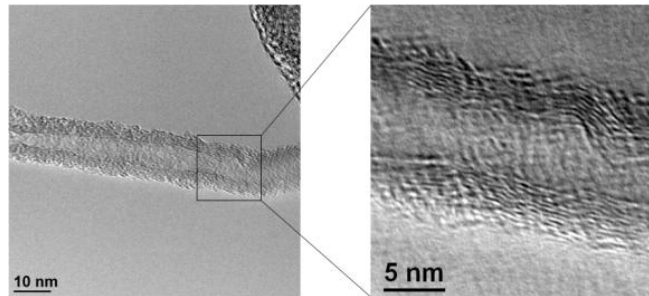


Fig.5. Left: HR-TEM image of a CNT with diameter D~13 nm. Right: high magnification of the squared area.

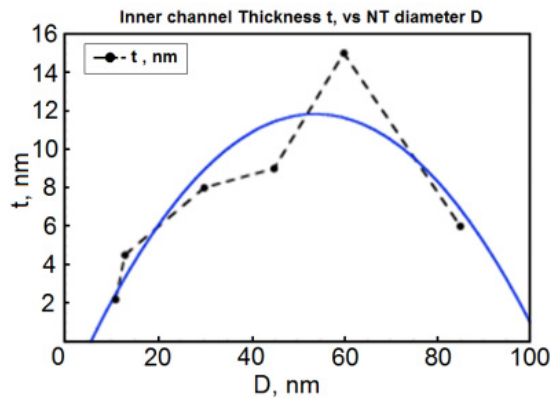


Fig.6. Thickness (t) of the inner channel as a function of the NT diameter (D). The black dots are the experimental data while the blue parabolic curve is a tentative fitting.

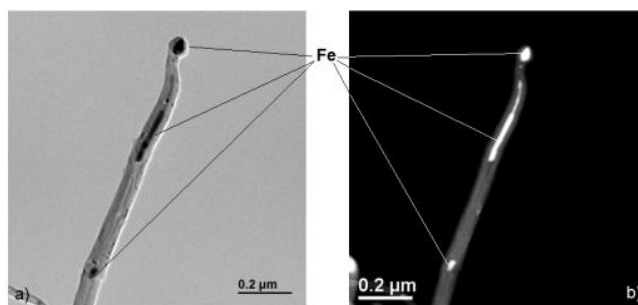


Fig.7. a) CTEM image of CNT; b) Corresponding HAADF image.

#### 4. CONCLUSION

It was grown long (up to 650  $\mu\text{m}$ ) multiwall carbon nanotubes, which diameters between 10 and 85 nm by optimization of synthesis process in the Aerosol-CVD system.

It was established that the reaction temperature between 840-950 $^{\circ}\text{C}$  and 15-18 mg/ml ferrocene/cyclohexane relation are optimal condition for synthesizing of high quality CNTs.

TEM observations of grown CNTs have provided with more detailed information about diameter, number of walls, structure and position of the catalyst in the CNTs. The number of the walls increases with increasing CNT diameter up to 85 nm. The distance between the CNT walls is calculated 0.340 nm, corresponding to graphite

(002). For the smaller thicknesses ( $\sim 10\text{-}15$  nm) only some discontinuous segments of CNT walls are visible. This anyway may be sufficient to confirm that also the small CNTs have a MW (6-8 layers) structure although quite irregular and discontinuous.

Has been defined that Fe nanoparticles were situated not only in the tip of the tubes, and also along the length of the nanotube (in the inner channel of the CNTs) and no other impurities or composites are present in the tubes or around of them.

#### ACKNOWLEDGEMENTS

This work was financial supported by the Scientific Found of the SOCAR - Oil Company of Azerbaijan Republic.

- 
- [1] *P.J. Harris*, Cambridge University Press, Cambridge, (1999).
  - [2] *M.S. Dresselhaus, G. Dresselhaus and R. Saito*, Physical Review., B45: 6234 (1992).
  - [3] *J.W. Mintmire, B.I. Dunlap and C.T. White*, Physical Review Letters 68, 631–634 (1992).
  - [4] *N.Hamada, S.Sawada and A.Oshiyama*, Physical Review Letters 68, 1579-1581 (1992).
  - [5] *S. Iijima and T. Ichihashi*, Nature 363, 603–605 (1993).
  - [6] *T.W. Ebbesen and P. M.Ajayan*, Nature 358, 220–222 (1992).
  - [7] *J.C. Charlier and S. Iijima*, Topics in Applied Physics 80, 55-80 (2001).
  - [8] *J.A. Gómez, A. Marquez, A. Pérez and A. Duarte-Moller*, Advances in Materials Science and Engineering, v. 7 (2012).
  - [9] *J.W. Seo, K. Hernadi, C. Miko and L. Forro*, Applied Catalysis A: General 260, 87-91 (2004).
  - [10] *C.J. Lee, S.C. Lyu, H.W. Kim, J.W. Park, H.M. Jung and J. Park*, Chemical Physics Letters 361, 469–472 (2002).
  - [11] *H. Yokomichi, F. Sakai, M. Ichihara and N. Kishimoto*, Physica B 323, 311-313 (2002).

Received: 10.12.2015

# VACANCY FORMATION ENERGY FOR CHARGED AND NEUTRAL STATES IN $\text{TlInS}_2$

G.S. ORUDZHEV<sup>1,2</sup>, N.A. ISMAYILOVA<sup>2</sup>

<sup>1</sup>Azerbaijan Technical University, H. Javid ave, 25, Baku, Az-1073, Azerbaijan

<sup>2</sup>Institute of Physics (Innovation Sector), H. Javid ave, 131, Baku, Az-1143, Azerbaijan  
ismayilova\_narmin\_84@mail.ru

For  $\text{TlInS}_2$  64-atom supercell, in LDA approximation of Density Functional Theory taking into account Hubbard+U corrections, from Fermi energy dependence of the Tl, In, S neutral and charged vacancy formation energies the transition levels were defined: for S-rich condition of S vacancies  $q=0$  charge state transfers to  $q=-2$  charge state, in 1.5 eV; for rich condition of Tl and In vacancies  $q=-1$  charge state transfers to  $q=-2$  charge state, in 0.5 eV and 1.75eV, respectively.

Considering that the calculated value of the energy gap obtained with LDA and LDA+U schemes (respectively 1.25 eV and 1.47 eV) are lower than experimental one (2.2 eV) and accepting the correction to agree on experimental value it was found that in arbitrary positions of the Fermi level within the band gap no transitions occur from the one charge state to another and as a result S vacancy remains in a neutral  $q=0$  state, and Tl and In vacancies in a  $q=-1$  charge state.

**Keywords:** pseudopotential, charged and neutral vacancy, defect, formation energy, valence band maximum.

**PACS:** 61.72.jd

## INTRODUCTION

The III-III-VI<sub>2</sub> family of crystals exhibit quasi low-dimensionality in the form of layered and chain structures and has become increasingly attractive due to their interesting structural properties and potential optoelectronic applications [1]. Like all layered  $\text{TlMeX}_2$  (where Me=In or Ga and X=S or Se)  $\text{TlInS}_2$  has C2/c space group symmetry at room temperature [2]. The fundamental structural unit of a layer is the  $\text{In}_4\text{S}_6$  ( $\text{Ga}_4\text{S}_6$ ) adamantane-like units linked together by bridging S atoms. The Tl atoms are in trigonal prismatic voids resulting from the combination of the  $\text{In}_4\text{S}_6$  ( $\text{Ga}_4\text{S}_6$ ) polyhedra into a layer [3]. The cell structure of  $\text{TlInS}_2$  shown in fig.1. In the crystal structure of  $\text{TlInS}_2$ , the Van der Waals interaction favors the formation of numerous, both point and extended, defects embedded predominantly in the interlayer space of the crystal. The effect of impurities on the phase transitions in the ferroelectric semiconductors  $\text{TlInS}_2$  have been studied [4].

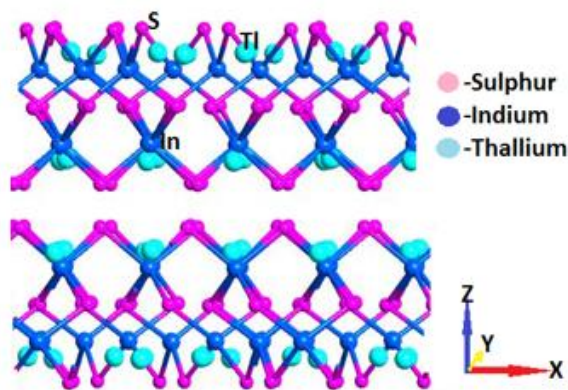


Fig.1. Cell structure of  $\text{TlInS}_2$ .

In this work, we aimed to examine the dependence of the defect formation energies (DFE) on the chemical potentials and Fermi-level position for the various charge states of Tl, In, S vacancy of the  $\text{TlInS}_2$  segnetoelectric semiconductor supercell containing 64 atoms and to determine corresponds transition levels on this basis. Our calculations were performed for neutral and charged vacancy defect, by Local Density Approximation (LDA) [5] and implementing the LDA+U method using the Atomistix ToolKit software program (ATK, <http://quantumwise.com/>) [6]. The electron-ion interactions were taken into account through pseudopotentials of the Fritz Haber Institute (FHI). The number of the electrons treated as valence electrons was 3 for Tl ( $6s^2 6p^1$ ), 3 for In ( $5s^2 5p^1$ ) and 6 for S ( $3s^2 3p^4$ ). The Perdew-Burke-Ernzerhof (PBE) exchange-correlation functional and Double Zeta Polarized basis sets were used in our calculations. The kinetic cut-off energy was 150 Ry. To determine the coordinates of the atoms and the lattice parameters of  $\text{TlInS}_2$  primitive cell structure was relaxed and optimized with force and stress tolerances of 0.0001 eV/Å and 0.0001 eV/Å<sup>3</sup>, respectively. The supercells containing vacancies were relaxed with force tolerance of 0.05 eV/Å.

The calculated band structures with LDA using HGH pseudopotential in Quantum Wise Atomistix ToolKit program and SGGA [7] using ultrasoft pseudopotential in Quantum Espresso [8] software programs show that bulk  $\text{TlInS}_2$  is a direct band gap semiconductor with the valence band top and the conduction band bottom located at the center of the Brillouin zone and  $E_g=1.25$  eV [9]. By LDA+U (the Hubbard parameter U we use for S 3p state  $U=3$ eV) scheme we defined that  $E_g=1.47$  eV. The calculated values of the energy gap are lower than experimental one (2.35 eV) [10].

## RESULTS AND DISCUSSION

The formation energy of a point defect is not a constant but depends on the growth or annealing conditions [11]. In the case of charged vacancy, the

formation energy further depends on the Fermi level ( $E_F$ ), which is the energy of the electron reservoir, i.e. the electron chemical potential. We calculated formation energy by:

$$E^f(V_a^q) = E_{tot}(V_a^q) - E_{tot}(TlInS_2) + \mu_a + q(E_F + E_{VBM}) \quad (1)$$

where  $E_{tot}(V_a^q)$  is the total energy of a supercell containing the vacancy of atom ( $a=Tl, In, S$ ) in the charge state  $q$ ,  $E_{tot}(TlInS_2)$  is the total energy of  $TlInS_2$  perfect crystal in the same supercell and  $\mu_a$  is the  $a$ -atoms chemical potential. First we determine the chemical potentials of atoms as  $E_{tot}$  energy per one atom. For this purpose we used cell and structure parameters of  $Tl, In$  and  $S$  taken from the literature [6] and optimized them. Another important physical parameter for the calculation

of the defect formation energy is the position of the valence band maximum (VBM), which corresponds to the reference energy level for the electron chemical potential. VBM is determined by adding the perfect supercell VBM with the Fermi level [13].

DFE of charged vacancies calculated in the case of rich atom conditions. Rich conditions of atoms forming the vacancy given by the thermodynamic stability condition:

$$E_{tot}(TlInS_2) - [E_{tot}(Tl) + E_{tot}(In) + 2E_{tot}(S)] = H_f(TlInS_2), \quad (2)$$

where  $H_f(TlInS_2)$  is the enthalpy of formation of bulk  $TlInS_2$  negative for a stable compound. The calculated enthalpy of formation of  $TlInS_2$  is  $H_f(TlInS_2) = -2.983$  eV. Adding the value of enthalpy to chemical potential of atom forming the vacancy we gain the rich condition of this atom respectively [14]. So rich conditions for each of the three atoms can be calculated as follows:

$$\mu_{Tl,In,S}^{min} = E_{tot}(Tl, In, S) + H_f(TlInS_2) \quad (3)$$

In our calculation transition level  $\varepsilon(q/q')$  is defined as the Fermi-level position for which the formation energies of charge states  $q$  and  $q'$  are equal.  $\varepsilon(q/q')$  can be obtained from

$$\varepsilon(q/q') = [E^f(V_q; E_F = 0) - E^f(V_{q'}; E_F = 0)] / (q' - q), \quad (4)$$

where  $E^f(V_q; E_F = 0)$  is the formation energy of the defect  $V$  in the charge state  $q$  when the Fermi level is at the valence band maximum ( $E_F = 0$ ).

The experimental significance of this transition level is that for Fermi-level positions below  $\varepsilon(q/q')$ , charge state  $q$  is stable, while for Fermi-level positions above  $\varepsilon(q/q')$ , charge state  $q'$  is stable [12]. In fig. 2 (In-rich limit LDA) the slope of the line changes from -1 to -2 at the intersection of lines with  $q=-1$  and  $q=-2$ . For In-rich condition the energy of intersection will be denoted by  $\varepsilon(-1/-2)$ . The  $q=-1$  state is more stable when  $E_F < \varepsilon(-1/-2)$ , and the  $q=-2$  is favorable when  $E_F > \varepsilon(-1/-2)$ . The calculated transition energy level for In is:  $E=1.25$  eV. In fig.2 (S-rich limit LDA) energy of intersection will be denoted by  $\varepsilon(0/-2)$  for S rich condition, where  $E_F < \varepsilon(0/-2)$ , corresponds to more stable  $q=0$  state and the  $q=-2$  is favorable when  $E_F > \varepsilon(0/-2)$ . Transition energy level for S is:  $E=1.5$  eV.

Tl-rich limit LDA (fig.2) describe the line changes from -1 to -2 at the intersection of lines with  $q=-1$  and  $q=-2$  for Tl vacancy. In this case the  $q=-1$  state is more stable when  $E_F < \varepsilon(-1/-2)$ , and the  $q=-2$  is favorable when  $E_F > \varepsilon(-1/-2)$ . Transition energy level for Tl is  $E=1.5$  eV.

The band gap obtained from LDA and the LDA +  $U$  schemes have been small compared with experimental results. Although the LDA+ $U$  approach only corrects part of the band-gap error, it provides us with a basis for obtaining a full band-gap correction through a physically justified extrapolation scheme [12]. Our approach takes advantage of the fact that the extent to which transition levels  $\varepsilon(q/q')$  change in going from LDA to LDA+ $U$  reflects their relative valence-band and conduction band character. The procedure is to perform calculations using the LDA, on the one hand, and the LDA+ $U$ , on the other hand, and then extrapolate to the experimental gap:

$$\varepsilon(q/q') = (\varepsilon(q/q')^{LDA+U} - \varepsilon(q/q')^{LDA}) / (E_g^{LDA+U} - E_g^{LDA}) * (E_g^{exp} - E_g^{LDA+U}) + \varepsilon(q/q')^{LDA+U} \quad (4)$$

Here,  $E_g^{LDA}$  and  $E_g^{LDA+U}$  are the band gaps given by the LDA and LDA+ $U$  approximations and  $E_g^{exp}$  is the experimental gap. As a result,  $Tl(-1/-2)=2.26$  eV,  $In(-1/-2)=0.74$  eV,  $S(0/-2)=2.26$  eV from obtaining value it was obvious that in arbitrary positions of the Fermi level

within the band gap no transitions occur from the one charge state to another. Thus S vacancy remains in a neutral  $q=0$  state, and Tl and In vacancies in a  $q=-1$  charge state.



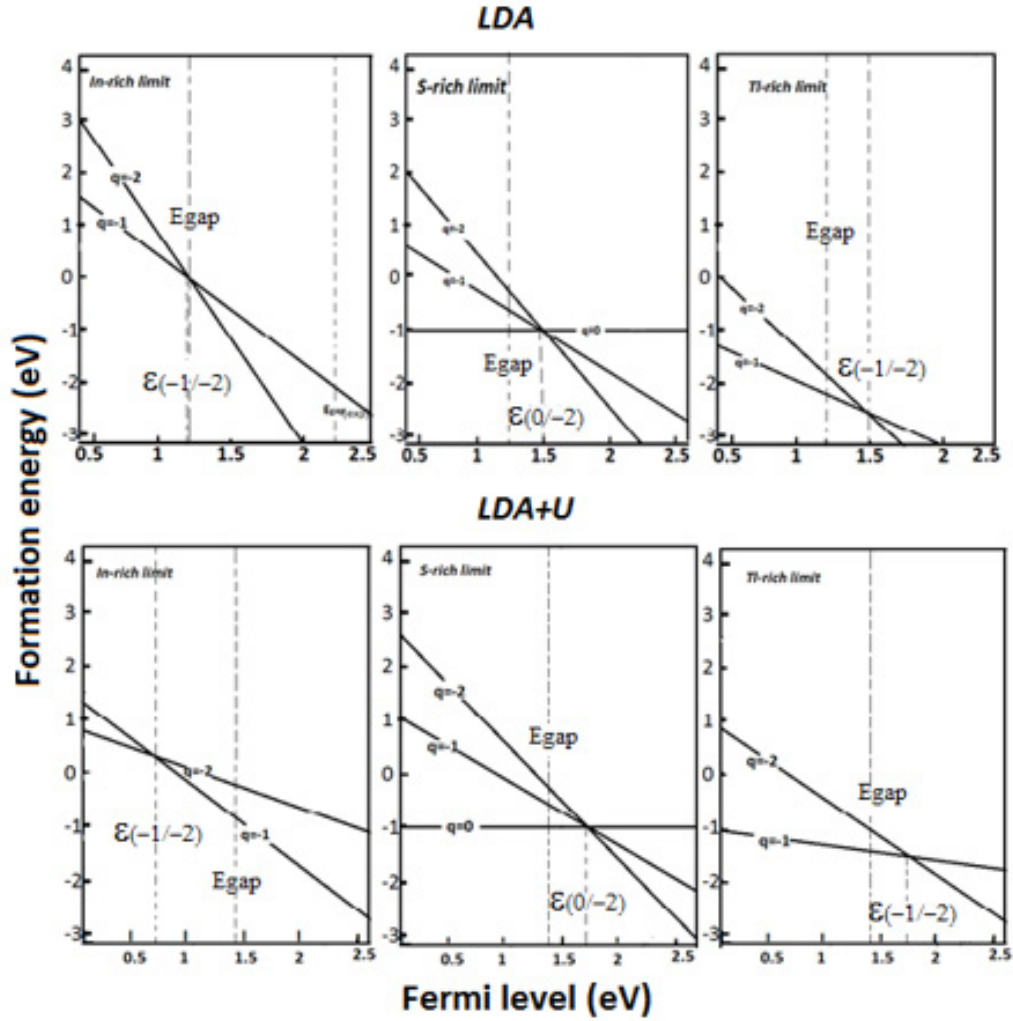


Fig. 2. Formation energies as a function of Fermi-level position for neutral and charged vacancy in TlInS<sub>2</sub>. Results for In-rich, S-rich and Tl-rich conditions with LDA and LDA+U are shown.

## CONCLUSION

Dependence of formation energy on charged and neutral states as a function of the Fermi level for TlInS<sub>2</sub> crystal calculated using the LDA and the LDA + U schemes. Considering that the calculated value of the

band gap (1.25 eV with LDA, LDA + U 1.47 eV) are lower than the experimental (2.2 eV), and extrapolating the calculated dependence to experimental value, it was found that in any position of the Fermi level within the band gap S vacancy remains in the neutral charge state  $q = 0$ , and Tl, In vacancies in the  $q = -1$  charge state.

- [1] K.A. Yee, A. Albright, *J.Am.Chem. Soc.* 113, 6474 (1991).
- [2] W. Henkel, H.D. Hochheimer, C. Carlone, A. Werner, S. Ves, and H.G. von Shnering. *Phys. Rev.*, B.26. 3211. (1982).
- [3] N.M. Gasanly and N.S. Yuksek. Low-Temperature Raman Scattering in TlGa<sub>x</sub>In<sub>1-x</sub>S<sub>2</sub> Layered Mixed Crystals: Compositional Dependence of the Mode Frequencies and Line Shapes Vol. 108 Acta Physica Polonica A No. 6(2005).
- [4] S.S Babaev, E.Basaran, T.G.Mammadov, F.A. Mikailov, F.M. Salehli, MirHasan Yu. Seyidov and R.A. Suleymanov. The effect of impurities on the phase transitions in the ferroelectric semiconductors TlInS<sub>2</sub> and TlGaSe<sub>2</sub> *Journal of Physics* Vol.27 (2015).
- [5] W. Kohn. and L. Sham. Self-consistent equations including exchange and correlation Effects, *Phys. Rev.*, 140 A1133 – A1138. (1965).
- [6] <http://quantumwise.com/>
- [7] J.Perdew, K.Burk, Y.Wang. Generalized gradient approximation for the exchange correlation hole of a many-electron system, *Phys. Rev. B* 54 16533-16539. (1996).
- [8] <http://quantum-espresso.org>
- [9] N.A. Ismayilova, G.S. Orudzhev. Electron spectrum and DOS calculations for TlInS<sub>2</sub> crystal from first principles. *ANAS Transaction* №5, Vol.35 p.15-19. (2015).
- [10] M.M. El-Nahass and M.M. Sallam Optical and Photoelectric Properties of TlInS<sub>2</sub> Layered Single Crystals. *Egypt. J. Solids*, Vol. (31), No. (1), (2008).

- [11] *C.G. Van de Walle and J. Neugebauer*. J. Appl. Phys. 95, 3851. (2004).
- [12] *Anderson Janotti and Chris G. Van de Walle*. Native point defects in ZnO. Phys. Rev., B 76, 165202 (2007)
- [13] *M.A. Mehrabova, H.R. Nuriyev, H.S. Orujov*. Defect formation energy for charge states and electrophysical properties of CdMnTe. Photonics, Devices, and Systems VI, edited by Pavel Tománek, Dagmar Senderáková, Petr Páta, Proc. of SPIE Vol. 9450, 94500Q (2015).
- [14] *Anderson Janotti and Chris G Van de Walle*. Fundamentals of zinc oxide as a semiconductor. Rep. Prog. Phys. 72 126501 (29pp) (2009).

*Received: 15.01.2016*

# INVESTIGATION OF PHASE TRANSITION IN $\text{Cu}_4\text{Te}_{1.5}\text{Se}_{0.5}$ SOLID SOLUTION BY HIGH-TEMPERATURE ROENTGENOGRAPHY METHOD

N.A. ALIYEVA, G.G. GUSEYNOV, G.M. AGAMIRZOYEVA, T.R. MEHDIYEV

*G.M. Abdullayev Institute of Physics of NASA, Azerbaijan*

*AZ-1143, Baku, H. Javid ave., 131*

The solid solution of  $\text{Cu}_4\text{Te}_{1.5}\text{Se}_{0.5}$  is synthesized. By roentgenographic method it is established that  $\text{Cu}_4\text{Te}_{1.5}\text{Se}_{0.5}$  samples crystallize in trigonal structure with lattice periods in hexagonal establishment:  $a_h=8,2319(11)$  Å,  $c_h=21,4145(23)$  Å,  $V=1089,811(12)$  Å<sup>3</sup>, sp.gr. P3m1,  $Z=22$ ,  $\rho_x=7,33$  gr/cm<sup>3</sup>. By comparative roentgen-phase analysis of temperature diffraction data it is established that trigonal phase of  $\text{Cu}_4\text{Te}_{1.5}\text{Se}_{0.5}$  at room temperature transits at  $T=750\pm 3$ K into two-phase system consisting of hexagonal phase of  $\text{Cu}_2\text{Te}_{0.5}\text{Se}_{0.5}$  composition with periods  $a=4,231$  Å,  $c=7,223$ Å; sp.gr. P6<sub>3</sub>/mmc and cubic phase of  $\text{Cu}_2\text{Te}$  composition with  $a = 6,049$  Å periods. It is shown that near  $T=800\text{K}\pm 5\text{K}$  the two-phase system transits into unique cubic phase with periods  $a=6.061$  Å.

**Keywords:** crystals, structure, phase, phase transitions, lattice parameters.

**PACS:** 77.22.Ch, 77.80.Bh, 77.80.Dj, 78.20.Fm

## INTRODUCTION

It is known that the development of electron technique, energetic and radio electronics stimulates the search and investigation of physicochemical properties of perspective materials. In this relation the thermomagnetic and thermoelectric materials with small lattice thermal conductivity and high mobility of charge carriers has the wide region of application in the capacity of thermoelectric transformers [1-3]. Ag, Cu chalcogenides and based on them different solid solutions are to them. It is obvious that for effective use of these materials it is necessary to have experimental data on influence of external factors on structure and structural changes. Note that for above mentioned chalcogenides the presence of polymorphous transformations under temperature influence is the one of character properties [4-6]. The results of experimental investigations of synthesis and structural-phase transitions of  $\text{Cu}_4\text{Te}_{1.5}\text{Se}_{0.5}$  in temperature interval 360-1250K are given in present work. Note that all roentgen-diffraction experiments are carried out on powder diffractometer "D8 ADVANCE Bruker (Germany) in regime: 40kV, 40mA,  $05^\circ \leq 2\theta \leq 80^\circ$ ,  $\text{CuK}_\alpha$  - radiation,  $\lambda=1.5406$ Å. The temperature investigations are carried out in HTK16 camera in vacuum 1.3 torr. The heating rate is  $2^\circ/\text{min}$ .

## EXPERIMENTAL PART

**Synthesis.** The samples of  $\text{Cu}_4\text{Te}_{1.5}\text{Se}_{0.5}$  solid solution are synthesized by the melting of initial elements Cu, Te, Se having the purity not less 99.998 in vacuum-processed quartz ampoule  $10^{-2}$  Pa in one-zone furnace. The ampoule of length 20 cm with substance (5gr) is gradually put into furnace with temperature 1200K. After that the furnace is closed and ampoule is kept at this temperature during one hour. Further, the temperature into furnace is slowly decreased up to 750K and ampoule with substance is kept during 5 days for homogenization.

**The investigation of phase transformations.** For establishment of possible structural transformations in

$\text{Cu}_4\text{Te}_{1.5}\text{Se}_{0.5}$  sample one can determine the crystallographic parameters of low-temperature phase.

Table 1.

Roentgen-diffraction data for  $\text{Cu}_4\text{Te}_{1.50}\text{Se}_{0.50}$  at 300K

№	$2\theta$	$d_{\text{exp}}$	$I/I_0$	$hkl$
1	12.398	7.13387	22.2	100
2	21.558	4.11874	3.2	110
3	24.943	3.56694	100	200, 006
4	26.372	3.37680	3	202
5	28.272	3.15405	14.1	203
6	29.237	3.05213	7.6	007
7	33.199	2.69635	13.7	008
8	35.831	2.50414	12.4	206
9	36.616	2.45222	8.5	213
10	40.172	2.24298	4.7	207
11	42.054	2.14684	20	00.10
12	42.887	2.10704	33	208
13	43.931	2.05937	81.7	222
14	45.824	1.97858	77.6	223
15	47.735	1.90375	3.5	224
16	51.178	1.78347	32.9	00.12
17	51.968	1.75820	2.3	226
18	52.943	1.72808	1.2	402
19	53.067	1.72435	3.6	403
20	53.645	1.70712	1.1	404
21	55.917	1.64301	2.7	00.13
22	58.478	1.57703	4.7	406
23	60.631	1.52607		00.14
24	63.072	1.47276	5.5	408
25	65.135	1.43100	4.9	00.15
26	65.352	1.42677	10.61	500
27	66.031	1.41374	1	409
28	66.875	1.39793	4.4	503
29	66.982	1.39596	2.6	501
30	68.047	1.37668	8.3	420
31	68.26	1.37291	1.6	421
32	69.691	1.34817	5.8	423
33	70.96	1.32714	3.7	00.16

To this purpose the small powder from synthesized sample is prepared and made the diffractograms in vacuum. On the base of the calculative analysis of obtained diffracted data with the help of "TOPAS" program is determined that synthesized sample crystallizes in hexagonal lattice with parameters  $a_h=8.2319\text{\AA}$ ,  $c_h=21.4145$ ,  $V=1089,811\text{\AA}$ , sp.gr P31c,  $Z=4$ ,  $\rho_x=8.11\text{gr/cm}^3$  at 300K. The diffractogram of  $\text{Cu}_4\text{Te}_{1.5}\text{Se}_{0.5}$  phase at room temperature is shown in fig.1a, and calculated crystallographic data  $2\theta$ ,  $I$ ,  $d$ , reflexion indexes ( $hkl$ ) are given in table 1. The high-temperature investigations are carried out after obtaining of above mentioned main crystallographic parameters of phase  $\text{Cu}_4\text{Te}_{1.5}\text{Se}_{0.5}$  at room temperature. To this purpose the necessary diffractometric photos for different temperatures with step 50K are obtained. The sample is

kept in each temperature point of photoradiography at the given temperature during 25 minutes for temperature stabilization in whole camera volume with investigated sample. Further, the comparative analysis of obtained temperature diffractograms is carried out.

The carried comparative analysis shows that in temperature interval  $300 < T < 1250\text{K}$  the essential diffraction changes corresponding to possible structural transitions take place near temperatures  $T=770\text{K}$  and  $T=850\text{K}$ . In other words, the trigonal  $\alpha$ -phase up to temperature 750K keeps own structure.

Note that the treatment of obtained diffraction experiments shows that the structural change process begins as a result of gradually temperature increase in trigonal structure of  $\alpha$ -phase of  $\text{Cu}_4\text{Te}_{1.5}\text{Se}_{0.5}$  at  $T \approx 723\text{K}$ .

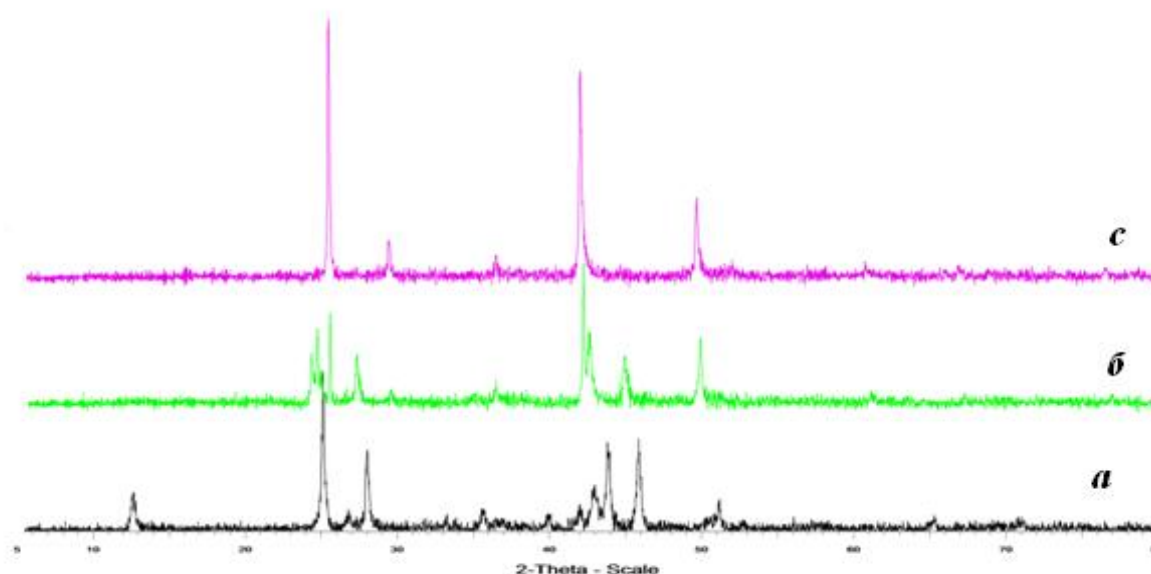


Fig.1.  $\text{Cu}_4\text{Te}_{1.5}\text{Se}_{0.5}$  diffractograms at different temperatures: 1-300K, 2-770K, 3-900K.

The diffractogram "b" fig.1 shows that the process of structural transformation near  $T=770\text{K}$  is seemed to be finished as at given temperature almost all reflections of  $\alpha$ -phase disappear, but the new system of reflections appears, on the base of which one can propose that the structural phase transformations takes place.

That's why for definition of equilibrium temperature of the given transition we begin to observe the change of the positions of diffraction reflections by decrease of heating step. To this purpose we observe for reflection position changes beginning from  $T=725\text{K}$  in each 10K. It is observed that at  $T=755\text{K}$  almost all diffraction peaks of  $\alpha$ -phase disappear and we obtain the observable diffractograms at  $T=770\text{K}$  as a result of observation for process of reflection position changes. The process temperature decrease from 755K up to 745K with step 5K shows that the system returns to previous structure, i.e. to  $\alpha$ -phase at  $T=745\text{K}$ . Thus, it is established that transition temperature of low-temperature  $\alpha$ -phase in new phase is  $750 \pm 3\text{K}$ .

In the next investigation stage one should define the crystallographic parameters and lattice symmetry obtained by phase transformation of room temperature trigonal  $\alpha$ -phase  $\text{Cu}_4\text{Te}_{1.5}\text{Se}_{0.5}$ .

Note that multiple attempts of lattice constant obtaining of investigated substance from diffractogram found at temperature 750K using the structural program TOPAS doesn't give us the expected results. That's why we suppose that observable diffraction change at  $T=770\text{K}$  isn't the phase transformation but sample decomposition under temperature influence. The fact of diffraction change higher than  $T=800\text{K}$  contradicts to above mentioned version. As it is seen from "c" diffractogram of fig.1, the sample diffraction picture at the given temperature is simpler than one obtained at  $T=770\text{K}$ . Moreover, the comparison of these two diffractograms shows that all peaks observable on diffractogram  $T=850\text{K}$  is the exact repeating of part of reflections taking place on diffractograms at  $T=770\text{K}$ , namely in interval  $T=750-850\text{K}$  the investigated substance is in mixture state of two lattices differentiating by structure (see table 2-3).



The treatment of diffraction data obtained at  $T=850\text{K}$  using TOPAS program shows that sample at this temperature is to cubic phase with lattice periods  $6,061\text{\AA}$ ,  $V=223.3\text{\AA}^3$ ,  $Z=4$ , sp.gr.Pa-3. Taking off the list the two-phase diffraction data of the cubic phase reflections the rest reflections of diffractogram at  $T=770\text{K}$  are identified by TOPAS program. The process of reflection indication shows that second phase crystallizes in hexagonal syngony with periods:  $a=4,231\text{\AA}$ ,  $c=7,223\text{\AA}$ ,  $V=112,0527$ , sp.gr  $P6_3/mmc$ ,  $Z=2$ . This is the structure by  $\beta\text{-Cu}_2\text{S}$  type. We suppose that investigated sample desintegrates in two equal parts at  $T=770\text{K}$  by  $\text{Cu}_4\text{Te}_{1.5}\text{Se}_{0.5} \rightarrow \text{Cu}_2\text{Te} + \text{Cu}_2(\text{SeTe})_{0.5}$  reaction. Near  $T=800\text{K}$  both these phases joining with each other transforms into one unique cubic phase which is above mentioned.

Table 2.  
Roentgen-diffraction data for  $\text{Cu}_4\text{Te}_{1.50}\text{Se}_{0.50}$  at  $773\text{K}$ .

$N_0$	$2\theta$	$d_{\text{rec}}$	$I/I_0$	$hkl$
1	24.28	3.6633	24	1 0 0 <sup>♦</sup>
2	24.64	3.6017	20	0 0 2 <sup>♦</sup>
3	25.48	3.4929	80	1 1 1 <sup>□</sup>
4	27.28	3.2664	20	1 0 1 <sup>♦</sup>
5	29.51	3.0251	14	2 0 0 <sup>□</sup>
6	36.35	2.4603	8	2 1 1 <sup>□</sup>
7	42.28	2.1395	100	2 2 0 <sup>□</sup>
8	42.72	2.1150	14	1 1 0 <sup>♦</sup>
9	44.91	2.0178	10	1 0 3 <sup>♦</sup>
10	49.96	1.8267	27	3 1 1 <sup>□</sup>
11	52.34	1.7488	2	2 2 2 <sup>□</sup>
12	61.23	1.5174	3	4 0 0 <sup>□</sup>
13	64.42	1.3879	3	3 3 1 <sup>□</sup>
14	73.15	1.2925	5	2 1 2 <sup>♦</sup>
15	77.18	1.2386	5	4 2 2 <sup>□</sup>

♦ is Hexagonal phase  $a=4,231\text{\AA}$ ,  $c=7,223\text{\AA}$  . $P6_3/mmc$   
□ is Cubic phase  $K$   $a=6,061\text{\AA}$ ,  $V=223.3\text{\AA}^3$ ,  $Z=4$ , sp.gr.Pa-3.

Table 3.  
Roentgen-diffraction data for  $\text{Cu}_4\text{Te}_{1.50}\text{Se}_{0.50}$  at  $900\text{K}$ .

$N_0$	$2\theta$	$d_{\text{rec}}$	$I/I_0$	$hkl$
1	25.471	3.4951	100	1 1 1
2	29.445	3.0261	14	2 0 0
3	36.355	2.4711	8	2 1 1
4	42.21	2.1431	70	2 2 0
5	49.545	1.8341	28	3 1 1

In conclusion note that the different low-temperature structures form in  $\text{Cu}_4\text{Se}_{1-x}\text{Te}_x$  ( $x=0.25; 0.50; 0.75$ ) solid solutions in dependence on atom processes Se/Te [7] and therefore, their structural transitions occur on different scheme. For example, the trigonal  $\alpha$ -phase with  $\text{Cu}_4\text{Se}_{1.5}\text{Te}_{0.5}$  periods:  $a_h=4,162\text{\AA}$ ,  $c_h=20.660\text{\AA}$  in temperature interval  $300\text{--}1250\text{K}$  has the only one phase transition. At  $T=558\text{K}$   $\alpha$ -phase transits into cubic structure with period  $a=5,899\text{\AA}$  [8]. For solid solutions of  $\text{Cu}_4\text{SeTe}$  and  $\text{Cu}_4\text{Te}_{1.5}\text{Se}_{0.5}$  compositions the trigonal structure with lattice periods  $a_h=4,1880\text{\AA}$ ,  $c_h=41,8531\text{\AA}$  [9] and  $a_h=8,2319\text{\AA}$ ,  $c_h=21,4145\text{\AA}$  [10] correspondingly is established. These phases aren't isostructural ones. Their structures differ from each other. The first structure is the structure polytype form of  $\text{NaCu}_6\text{Se}_4$  type structure [11] and second phase is ordered structure of  $\text{Cu}_{1.75}\text{Te}$  type [12]. The processes of the structural transformation are also different for them. In  $\text{Cu}_4\text{SeTe}$  and  $\text{Cu}_4\text{Se}_{0.5}\text{Te}_{1.5}$  in temperature interval  $T=300\text{--}1250\text{K}$  the phase transformation process is accompanied by composition desintegration. For  $\text{Cu}_4\text{SeTe}$  at  $T=573\text{K}$  the sample decomposes in  $\text{Cu}_2\text{Se}_{0.5}\text{Te}_{0.5}$  having structure of Novotny phase type [13] with space group  $P6/mmm$  and  $\text{Cu}_2\text{Te}$  having cubic structure. The next transition corresponds to temperature  $T=673\text{K}$ . At this temperature the situation is similar as one at  $T=573\text{K}$ . The two-phase state keeps but hexagonal phase of  $\text{Cu}_2\text{Se}_{0.5}\text{Te}_{0.5}$  composition transits into to structure with sp.gr.  $P6_3/mmc$  of  $\beta\text{-Cu}_2\text{S}$  type [14]. The further heating at  $T=735\text{K}$  shows that these both phases transit into unique cubic phase with period  $a=6,05\text{\AA}$ .

As it is above mentioned the sample of composition decomposes in two phases at  $T=750\text{K}$ . Moreover, the process is identical with the one at  $T=673\text{K}$  observed for  $\text{Cu}_4\text{Se}_{0.5}\text{Te}_{0.5}$ . In given case the two-phase state higher  $T=800\text{K}$  transits into unique cubic phase  $a=6,06\text{\AA}$ .

## CONCLUSION

1. The solid solution of  $\text{Cu}_4\text{Te}_{1.5}\text{Se}_{0.5}$  composition is synthesized and it is defined by roentgenophase analysis that it crystallizes in trigonal syngony with lattice periods  $a_h=8,2319(11)\text{\AA}$ ,  $c_h=21,4145(23)\text{\AA}$ ,  $V=1089,811(12)\text{\AA}^3$ , sp.gr.  $P3m1$ ,  $Z=22$ ,  $\rho_x=7,33\text{ gr/cm}^3$ .

2. By high-temperature roentgen-diffraction method it is established that in  $300 < T < 1250\text{K}$  temperature interval the substance at  $750 \pm 5\text{K}$  decomposes in hexagonal and cubic phases of  $\text{Cu}_2\text{Se}_{0.5}\text{Te}_{0.5}$  and  $\text{Cu}_2\text{Te}$  compositions with lattice periods  $a_h=4,231\text{\AA}$ ,  $c_h=7,223\text{\AA}$  and  $a=6,049\text{\AA}$  correspondingly.

3. It is observed that in further heating the two-phase system higher  $850\text{K}$  transits into unique cubic phase.

[1] G. Krill, P. Panissod, M.F. Lapierre, F. Gautier, C. Robert, Nassr Eddine. M., J.Phys. C.9 (1976), 1521.  
[2] G.P. Sorokin. Izvestiya VUZ, Fizika, №4, (1965), 140-143.

[3] V.V. Qorbacev. Poluprovodnikovie soedineniya  $A_2B^VI$ . M.: Metallurgiya, (1980), 132 s. (In Russian).  
[4] B.A. Mansour, B.S. Farag, S.A. Khodier. Thin Solid Films, 247 (1994) 112.

- [5] *Yu.G. Asadov, Yu.I. Aliyev, A.Q. Babaev.* Fizika elementarnix castich i atomnoqo yadra, t.46, vip. 3, (2015), 812-853. (In Russian).
- [6] *Yu.G.Asadov, K.M.Jafarov, L.V.Rustamova.* Phase Transitions, v.38, (1992) , 247-259.
- [7] *A.S. Pashinkin, L.M. Pavlov, and R.A. Amirov.* p-T Phase diagram of the system Copper-Tellurium, Izv. Akad. Nauk SSSR, Neorg. Mater., v.21, №12., (1985), 2088-2091.
- [8] *N.A. Gasimova, I.R. Amirasanov, Y.I. Aliyev, G.G. Guseinov.* AIP Conf.Proc. 1400, (2011), 476-479.
- [9] *N.A. Aliieva, G.G. Guseinov, V.A. Gasymov, Yu.I. Aliyev, T.R. Mekhtiev.* Inorganic Materials, v.51, №7, 661-664.
- [10] *N.A. Aliieva, Yu.I. Aliyev, G.G. Guseynov, A.B. Maqerramov.* «Fundamentalnie I prikladnie voprosi fiziki», Trudi mejdunarodnoy konferenchii 14-15 noyabrya, Tashkent 2013, 75-76. (In Russian).
- [11] *Mihai Sturza, Christos D. Malliakas, Daniel E. Bugaris, Fei Han, Duck Young Chung and Mercouri G. Kanatzidis.* Inorg.Chem., 53 (2014), 12191-12198.
- [12] *R.B. Baronova, P.B.Баронова.* Kristalloqrafiya, (1967),t.12,vip.2. s. 266. (In Russian).
- [13] *V. H. Nowotny, Z. Metallkunde.* V. 37, (1946), 40.
- [14] *N.B. Belov, B.A. Butuzov.* Dokl. AN SSSR. t.54, № 8, (1946), 721. (In Russian).

*Received: 16.12.2015*

# THERMORECOMBINATION WAVES EXTRINSIC SEMICONDUCTORS WITH TWO TYPES OF CHARGE CARRIES

E.R. GASANOV, A.V. ISLAMZADE

BSU, Institute of Physics Problems<sup>1</sup> Az- 1143, Baku, Z.Khalilov street, 23

ANAS Institute of Physics<sup>2</sup> Az- 1143, Baki, H.Javid ave. 131

aygul\_islamzade@mail.ru

It is theoretically shown that a non-stable thermorecombination wave propagates in semiconductors with the singly and doubly negatively charged impurity centers in the presence of constant electric field and constant temperature gradient. The frequency and increment of the thermorecombination wave are calculated. An analytic formula for the constant external electric field at which the wave instability begins is found.

**Key words:** frequency, increment, electric field, temperature gradients, impurity centers.

**PACS:** 80.40.H

## INTRODUCTION

In paper [1], it is shown that hydrodynamic motion in non-equilibrium plasma, in which there is a temperature gradient  $\vec{\nabla}T$ , results in the magnetic field excitation. In that paper, it is found that the plasma with a temperature gradient  $\vec{\nabla}T$  has oscillatory characteristics noticeably different from normal plasma. In the absence of external magnetic field and hydrodynamic motion in the plasma, transverse "thermo-magnetic" waves are possible, in which oscillations of the magnetic field alone take place. If there is a constant external magnetic field  $\vec{H}_0$ , then the wave vector of the thermo-magnetic wave must be perpendicular to it and lie in the  $(\vec{H}_0, \vec{\nabla}T)$  plane.

In paper [2], conditions for the occurrence of thermo-magnetic wave instability in solid plasma with a single type of charge carriers (electrons) have been analyzed theoretically.

In paper [3-5], the instability conditions in the isotropic and anisotropic solid-state media with charge carriers of a single type have been theoretically derived. However, conditions for the occurrence and instability of thermo-magnetic waves in extrinsic semiconductors with two types of charge carriers remain indeterminate.

It is clear that the determination of instability condition in specific impurity semiconductors is of great scientific interest. In this theoretical paper we investigate conditions for the occurrence of non-stable thermorecombination waves in extrinsic semiconductors with two types of charge carriers.

## BASIC EQUATIONS

In the presence of electric field  $\vec{E}$ , of gradients of the electron  $n_-$  and hole  $n_+$  concentrations, and

temperature gradient  $\vec{\nabla}T$ , the current density for electrons and holes is of the form [1]:

$$\vec{j}_- = -\frac{\sigma_- \vec{E}^*}{e} + \frac{\sigma_{1-}}{e} [\vec{E}^* \vec{H}] - \alpha_- \vec{\nabla}T - \alpha'_- [\vec{\nabla}T \vec{H}] \quad (1)$$

$$\vec{j}_+ = -\frac{\sigma_+ \vec{E}^*}{e} + \frac{\sigma_{1+}}{e} [\vec{E}^* \vec{H}] - \alpha_+ \vec{\nabla}T - \alpha'_+ [\vec{\nabla}T \vec{H}] \quad (2)$$

$$\vec{E}^* = \vec{E} + \frac{T}{e} \left( \frac{\vec{\nabla}n_-}{n_-} - \frac{\vec{\nabla}n_+}{n_+} \right) \quad (3)$$

$$\vec{j} = \vec{j}_- + \vec{j}_+, \quad \sigma_{\pm} = en_{\pm}\mu_{\pm}, \quad \sigma_{1\pm} = en_{\pm}\mu_{1\pm} \quad (4)$$

Substituting equations (1), (2) and (3) in the equation (4), and using Maxwell equation  $\text{rot}\vec{H} = \frac{4\pi}{c} \vec{j}$ , we obtain the following expression for electric field:

$$\vec{E} = -\Lambda' [\vec{\nabla}T \vec{H}] + \frac{c}{4\pi\sigma} \text{rot}\vec{H} + \frac{T}{e} \left( \frac{\vec{\nabla}n_-}{n_-} - \frac{\vec{\nabla}n_+}{n_+} \right) + \Lambda \vec{\nabla}T \quad (5)$$

Here

$$\Lambda = \frac{\alpha_- - \alpha_+}{\sigma}; \quad \Lambda' = \frac{\alpha'_- \sigma - \alpha'_+ \sigma'}{\sigma^2}$$

$$\sigma = \sigma_+ + \sigma_-; \quad \sigma'_1 = \sigma'_{1+} - \sigma'_{1-};$$

$$\alpha = \alpha_- - \alpha_+; \quad \alpha' = \alpha'_- - \alpha'_+$$

A detailed description of mathematical method, which enable (5) to be obtained from vector equation (1-4) is given in paper [1]. In (5), the quadratic terms in magnetic field and the diffusion terms are neglected because in semiconductors  $k_0 T \ll e E_0 \ell_{\pm}$  where  $k_0$  is the Boltzmann constant,  $\ell_{\pm}$  — mean free path for holes and electrons, and  $E_0$  is external constant electric field.

In extrinsic semiconductors the kinetic equations, which take the recombination and generation of charge carriers into account, must be added to equation (5) for electric field.

Certain impurities in semiconductors create centers which can be in several charged states. For example, Au

atoms in Ge can be singly positively charged as well as singly, doubly and triply negatively charged centers, and besides that they can be in neutral state.

Several energy levels in the band gap correspond to such centers. Depending on their charged states, these energy levels (impurity centers) can capture electrons or holes. As a result of such capture, concentrations of electrons (in the conduction band) and holes (in the valence band) change, therefore the electrical conduction in semiconductor also changes.

In various experimental conditions, these impurity centers are more or less active, so the recombination and generation proceed generally via a certain number of impurity centers. For example, in experiment [6] (we will use its results), singly and doubly negatively charged Au centers in Ge were active centers.

In the presence of an electric field, electrons and holes gain energy on the order of  $eE_0 \ell_{\pm}$  (where  $e$  is the positive elementary charge) due to the electric field. Therefore, in the presence of the electric field, electrons can overcome the Coulomb barrier of the singly charged center and be captured. Electrons can also be generated owing to thermal transitions from impurity centers to the conduction band. The number of holes increases due to the capture of electrons from the valence band by impurity centers, and decreases due to the capture of electrons from impurity centers by holes. The probability of charge carrier generation and the probability of charge carrier recombination are different, and it leads to the change in concentrations of electrons and holes in semiconductors. A detailed description of kinetic equations for electrons and holes in the above-mentioned semiconductor was given in paper [7]. These equations are of the following form:

$$\frac{\partial n_{-}}{\partial t} + \text{div} \vec{j}_{-} = \gamma_{-}(0)n_{1-}N_{-} - \gamma_{-}(E)n_{-}N = \left( \frac{\partial n_{-}}{\partial t} \right)_{\text{rec}} \quad (6)$$

$$N_0 = N_{-} + N_{+} = \text{const} \quad n_{1-} = \frac{n_{-}^0 N_0}{N_{-}^0} \quad (7)$$

Here  $N_0$  is a total concentration of the singly negatively charged centers  $N$  and the doubly negatively charged centers  $N_{-}$ , and  $n_{1-}$  is a characteristic concentration found on condition that

$$E_0 = 0, \quad \left( \frac{\partial n_{-}}{\partial t} \right)_{\text{rec}} = 0 \quad (8)$$

$$\frac{\partial n_{+}}{\partial t} + \text{div} \vec{j}_{+} = \gamma_{+}(E)n_{1+}N - \gamma_{+}(0)n_{+}N_{-} = \left( \frac{\partial n_{+}}{\partial t} \right)_{\text{rec}} \quad (9)$$

$$n_{1+} = \frac{n_{+}^0 N_{-}^0}{N_0}$$

In equations (6-10),  $\gamma_{-}(0)$  is the coefficient of electron emission by the doubly negatively charged centers in the absence of electric field,  $\gamma_{-}(E)$  is the coefficient of electron capture by the singly negatively charged centers, and  $\gamma_{+}(0)$  is the coefficient of hole capture by the doubly negatively charged centers. The variation in the doubly negatively charged traps with time determines the variation in the singly negatively charged centers. Therefore, the equation determining the variation in charged centers with time is of the form:

$$\frac{\partial N_{-}}{\partial t} = \left( \frac{\partial n_{+}}{\partial t} \right)_{\text{rec}} - \left( \frac{\partial n_{-}}{\partial t} \right)_{\text{rec}} \quad (10)$$

In order to obtain the  $\omega(k)$  dispersion relation, the set of equations (5), (6), (7), (9) and (10) must be solved simultaneously, taking into account the Maxwell equation

$$\frac{\partial \vec{H}}{\partial t} = -c \text{rot} \vec{E} \quad (11)$$

where  $c$  is the velocity of light.

For this purpose, we linearize the set (5-10) in the following way:

$$\vec{E} = \vec{E}_0 + \vec{E}; \quad n_{\pm} = n_{\pm}^0 + n'_{\pm}; \quad \vec{\nabla} T = \text{const}$$

$$(\vec{E}', n'_{\pm}) \sim e^{i(\vec{k}\vec{r} - \omega t)}$$

$$\vec{E}' \ll \vec{E}_0; \quad n'_{\pm} \ll n_{\pm}^0 \quad (12)$$

Here  $\vec{k}$  is a wave vector, and  $\omega$  is the wave frequency. Substituting equation (11) into (5), we get:

$$\vec{E} = -\frac{c\Lambda'}{\omega} [\vec{\nabla} T [\vec{k}\vec{E}']] + \frac{ic^2}{4\pi\omega\sigma} [\vec{k} [\vec{k}\vec{E}']] + \frac{iE_1 \vec{k}}{k} \left( \frac{n'_{-}}{n_{-}^0} - \frac{n'_{+}}{n_{+}^0} \right) + \Lambda \vec{\nabla} T \quad (13)$$

Linearizing equation (10), we get:

$$N'_- = \frac{N^0 \lambda \frac{\vec{E}' \vec{E}_0}{2} + \omega_-(E_0) n'_- - \omega_+(0) n'_+}{\nu - i\omega} \quad (14)$$

Here

$$\begin{aligned} \nu &= \nu_+ + \nu_- = \gamma_+(E_0) n_{1+} + \gamma_+(0) n'_+ + \gamma_-(0) n_{1-} + \gamma_-(E_0) n_-^0 \\ \lambda &= \gamma_+(E_0) n_{1+} \varphi_+ + \gamma_-(E_0) n_-^0 \varphi_-; \quad \omega_-(E_0) = \gamma_-(E_0) N^0, \quad \omega_+(0) = \gamma_+(0) N_-^0 \\ \varphi_{\pm} &= 2 \frac{d\hbar \sigma_{\pm}}{d\hbar(E_0^2)}; \\ \text{div} \vec{j}'_{\pm} &= \left[ \pm \frac{i\sigma_{\pm}^0 \delta_{\pm}}{e} + \frac{ic\sigma_{1\pm}}{e} (\vec{k} \vec{E}_0) \right] - \frac{ic\sigma_{1\pm}}{e\omega} (\vec{E}_0 \vec{E}') + \frac{\sigma_{\pm}^0 E_1 k}{e} \left( \frac{n'_-}{n_-^0} - \frac{n'_+}{n_+^0} \right); \\ E_1 &= \frac{Tk}{e}; \\ \theta_{\pm} &= 2 \frac{d\hbar \alpha_{\pm}}{d(E_0^2)}; \quad \delta_{\pm} = 1 \pm \varphi_{\pm} \end{aligned} \quad (15)$$

Expanding the vector products in (13), we get:

$$\begin{aligned} \left( 1 + \frac{\omega_T}{\omega} + \frac{ic^2 k^2}{4\pi\sigma_0\omega} \right) \vec{E}' &= -\frac{c\Lambda' \vec{k} (\vec{\nabla} T \vec{E}')}{\omega} + \frac{ic^2 \vec{k} (\vec{k} \vec{E}')}{4\pi\omega\sigma_0} + \frac{iE_1 \vec{k}}{k} \left( \frac{n'_-}{n_-^0} - \frac{n'_+}{n_+^0} \right) + \vec{\nabla} T \Lambda U \frac{\vec{E}_0 \vec{E}'}{E_0^2}, \\ U &= 2 \frac{d\hbar \Lambda}{d\hbar E_0^2} \end{aligned} \quad (16)$$

where  $\omega_T = -c\Lambda' \vec{k} \vec{\nabla} T$  is the frequency of thermo-magnetic waves [1]. Multiplying (15) scalar wise at first by  $\vec{E}_0$  and after that by  $\vec{k}$ , we can easily get:

$$\begin{aligned} \vec{E}_0 \vec{E}' &= iE_0 E_1 a \left( \frac{n'_-}{n_-^0} - \frac{n'_+}{n_+^0} \right); \quad \vec{k} \vec{E}' = iE_1 k a \left( \frac{n'_-}{n_-^0} - \frac{n'_+}{n_+^0} \right) \\ a &= \frac{\Lambda' ck}{\omega_T \Lambda U \cos \alpha} \quad (\vec{E}_0 \vec{k}) = E_0 k \cos \alpha \end{aligned} \quad (17)$$

It should be noted that  $\alpha \neq \infty$  and so in the expression for  $a$  one cannot assume  $\alpha = 90^\circ$ . Hereinafter we will omit superscript 0 of the equilibrium quantities  $n_{\pm}^0, N^0, E_0$ . Substituting (15-17) into the set (6-9), we get:



$$\left\{ -i\omega - iku_+a + \lambda_+(0) + \omega_+(E_0) \frac{n_{1+}}{n_+} \varphi_+ + \frac{iaE_1}{E} - \frac{\nu_+}{\nu_- i\omega} [i\lambda_+ + \omega_+(0)] \right\} n'_+ +$$

$$+ \left\{ iku_+a \frac{n_+}{n_-} + \frac{n_+}{n_-} ku_{1+} - \omega_+(E_0) \frac{n_{1+}}{n_+} \varphi_+ + \frac{iaE_1}{E} + \frac{\nu_+}{\nu_- i\omega} [i\lambda_- + \omega_-(E_0)] \right\} n'_- = 0 \quad (18)$$

$$\left\{ i \frac{n_-}{n_+} ku_-a - \frac{n_+}{n_-} ku_{1-} - \omega_-(E_0) \frac{n_-}{n_+} \varphi_- + \frac{iaE'}{E} + \frac{\nu_-}{\nu_- i\omega} [i\lambda_+ + \omega_+(0)] \right\} n'_+ +$$

$$+ \left\{ -i\omega - iu_-ka + \lambda_-(E) + \omega_-(E_0) \varphi_- + \frac{iaE'}{E} - \frac{\nu_-}{\nu_- i\omega} [i\lambda_- + \omega_-(E_0)] \right\} n'_- = 0 \quad (19)$$

Here

$$\lambda \frac{aE'}{E} \frac{N}{n_-} = \lambda_-; \quad \frac{N}{n_+} \frac{aE'}{E} = \lambda_+ \quad \omega_+(0) - u_{1+}k = \lambda_+(0) \quad \omega_-(E_0) + u_{1-}k = \lambda_-(E)$$

Let us write equations (18) and (19) in the following form:

$$\begin{cases} \lambda_1 n'_+ + \lambda_2 n'_- = 0 \\ \lambda_3 n'_+ + \lambda_4 n'_- = 0 \end{cases} \quad (20)$$

$$\lambda_1 \lambda_4 - \lambda_2 \lambda_3 = 0 \quad (21)$$

Substituting  $\lambda_1, \lambda_2, \lambda_3, \lambda_4$  from equations (18-19) into (21), we get an equation determining the frequency and increment of “thermorecombination” wave:

$$\omega^2 + i(A_- + A_+) \omega + B_+ B_- - A_+ A_- = 0 \quad (22)$$

$$A_- = -iku_-a + \lambda_-(E_0) + \omega_-(E_0) \varphi_- + \frac{iaE'}{E}$$

$$A_+ = iku_+a \frac{n_+}{n_-} + \frac{n_+}{n_-} ku_{1+} - \omega_+(E_0) \varphi_+ + \frac{iaE'}{E}$$

$$B_- = iku_-a \frac{n_-}{n_+} - \frac{n_-}{n_+} ku_{1-} - \omega_-(E_0) \frac{n_-}{n_+} \varphi_- + \frac{iaE'}{E}$$

$$B_+ = iku_+a \frac{n_+}{n_-} + \frac{n_+}{n_-} ku_{1+} - \omega_+(E_0) \frac{n_{1+}}{n_-} \varphi_+ + \frac{iaE'}{E} \quad (23)$$

It is too complicated to solve the equation (22) taking into account (23), so we will solve the equation (22) for certain analytical expressions of the external electric field. It is easy to verify that if  $A_- = A_+$  then

$$E = \frac{\omega_+(0) \varphi_- \left[ 1 - \frac{\mu_- k E'}{\omega_+(0)} - \frac{\omega_+(E)}{\omega_+(0)} \frac{n_{1+}}{n_+} \frac{\varphi_+}{\varphi_-} \right]}{k \mu_- \left( \delta_- + \frac{\omega_T}{ck} r_- + \frac{\omega_T}{ck} \frac{\mu_+}{\mu_-} r_+ \right)} \quad (24)$$

$$r_- = \frac{\alpha_- \theta_- \vec{E}_0 \vec{\nabla} T}{E^2 n_- \mu_-}; \quad r_+ = \frac{\alpha_+ \theta_+ \vec{E} \vec{\nabla} T}{E^2 n_+ \mu_+}; \quad \frac{B_-}{B_+} = \left( \frac{\nu_-}{\nu_+} \right)^2 \quad (25)$$

Taking into account (24-25), from (22) we get:

$$\omega_{1,2} = -iA_- \pm iB_+ \frac{v_-}{v_+} \quad (26)$$

Substituting  $A_-$  and  $B_+$ , we get the following expressions for the frequency and increment of thermorecombination wave:

$$\omega_1 = -ku_-a + \omega_-(E_0)\varphi_- \frac{aE'}{E} - \frac{v_-}{v_+} ku_+a \frac{n_+}{n_-} + \frac{v_-}{v_+} \omega_+(E) \frac{n_+}{n_-} \varphi_+ \frac{aE'}{E} +$$

$$+ i \left[ \frac{v_-}{v_+} \frac{n_+}{n_-} ku_{1+} - \lambda(E) \right] \quad (27)$$

$$\omega_2 = -ku_-a + \omega_-(E_0)\varphi_- \frac{aE'}{E} + \frac{v_-}{v_+} ku_+a \frac{n_+}{n_-} - \frac{v_-}{v_+} \omega_+(E) \frac{n_+}{n_-} \varphi_+ \frac{aE'}{E} -$$

$$- i \left[ \frac{v_-}{v_+} \frac{n_+}{n_-} ku_{1+} + \lambda(E) \right] \quad (28)$$

### ANALYSIS OF THE OBTAINED RESULTS

As follows from (26-27), the wave with frequency  $\omega_2$  (28) is a damped wave, and there is no energy emission from the above-mentioned semiconductor at the frequency  $\omega_2$ . Emission from the above-mentioned semiconductor occurs if the wave increment

$$\omega_1 = \frac{v_-}{v_+} \frac{n_+}{n_-} ku_{1+} - \lambda_-(E) \quad (29)$$

is positive, and a high hole concentration and a low electron concentration are required for that. One can see from (27)  $\omega = \omega_0 + i\omega_1$  that  $a \sim \frac{1}{\omega_1}$ . The thermo-

magnetic waves decrease frequencies of thermorecombination wave, and the frequency of electron

capture and the frequency of hole emission increase frequencies of thermorecombination wave.

Probably, there are values of  $\omega_{\pm}(E_0)$  and  $\omega_T$  at which semiconductors with the above-mentioned model emit energy nearly stable. Such a situation can occur at certain values of the external electric field and the constant temperature gradient.

The presence of constant and alternating magnetic field can change conditions of the thermorecombination wave generation. When energy is emitted from a medium, a resistance of the medium decreases and the current variations in external circuit occur. For investigation of external instability (i.e. when the real part of impedance is negative  $\text{Re } z < 0$ ), the impedance of semiconductor has to be calculated. This problem requires taking into account the boundary conditions across electric field at ends of the medium and of course the injection at ends of the medium.

- 
- |  |  |
|--|--|
| <p>[1] <i>L.E. Gurevich</i>. Thermomagnetic waves and the excitation of a magnetic field in a nonequilibrium plasma. Soviet Physics JETP, 1963, Vol. 17, No.2, pp. 373-377 [J. Exptl. Theoret. Phys. (U.S.S.R.), 1963, 44, 548-555].</p> <p>[2] <i>L.E. Gurevich and B.L. Gel'mont</i>. Hydrothermomagnetic waves in a weakly inhomogeneous plasma. Soviet Physics JETP, 1965, Vol. 20, No.5, 604-614 [J. Exptl. Theoret. Phys. (U.S.S.R.) 1964, 46, 884-901].</p> <p>[3] <i>L.E. Gurevich and V.I. Vladimirov</i>. Kinetic properties of a low-density plasma with large radiation pressure and electron-phonon drag. Soviet Physics JETP, 1963, Vol. 17, No.1, pp.116-122 [J. Exptl. Theoret. Phys. (U.S.S.R.) 1963, 44, 166-176].</p> | <p>[4] <i>E.R. Hasanov, M.F. Novruzov, A.Z. Panahov, A.I. Demirel</i>. Energy generation and amplitude of thermo-magnetic waves in the conducting medium. Modern Physics Letters B, 2008, Vol.22, No.6, pp. 455-457.</p> <p>[5] <i>E.R. Hasanov, M.F. Novruzov, A.Z. Panahov, A.I. Demirel</i>. Instability of thermo-magnetic waves in the Ge Au Semiconductors with impurities. International Journal of Pure and Applied Physics, 2008, Vol. 4, No. 1, pp. 23-28.</p> <p>[6] <i>M.I. Iglitsyn, E.G. Pel', L.Ya. Perova, V.N. Fistul'</i>. FTT, 1966, Vol. 8, No. 12, pp.3606-3612.</p> <p>[7] <i>L.E. Gurevich and E.R. Gasanov</i>. Theory of spontaneous oscillations of current in crystals with deep traps. FTT, 1962, Vol. 11, p.1433.</p> |
|--|--|

Received: 06.12.2015

# ELEMENTARY PROCESSES IN KINETICS OF MECHANICAL FAILURE OF PP-PELD POLYMER COMPOSITIONS

I.K. ALIYEVA<sup>1</sup>, P.B. ASILBEYLI<sup>2</sup>, T.M. VELIYEV<sup>3</sup>, E.S. SAFIYEV<sup>4</sup>, A.A. KHADIYEVA<sup>2</sup>

<sup>1</sup>Azerbaijan Naval Academy,

<sup>2</sup>Institute of Physics of Azerbaijan National Academy of Sciences, AZ1143, Baku, Azerbaijan, H.Javid ave.,131

<sup>3</sup>Odlar Urdu University, Az1071, Baku, K.Ragimova str.,13

<sup>4</sup>Azerbaijan Oil Academy, Baku, Azdalig ave.,20

e-mail: [asilbeyli@mail.ru](mailto:asilbeyli@mail.ru)

The distribution of optimal polymer compositions of low density polypropylene-polyethylene PP-PELD on  $\tau$  mechanical durability, which is the rupture waiting time (mechanical failure at constant voltage) is measured. The test results of continuous field action on samples with discontinuous one, saving them in intact state after endurance during the time corresponding to  $\lg t$  average value, are compared. The action duration and temperature are varied, that's why the different regeneration degree of strength of polymer compositions is observed. It is shown that the accumulated changes, which are identified as fluctuating rupture of chain molecules, are reversal ones in the case of mechanical failure of polymer compositions.

**Keywords:** polymer compositions, mechanical failure, supramolecular structure, over-barrier transition, failure kinetics

**PACS:** 81.05.Rm

## INTRODUCTION

The sample rupture under action of applied mechanical load are the final acts of developing processes in loaded objects preparing the appearance of continuity macroscopic loss. Many experimental data on observation of so-called "late failure" when sample rupture doesn't become at once after application of some constant mechanical load, but after some time the duration of which depends on mechanical load value and also on series of other factors (temperature, structural object state, environment, radiation interaction and etc) indicate it [1].

We can conclude that during this time the changes take place in loaded object, processes leading to total loss of object stability to load action develop in one. Thus, the mechanical failure isn't the critical accident but there is kinetic phenomenon.

The questions of reversibility and irreversibility of elementary processes preparing the body rupture are the important ones.

The revealing of reversibility degree of accumulated processes in mechanical failure kinetics of polymer compositions is carried out for this purpose.

## EXPERIMENT TECHNIQUE AND SAMPLE PREPARATION

The samples from polymer optimal compositions low density polypropylene-polyethylene (PP-PELD) in percent ratio 80/20, correspondingly with different submolecular structures (SMS) are taken in the capacity of investigation objects. The film thickness is the several decades of micrometers.

The measurements of mechanical durability are carried out on tearing machine in which the temperature value and tension stress are given for each sample and the time interval from load moment up to sample rupture is defined. The durability value in time interval from several seconds up to  $10^5$  sec is measured.

The durability measurement of samples series not less 30 is carried out for each combination voltage-temperature because of the character essential spread of durability values at measurements

The investigation of reversibility degree of accumulation processes leading to mechanical failure is carried out on the base of known method which is the comparison of durability measurement results at continuous action of mechanical load with durability measurement results at discontinuous action. Note that quantitative analysis of test results of similar type for polymer mechanical failure is carried out but not for polymer compositions and without necessary account of durability statistics [2].

Thereto, the measurements of mechanical durability ( $\tau$ ) of polymer compositions PP-PELD are carries out in series from 30 samples in present work because these measurements with the discontinuous action of mechanical load on single samples don't give the possibility to analyze the sample distribution functions on mechanical durability.

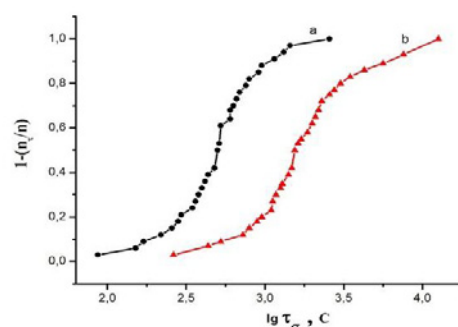


Fig. 1. The integral distribution of polymer composition samples on durability. The mechanical failure of 30 samples at  $T=223K$ .

a) SC samples of PP-PELD,  $\sigma=80$  MPa;

b) RC samples of PP-PELD,  $\sigma=90$  MPa.

The integral functions of distribution for slowly cooled (SC) and rapidly cooled (RC) samples of PP-PELD correspondingly on  $\lg \tau$  at corresponding mechanical load ( $\sigma$ ) and temperature ( $T$ ) are shown in fig.1 (a,b).

The function  $1 - n_\tau/n$ , where  $n$  is total number of samples in series is given on ordinate axis;  $n_\tau$  is number of samples saved in intact state after  $\tau$  endurance time. As it is seen the plots of these functions for  $\tau$  in both compositions has the unified S-form with effective distribution width  $\Delta \lg \tau \approx 1 \div 1.5$ . The distribution form is close to normal distribution of random variable (probability integral). The distribution width is caused by structure variation and sample imperfection and etc. The mechanical durability values appropriating to failure of half number of samples for SC and RC of PP-PELD,  $\tau_1 = 504$  sec and  $\tau_1 = 1590$  sec correspondingly, are defined from fig.1(a,b). Further, the new series of the same samples are endured at the same  $\sigma$  and  $T$  values during  $\tau_1$  time correspondingly, after that the load ( $\sigma$ ). As a result, the half number of samples, with which the further operations are carried out, stay in intact state. The meaning and method of data analysis is diagrammatically explained in fig.2.

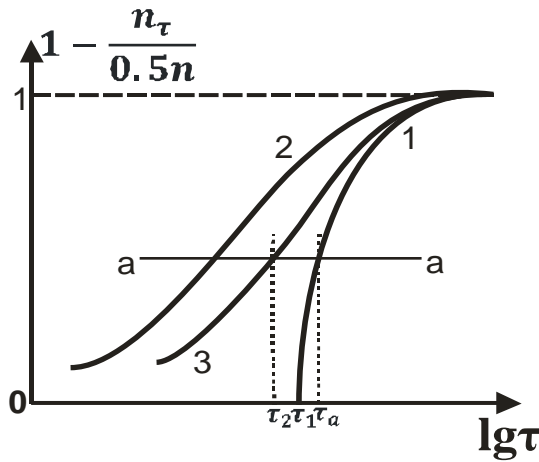


Fig.2. The distribution scheme of polymer composition samples PP-PELD by durability is: 1. Samples which become indifferent ones after endurance during  $\tau_1$  time; 2. The distribution by secondary durability  $\lg(\tau - \tau_1)$ ; 3. Samples treated by partial regeneration.

Here the curve 1 is upper part of distribution curves (fig.1), i.e. it is constructed from level 0,5 in fig.1 and renormalized one on total number of samples (with ordinate  $1 - n_\tau/0,5n$ , which are not broken. If we propose that accumulated changes in samples, which are not broken, during interruption time are disappeared (total regeneration) after endurance under mechanical load during  $\tau_1$  time, then the distribution of these samples on secondary durability should coincide with curve 1 after secondary application of the same load. If the accumulated changes are totally kept during interruption time after endurance during  $\tau_1$  and load taking off, then sample distribution on secondary durability should obtain by reconstruction curve 1 from values  $\lg \tau$  to  $\lg(\tau - \tau_1)$  ones and has the form of curve 2 (fig.2), i.e. in the region of lesser  $\tau$  values, especially in the region of distribution

initial (low) part. Finally, if partial regeneration of accumulated changes takes place in the interval between load taking off and its repeated application in the samples, then the sample distribution on secondary durability should take place between 1 and 2 curves, i.e. correspond to curve 3. The distributions on durability at continuous load action for slow cooling (SC) PP-PELD samples with durability exceeding  $\tau_1 = 504$  sec, i.e. renormalized upper parts of distribution curves from  $n$  on  $0,5n$  (fig.1).

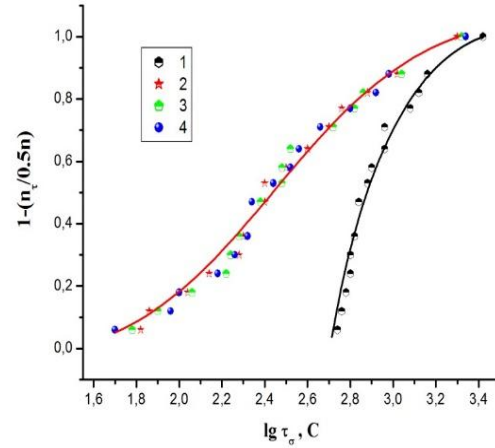


Fig. 3. The integral distribution of SC samples PP-PELD on mechanical durability.  $\sigma = 80$  MPa,  $T = 223$  K.

1 is failure during time exceeding  $\tau_1 = 504$  sec; 2 is distribution of the same samples on  $\lg(\tau - \tau_1)$ ; 3 is measured sample distribution on secondary durability after “resort” during  $10^3$  sec at 223 K; 4 is measured sample distribution on secondary durability after “resort” during  $10^3$  sec at 323 K (regeneration absence).

Points 3 are reconstruction results of points 1 on coordinate  $\lg(\tau - \tau_1)$ . Points 3 are experimental data on secondary durability after sample endurance under load during time  $\tau_1$  and load interruption time  $10^3$  sec at 223 K. The closeness of 2 and 3 points in fig.3 evidences on fact that changes accumulate in samples during  $\tau_1$  of first endurance under load. These changes keep in load interruption time at the same temperature that leads to lower values of secondary durability. The corresponding data for RC samples PP-PELD are similar ones, i.e. the accumulated changes in both samples behave as irreversible ones under conditions of mechanical failure kinetics at comparatively low temperatures.

For mechanical failure during the “resort” the samples are endured at the exceeded temperatures. The results of such tests when unloaded SC samples of compositions are endured at 323 K during  $10^3$  sec in interval are presented in fig.3 (points 4). It is seen that “resort” temperature increase doesn’t lead to change of sample distribution on secondary durability, i.e. change regeneration doesn’t observed. This allows us to conclude that changes caused by action of mechanical load are the enough stable ones. The earlier mentioned irreversibility of accumulated changes at mechanical failure of polymer compositions [2] is confirmed in present work. This well agrees with conception on accumulation of chain

molecule rupture during the time. Especially the rupture act chain molecules at mechanical stress carried out by fluctuation mechanism, behaves itself in the capacity of elementary failure act of polymers and compositions on the base polymer-polymer [1].

The further polymer failure process is developed on the base of such molecular ruptures: the formation of germ cracks and rupture of whole sample [1]. It is natural that recombination of chain molecule rupture is enough incredibly, so the secondary free-radical reactions, "convolution" of molecule parts unloaded by rupture prevent to regeneration of its continuity [1,3] after rupture. In this fact we can see the specific of polymer failure process and their compositions. Note that continuity regeneration at mechanical failure of three-

dimensional atom-molecular structure bodies, in particular, metal is possible [4]. At corresponding conditions (temperature, pressure) we can reconstruct the initial continuity of objects ("cure" of accumulating micro-cracks and pores) and whereas to multiply increase of their mechanical durability.

## **CONCLUSION**

The results of our investigation are data on character of accumulation processes leading to rupture of polymer compositions with confirmation of irreversibility of these processes in the case of mechanical failure of polymer compositions obtained on the base of statistical analysis of mechanical durability.

- 
- [1] *B.L. Qilyarov*. FTT 2005, t.45, №5, s.808-811. (In Russian).  
[2] *A.I. Sluchker, T.M. Veliev, I.K. Alieva, V.A. Alekperov, S.A. Abasov*. FTT 1990, t.32, №8, s.2399-2344. (In Russian).  
[3] *V.A. Zakrevskiy, V.A. Paxotin*. FTT, 2010,t.52, №6, s.1083-1089. (In Russian).  
[4] *V.I. Betextin, A.I. Ormanov*. FMM 1989, t.67, №5, s.318-322. (In Russian).

*Receved: 07.10.2015*



# STRUCTURAL INVESTIGATIONS OF $\text{Zn}_{1.5}\text{In}_3\text{Se}_6$ POLYTYPE 3R BY MEANS OF NEW ELECTRON-DIFFRACTION ROTATION METHODS

M.G. KYAZUMOV, L.V. RUSTAMOVA

*Institute of Physics of Azerbaijan NAS*

*AZ1143 H.Javid ave., 131, Baku*

*elmira@physics.ab.az, [el\\_max63@yahoo.com](mailto:el_max63@yahoo.com)*

The electron-diffraction pattern of monocrystalline films (MF)  $\text{Zn}_{1.5}\text{In}_3\text{Se}_6$ , obtained by rotation of MF round axis perpendicular to film plane, which earlier is inclined on  $\varphi$  angle from perpendicular position to incident electron beam and also electron-diffraction pattern obtained by MF rotation round  $a^*$  axis of reciprocal lattice perpendicular located to electron beam, are studied. The thin structural effects and different series appear separately on electron-diffraction patterns obtained by new rotation methods as opposed to electron-diffraction patterns of oblique textures where the thin structural effects appear and different series of reflexes superimpose one on another. The three-package rhombohedral polytype (3R) with crystal lattice parameters  $a = 4.046 \text{ \AA}$ ,  $c = 59.292 \text{ \AA}$ , sp. gr.  $R3m$  and also superlattice parameter  $A_{s,1} = \sqrt{3} a$  are found.

**Keywords:** new rotation methods, electron diffraction, inorganic compound structure

**PACS:** 61.05.-a, 61.14.-x, 61.66.Fn.

## INTRODUCTION

The electron-diffraction methods are more effective ones to investigate of layered crystals. The development of nanotechnology stimulates the design of new electron-diffraction methods having the specific advantages to investigate of nanosamples. The present paper is devoted to study of nanothick monocrystalline films (MF)  $\text{Zn}_{1.5}\text{In}_3\text{Se}_6$  by new electron-diffraction rotation methods [1-4]. Earlier the three-package rhombohedral polytype (3R) is defined by electron-diffraction patterns of  $\text{Zn}_{1.5}\text{In}_3\text{Se}_6$  textured samples [5].

## EXPERIMENTAL PART AND RESULT DISCUSSION

$\text{Zn}_{1.5}\text{In}_3\text{Se}_6$  crystals synthesized by ChTR (chemical transport reaction), are divided into two parts perpendicularly to layers. The crystalline structure of one of them is studied by method of oblique texture. The samples for experiment are obtained by precipitation of micro-crystals (obtained by easy comminution with further dispergation by ultrasound) from suspension in water on metallic grid covered by celluloid film. The one orientation remains constant, in connection with layered structure of crystals, after the crystal precipitation from the suspension in water on the film. The experiment is carried out on high-voltage electronograph EG-400 ( $V=350\text{kV}$ ,  $2L\lambda=33,2\text{mm}\text{\AA}$ ).

The electron-diffraction patterns from  $\text{Zn}_{1.5}\text{In}_3\text{Se}_6$  textures is shown in fig.1. The electron-diffraction pattern interpretations are made by the following formulas for oblique textures [6]:

$$d_{100} = 3a/4 = 2L\lambda h/2R_{h00}, \quad (1)$$

$$D_{hk\ l} = (R_{hkl}^2 - R_{hk0}^2)^{1/2}, \quad (2)$$

$$D = c * L\lambda = (D_{hkl} - D_{hk(l-1)}), \quad (3)$$

$$d_{001} = c = 1/c^* = L\lambda/\Delta D. \quad (4)$$

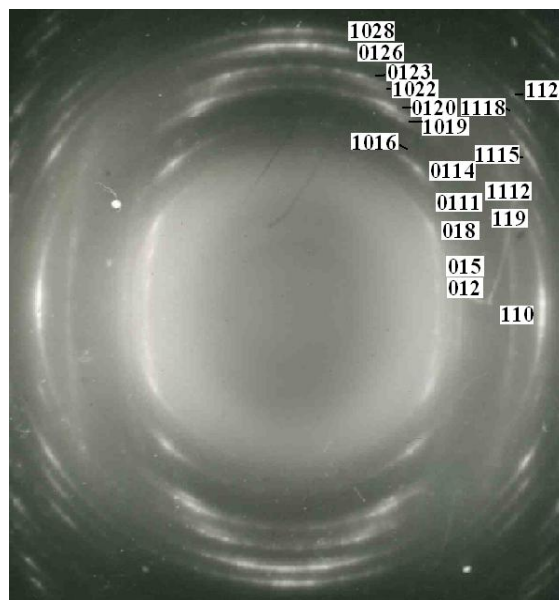


Fig.1. Electron-diffraction pattern of  $\text{Zn}_{1.5}\text{In}_3\text{Se}_6$  textures.

The polytype 3R with elementary cell parameters  $a = 4.046$ ,  $c = 59.292 \text{ \AA}$ , sp. gr.  $R3m$  and with structure module  $\dots_h\text{T}_c\text{T}_h\text{O}_h\text{T}_c\text{T}_h\text{P}\dots$ , where T and O are two-dimensional tetrahedral and octahedral layers, P is empty interlayer,  $h$  and  $c$  are hexagonal and cubic package of Se atomic planes, is established.

The metal disposition (a,b,c positions) in compact selenium package (A,B,C positions) is following:

$\dots\text{AbBaCcApCaAcBbCbBcCbAaBp}\dots$ ,

$\dots\text{Se}_1 \ 2/3\text{In}; 1/3\text{Zn} \ \text{Se}_2 \ 1/3\text{In}; 0,42\text{Zn} \ \text{Se}_3 \ \text{In} \ \text{Se}_4 \ 1/3\text{In}; 0,42\text{Zn} \ \text{Se}_5 \ 2/3\text{In}; 1/3\text{Zn} \ \text{Se}_6 \ \text{P}\dots$

The other part of  $\text{Zn}_{1.5}\text{In}_3\text{Se}_6$  crystal is used for obtaining of thin MF, suitable for electron-diffraction investigation.

The thin MF are obtained by film exfoliation from thick crystal by the adhesive tape.

The thin MF are studied by electron-diffraction rotation methods developed by M.G.Kazumov [1-4].

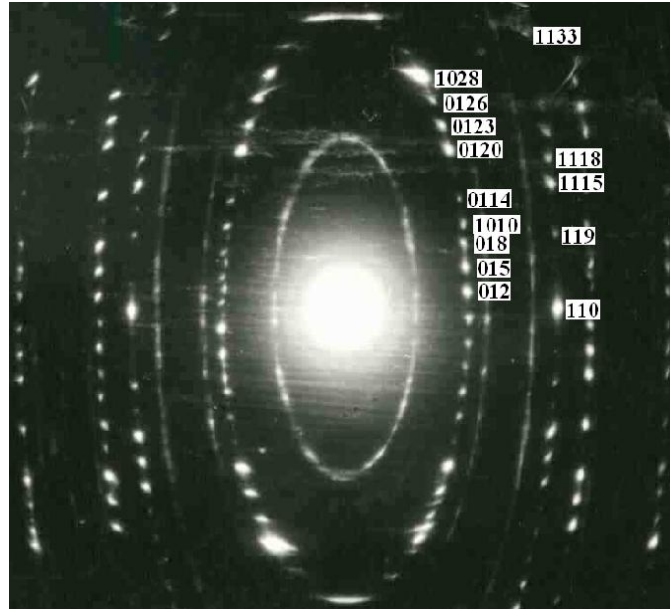


Fig.2. Electron-diffraction pattern of monocrystalline rotation imitating the electron-diffraction patterns of  $\text{Zn}_{1.5}\text{In}_3\text{Se}_6$  oblique texture type.

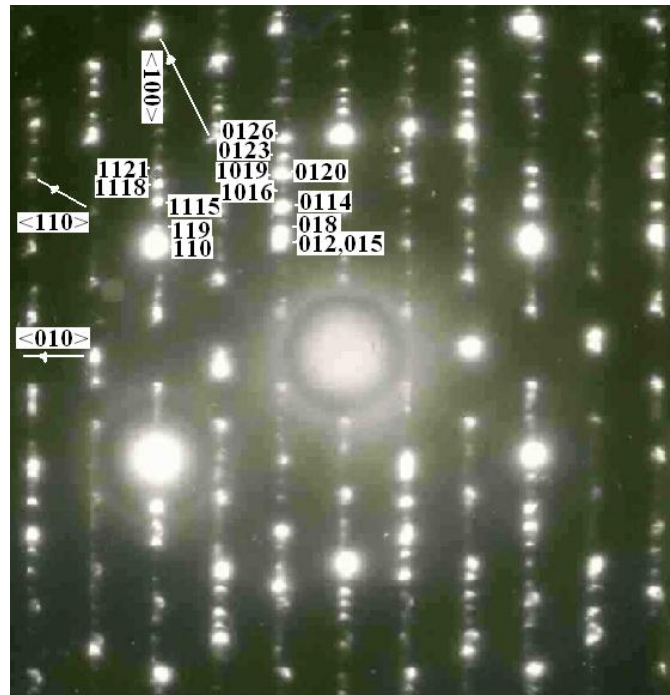


Fig.3. Electron-diffraction pattern of 3R-polytype  $\text{Zn}_{1.5}\text{In}_3\text{Se}_6$  rotating round axis of  $a^*$  reversal lattice.

The electron-diffraction pattern obtained by rotation (during exposition) of MF film on  $\omega = 60^\circ$  angle round axis perpendicular to film plane which is previously inclined to incident electron beam on angle  $\varphi = 60^\circ$  (reciprocal lattice plane  $hk0$  is in MF plane), is shown in fig.2. The main crystal lattice parameters  $a = 4.046 \text{ \AA}$ ,  $c = 59.292 \text{ \AA}$ , sp. gr.  $R3m$  and also superlattice parameter  $A_{s,1} = \sqrt{3}a$  in basic plane of main lattice, are found. The reflexes being on weak ellipses which are first, third, fourth, seventh, eighth and other ones are to superlattice.

The reflexes being on the strong ellipses, which are second, fifth, sixth, ninth and other ones are to main lattice. The reflex intensities in fig.1 coincide with ones of corresponding reflexes of main lattice (fig.2) and it shows the structure identity (fig.2).

The electron-diffraction pattern obtained by rotation of MF film  $\text{Zn}_{1.5}\text{In}_3\text{Se}_6$  round  $a^*$  axis of reversal lattice perpendicularly situated to electron beam, is shown on fig.3. The registration is begun from  $hk0$  plane; the essential delay of this plane under electron beam is admitted. The polytype 3R with above mentioned lattice

parameters and super lattice is observed. The different node series (series of reflexes) appear separately but the nodes with  $l$  small values join each other in each node series  $hk$  ( $h, k = \text{const}, l$  changes). The quantity of joined reflexes depends on value and on distance of node row and on rotation  $c^*$  axis, i.e. on sp.  $R_{hk0}$ .

## CONCLUSION

The electron-diffraction patterns of monocrystal rotation (EMR) have the additional advantage series besides the texture ones have. EMR give the concrete-local diffraction and structural information relating to isolated crystals and electron-diffraction patterns from

textures give the integral averaged information relating to crystal variety. In EMR the higher sensitivity to weak diffraction effects, which can't be observed in electron-diffraction patterns of textures and polycrystals, is observed. The reflexes in EMR localize in the point form and they spread in the form of parenthesis or total rings in electron-diffraction patterns of textures and polycrystals.

The other advantage is the possibility to avoid the consequence of object dispergation accompanying to preparation of polycrystals and textures. It can not only destroy the crystalline structure perfection, but lead sometimes to phase transformations. So, for example, the graphite comminution causes the polytype transition 2H-3R.

- 
- [1] B.B. Zvyagin, A.P. Juxlistov, M.Q. Kyazumov, A.M. Fominenkov. Kristalloqrafiya, **35**, №3 (1990) 602-609. (In Russian).
  - [2] M.Q. Kyazumov i dr. Sposob poluceniya elektronogram tipa kosix tekstur tonkix plastinchatix kristallov. Avtorskoe svidetelstvo № 1649397 (1991). (In Russian).
  - [3] M.G. Kyazumov. New electron diffraction rotation methods. Acta Cryst. **A.68** (2012) 61.
  - [4] M.Q. Kyazumov. Kristalloqrafiya, **59** (2014) 549-555. (In Russian).
  - [5] A.G. Abdullayev, M.G. Kyazumov, A.Sh. Khidirov. An electron diffraction study of the  $\text{ZnIn}_2\text{Se}_4$  crystal structure. A novel phase. Thin Solid films, **190** (1990) 309-315.
  - [6] B.B. Zvyagin. Elektronografiya i strukturnaya kristalloqrafiya qlinistix mineralov. M.: Nauka, 1964, - 312 s. (In Russian).

Received: 09.12.2015

# REEXAMINATION A TIME-DEPENDENT LINEAR POTENTIAL IN THE QUANTUM MECHANICS

Sh.M. NAGIYEV<sup>1</sup>, K.Sh. JAFAROVA<sup>1</sup>, A.I. KAZIMOVA<sup>2</sup>

<sup>1</sup>*Institute of Physics, Azerbaijan National Academy of Sciences,*

*Javid av. 131, Az-143, Baku, Azerbaijan,*

<sup>2</sup>*Gandja State University, H.Aliyev av. 187, AZ-2000, Gangja, Azerbaijan*

*E-mail: [smnagiyev@physics.ab.az](mailto:smnagiyev@physics.ab.az)*

We reexamine the complete solutions of the Schrödinger equation for a particle with time-dependent mass moving in a time-dependent linear potential on the base of the evolution operator method. We solve the problem in both, configuration and momentum spaces. Appropriately choosing the initial wave functions we can obtain from the representation  $\psi(t)=U(t)\psi(0)$  all kinds of wave functions of the system under consideration, in particular, those solutions which are known in the literature. For example, it is shown that evolution operator can be used to obtain the Gaussian-type, Airy-type and oscillator-type wave-packet solutions of the time-dependent system. The explicit form for the initial momentum and coordinate operators (two linear independent invariants)  $\hat{p}_0(t)$  and  $\hat{x}_0(t)$  are found. We show that the problem of a particle moving in a linear potential is unitary equivalent to that of a free particle.

**Keywords:** Time-dependent linear potential, evolution operator, invariants

**PACS:** 03.65.-w, 03.65.Fd, 02.30.Tb

## 1. INTRODUCTION

During the past several decades the analytical solutions of the Schrödinger equation with the time-dependent linear potential have attracted much attention of physicists [1-8]. To study the time-dependent quantum systems there are many methods, such as LR invariant method [9, 12], path-integral method [10], space-time transformations method [5], evolution operator method [11], etc. For instance, in Ref. [1] using the Feynman's path-integral method the solution of the time-dependent linear potential problem in the form of the Airy function was presented and was shown that the Airy packet propagates without change of form. The Wigner function and exact transition amplitude between energy eigenstates for a particle in a general time-dependent linear potential was calculated in Ref. [3]. In Ref. [4], Guedes with the help of the LR invariant method solved the time-dependent Schrödinger equation for the linear potential of the particular form  $V(x,t)=qx(\varepsilon_0+\varepsilon\cos\omega t)$ . Feng [5] followed the space-time transformations of the Schrödinger equation and found plane-wave type and the Airy-packet type solutions. Later Luan et al. [6] used a non-Hermitian linear LR invariant to obtain Gaussian-type wave-packet solutions of the system. Bekkar et al. [7] gave a general solution of the Schrödinger equation with the time-dependent linear potential, which corresponds to the linear LR invariant  $I_1=A(t)\hat{p}+B(t)\hat{x}+C(t)$ .

The purpose of the present paper is to undertake a completely analytical solution for the problem above by means of the evolution operator method. This method has long time been used

to solve problems in quantum mechanics and quantum field theory. We demonstrate that the evolution operator method allows us to find, in principle, all (infinitely many) solutions of this problem, including those solutions which are known in the literature [1-7]. Therefore, it can be argued that all known solutions [1-7] are in fact partial

solutions to the problem under consideration. We show that a complete set of Lewis-Riesenfeld (LR) invariants for this problem is not limited to linear and quadratic invariants. The reason for this may formulate as follows: according to the evolution operator method, the solutions of the time-dependent Schrödinger equation  $\hat{S}(t)\psi(t)=0$  can be represented as  $\psi(t)=U(t)\psi(0)$ , where  $\hat{S}(t)=i\hbar\partial_t-H(t)$  and  $\psi(0)$  is any function (initial wave function). The evolution operator  $U(t)$  satisfies the Schrödinger equation  $\hat{S}(t)U(t)=0$  with the initial condition  $U(0)=1$ . One can expand the function  $\psi(0)$  over some complete set of the orthogonal functions  $\{\psi_n(0)\}$ :  $\psi(0)=\sum_n c_n\psi_n(0)$ . Then the wave function at arbitrary time  $t$  can be given as  $\psi(t)=\sum_n c_n\psi_n(t)$ , where  $\psi_n(t)=U(t)\psi_n(0)$ . (In the case of expansion in the Fourier integral  $\psi(0)=\int g(\lambda)e^{i\lambda x}d\lambda$  for the wave function at time  $t$  we obtain an expression  $\psi(t)=\int g(\lambda)\psi_\lambda(t)d\lambda$ , where  $\psi_\lambda(t)=U(t)e^{i\lambda x}$ .)

It is well known [12] also that one can construct two (for one-dimensional system) linearly independent simple invariants  $\hat{p}_0(t)$  and  $\hat{x}_0(t)$ , provided that the evolution operator for a quantum system exists:

$$\begin{aligned}\hat{p}_0(t) &= U(t)\hat{p}U^{-1}(t), \\ \hat{x}_0(t) &= U(t)\hat{x}U^{-1}(t).\end{aligned}\tag{1.1}$$

They are the operators of initial momentum and coordinate. All other invariants can be expressed in terms of these operators. Recall that the invariant  $I(t)$  is the operator which should commute with the Schrödinger

operator  $[\hat{S}(t), I(t)] = 0$ , yielding the analogous to (1.1) expression for  $I(t)$ :

$$I(t) = U(t)I(0)U^{-1}(t). \quad (1.2)$$

It is clear that if  $I(0) = G(\hat{p}, \hat{x})$ , then  $I(t) = G(\hat{p}_0(t), \hat{x}_0(t))$ .

On the other hand, according to the LR invariant method [9], the solutions of the time-dependent Schrödinger equation can be constructed in terms of the eigenstates  $\varphi_n(t)$  of the LR invariant  $I(t)$  with the time-independent eigenvalues  $\lambda_n$ :  $I(t)\varphi_n(t) = \lambda_n\varphi_n(t)$ . The function  $\varphi_n(t)$  does not satisfy the Schrödinger equation, but it is an eigenfunction of the operator  $\hat{S}(t)$ :  $\hat{S}(t)\varphi_n(t) = s_n(t)\varphi_n(t)$ . A solution of the Schrödinger equation is chosen as

$$\psi_n(t) = e^{i\alpha_n(t)}\varphi_n(t), \quad (1.3)$$

where the phase  $\alpha_n(t)$  is a function of time only. It follows from the Schrödinger equation for  $\psi_n(t)$  that  $\alpha_n(t)$  satisfies the relation

$$\alpha_n(t) = \hbar^{-1} \int_0^t s_n(t') dt'. \quad (1.4)$$

One can obtain the state (1.3) also from the eigenstate  $\varphi_n(0)$  of the operator  $I(0)$  with the same eigenvalue  $\lambda_n$  by means of the evolution operator  $U(t)$ :

$$\psi_n(t) = U(t)\varphi_n(0) = e^{i\alpha_n(t)}\varphi_n(t). \quad (1.5)$$

Thus, the evolution operator  $U(t)$  transforms any eigenstate of  $I(0)$  into an eigenstate of  $I(t)$ , or, more precisely, into a solution of the Schrödinger equation.

The initial wave function  $\psi(0)$  can be expanded over the complete set of the eigenfunctions  $\{\varphi_n(0)\}$  of the operator  $I(0)$ , thereby the solution of the Schrödinger equation is obtained as:

$$\psi(t) = \sum_n c_n U(t)\varphi_n(0) = \sum_n c_n e^{i\alpha_n(t)}\varphi_n(t). \quad (1.6)$$

The solution, obtained in [7], corresponds to an expansion over the eigenfunctions of the linear invariant  $I_1(0) = A_0\hat{p} + B_0\hat{x} + C_0$  at  $B_0 = 0$ , i.e. over the plane waves, which can be understood as a usual Fourier transformation.

It is clear that there may exist other operators  $I(0)$ , with complete set of the eigenfunctions, and one can expand  $\psi(0)$  over this complete set. One of such kind operator is

$$I_3(0) = A_0 \cosh\left(\frac{a\hat{p}}{\hbar}\right) + B_0 x(x + ia)e^{-\frac{a\hat{p}}{\hbar}}, \quad (1.7)$$

which is Hamiltonian of the relativistic linear harmonic oscillator [14,15]. The eigenfunctions of  $I_3(0)$  are expressed through the Meixner-Pollaczek polynomials

$$\varphi_n(0) = N_n A_0^{-ix/a} \Gamma(\nu - ix/a) P_n^\nu(x/a; \pi/2), \quad (1.8)$$

where  $\nu = \frac{1}{2} + \sqrt{\frac{1}{4} + A_0^2}$ ,  $a = (2A_0B_0)^{-1/2}$ . The

operators  $K_0 = I_3(0)$ ,  $K_1 = -x/a$  and

$K_2 = -I_3(0) + A_0 \exp\left(\frac{a\hat{p}}{\hbar}\right)$  form the Lee algebras (1.1),

i.e.  $[K_0, K_1] = iK_2$ ,  $[K_1, K_2] = -iK_0$ .

Thus, now it becomes clear that the complete solution of the Schrödinger equation with the time-dependent linear potential is not exhausted by the results of [1-8]. We will consider, as in [5], a more general case, i.e., a particle with time-dependent mass moving in the time-dependent linear potential. This time-dependent dynamical problem could be solved in either configuration or momentum space. It can be found that the all known in the literature solutions [1-8] are merely the particular cases in comparison with our result. We also note that in the evolution operator method there is no further problem of finding time-dependent phase, inherent LR invariant method. The derivation of the exact wave functions is straightforward and is obtained with much less effort than other results [1-7] based on the other methods.

The main results of this paper are as follows. First, we give an explicit form of the evolution operator  $U(t)$  in the  $x$ - and  $p$ -representations for the Schrödinger equation describing the motion of a particle with the time-dependent mass in the time-dependent linear potential (Sec. II). Second, we show that all known solutions can be derived from a general representation for the wave function  $\psi(t) = U(t)\psi(0)$  (Sects. II, III, IV). Since the time-dependent system in the initial time can be in any state, the corresponding Schrödinger equation has infinitely many solutions.

However, appropriately choosing an initial wave function, one can always construct a solution of the Schrödinger equation with the required properties. For example, in Sec. V we obtained the square-integrable oscillator-like solutions. Third, we find the explicit form of the initial momentum and the initial coordinate operators  $\hat{p}_0(t)$  and  $\hat{x}_0(t)$ , through of which all other invariants can be expressed (Sec. III).

We show that the complete set of the LR invariants for the system under consideration is not restricted by the linear and quadratic invariants (Sec. VI).

Fourth, we have shown that a problem of a particle that moves in a linear potential and a free particle problem are unitarily equivalent.



## 2. CONFIGURATION SPACE

The Schrödinger equation for describing the motion of a particle with time-dependent mass in the presence of time -dependent linear potential is of the form

$$i\hbar\partial_t\psi(x,t) = \left[ -\frac{\hbar^2}{2M(t)}\partial_x^2 - F(t)x \right] \psi(x,t) \quad (2.1)$$

where  $M(t)$  and  $F(t)$  are arbitrary time-dependent functions. The solution of the equation (2.1) may be obtained from the evolution operator  $U(x,t)$

$$\psi(x,t) = U(x,t)\psi(x,0). \quad (2.2)$$

The explicit form of the operator  $U(x,t)$  was found in [15]

$$U(x,t) = e^{\frac{ix\delta(t)}{\hbar}} e^{-\frac{i}{\hbar}\int_0^t \frac{1}{2M(t')} [-i\hbar\partial_x + \delta(t')]^2 dt'} \quad (2.3)$$

in which the notation  $\delta(t) = \int_0^t F(t')dt'$  is used. Now

taking into account (2.3) in (2.2), one gets a following general representation for the solution of the Schrodinger equation (2.1)

$$\psi(x,t) = e^{\frac{i}{\hbar}[x\delta(t)-s_0(t)]} e^{-s_1(t)\partial_x} e^{i\hbar s_2(t)\partial_x^2} \psi(x,0), \quad (2.4)$$

where  $s_i(t)$  ( $i=0, 1, 2$ ) are defined, respectively, as

$$s_0(t) = \int_0^t \frac{\delta^2(t')}{2M(t')} dt', \quad s_1(t) = \int_0^t \frac{\delta(t')}{M(t')} dt',$$

$$s_2(t) = \int_0^t \frac{dt'}{2M(t')}. \quad (2.5)$$

If we set  $M(t)=m$ , we will find that

$$s_0(t) = \frac{\delta_2(t)}{2m}, \quad s_1(t) = \frac{\delta_1(t)}{m}, \quad s_2(t) = \frac{t}{2m}, \quad (2.6)$$

$$\text{Where } \delta_1(t) = \int_0^t dt' \int_0^{t'} F(t'') dt'' = \int_0^t \delta(t') dt',$$

$$\delta_2(t) = \int_0^t dt' \left[ \int_0^{t'} F(t'') dt'' \right]^2 = \int_0^t \delta^2(t') dt'.$$

A particular form of the evolution operator  $U(x,t)$ , when  $M(t)=m$  and  $F(t)=F_0$  was given in [8]. In this case we have  $\delta(t)=F_0 t$ ,  $\delta_1(t)=F_0 t^2/2$ ,  $\delta_2(t)=F_0^2 t^3/3$ . Now choosing in (2.4) different initial wave functions  $\psi(x,0)$  one can construct different wave functions  $\psi(x,t)$  at time  $t > 0$ .

For example, appropriately choosing the initial wave function we obtained from (2.4) all known in the literature solutions [1-8] of the equation (2.1) as the special cases:

1)  $\psi(x,0) = N$ . In this case we easily get

$$\psi(x,t) = N e^{\frac{i}{\hbar}[x\delta(t)-s_0(t)]}, \quad (2.7)$$

where  $N$  is a normalization constant. To compare with the solution in Ref. [4], we let  $F(t)$  take the form  $-q(\varepsilon_0 + \varepsilon \cos \omega t)$ , and set  $M(t)=m$ , which yields

$$\delta(t) = -\frac{q}{\omega}(\varepsilon_0 \omega t + \varepsilon \sin \omega t),$$

$$s_0(t) = \frac{q^2}{2m\omega^3} \left[ \frac{\varepsilon_0(\omega t)^3}{3} + 2\varepsilon_0(\sin \omega t - \omega t \cos \omega t) + \frac{1}{2}\varepsilon^2(\omega t - \frac{1}{2}\sin 2\omega t) \right]. \quad (2.8)$$

Substituting these expressions in (2.7), we obtain the solution of (18) in [4]

$$\psi(x,t) = N \exp \left[ -\frac{iq}{\hbar\omega}(\varepsilon_0 \omega t + \varepsilon \sin \omega t)x \right] \times$$

$$\times \exp \left\{ -\frac{iq^2}{2m\hbar\omega^3} \left[ \frac{\varepsilon_0(\omega t)^3}{3} + 2\varepsilon_0(\sin \omega t - \omega t \cos \omega t) + \frac{1}{2}\varepsilon^2(\omega t - \frac{1}{2}\sin 2\omega t) \right] \right\}. \quad (2.9)$$

2)  $\psi(x,0) = e^{iAx} / \sqrt{2\pi}$ , where  $A$  is an arbitrary real number. In this case using (A.3) one can obtain the following expression for the wave function

$$\psi(x, t) = \frac{1}{\sqrt{2\pi}} e^{iA[x-s_1(t)]} e^{-i\hbar s_2(t)A^2} e^{\frac{i}{\hbar}[x\delta(t)-s_0(t)]}, \quad (2.10)$$

which coincides with the formula (6) in [5].

3)  $\psi(x, 0) = Ai(Bx)$ , where  $B$  is an arbitrary constant and  $Ai(x)$  denotes the Airy function. In this case, after some simple transformations in (2.4) with the help of the formula (A6) can be shown that

$$\begin{aligned} \psi(x, t) = & e^{\frac{i}{\hbar}[x\delta(t)-s_0(t)]} e^{i\hbar s_2(t)B^3[x-s_1(t)] - \frac{2}{3}i\hbar^3 s_2^3(t)B^6} \times \\ & \times Ai\left(B\left[x - s_1(t) - \hbar^2 s_2^2(t)B^3\right]\right). \end{aligned} \quad (2.11)$$

This result is equivalent to formula (8) of Ref. [5].

Note that the formula (15) of Ref. [1] [17] corresponds to the following initial condition  $\psi(x, 0) = Ai(Bx/\hbar^{2/3})$  and, therefore, it is obtained from (2.11) by replacing  $B \rightarrow B/\hbar^{2/3}$  and  $M(t) \rightarrow m$ . By choosing the initial wave function in the form  $\psi(x, 0) = Ai\left(-[2mF_0/\hbar^2]^{1/3}[x + E/F_0]\right)$  one gets the formula (24) of Ref. [3].

In the next two Sections we obtain a general solution of the Schrodinger equation (2.1) by the evolution operator method, which yields the results of [6, 7] as a particular cases.

### 3. INVARIANTS FOR THE TIME-DEPENDENT LINEAR POTENTIAL

Knowledge of the evolution operator (2.3) allows us to find not only the wave functions, but also to construct the LR invariants for the system. In the case of the time-dependent linear potential we have the following general expressions for the invariants (1.1)

$$\begin{aligned} \hat{p}_0(t) &= \hat{p} - \delta(t), \\ \hat{x}_0(t) &= \hat{x} - 2s_2(t)\hat{p} + 2\delta(t)s_2(t) - s_1(t). \end{aligned} \quad (3.1)$$

All other invariants are expressed through them. For example,

$$I_1(t) = A_0\hat{p}_0(t) + B_0\hat{x}_0(t) + C_0 \equiv A(t)\hat{p} + B(t)\hat{x} + C(t), \quad (3.2a)$$

$$\begin{aligned} I_2(t) &= D_0^2\hat{p}_0^2(t) + K_0\hat{x}_0^2(t) \equiv \\ &\equiv D(t)\hat{p}^2 + E(t)(\hat{p}\hat{x} + \hat{x}\hat{p}) + K(t)\hat{x}^2 + A'(t)\hat{p} + B'(t)\hat{x} + C'(t), \end{aligned} \quad (3.2b)$$

$$I_3(t) = A_0 \cosh\left(\frac{a\hat{p}_0(t)}{\hbar}\right) + B_0\hat{x}_0(t)[\hat{x}_0(t) + ia]e^{\frac{a\hat{p}_0(t)}{\hbar}}. \quad (3.2c)$$

At  $M(t) = m$  the invariants constructed in Refs.[4, 6, 7] are obtained from (3.1) and (3.2a).

a) Let us find with the help of the evolution operator a particular solution of the Schrodinger equation (2.1), corresponding to the linear invariant (3.2a) at  $B_0 = 0$ . For this purpose, as the initial wave function we choose the eigenvector of the operator  $I_1(0)$  at  $B_0 = 0$  corresponding to the eigenvalue  $\lambda$ , which has the form

$$\varphi_\lambda(x, 0) = e^{\frac{i}{\hbar}\lambda_1 x}, \quad \lambda_1 = (\lambda - C_0)/A_0. \quad (3.3)$$

From (2.3), (2.4) and (3.3), we then get the solution of the equation (2.1):

$$\psi_\lambda(x, t) = U(x, t)e^{\frac{i}{\hbar}\lambda_1 x} = \exp\left\{-\frac{i}{\hbar} \int_0^t \frac{1}{2M(t')} \left[\frac{\lambda - C(t')}{A_0}\right]^2 dt'\right\} \exp\left[\frac{i}{\hbar} \frac{\lambda - C(t)}{A_0} x\right], \quad (3.4)$$

where  $C(t) = -A_0\delta(t) + C_0$ . To derive the relation (3.4) we have used the formula

$$f(-i\hbar\partial_x)e^{\frac{i}{\hbar}\lambda_1 x} = f(\lambda_1)e^{\frac{i}{\hbar}\lambda_1 x}. \quad (3.5)$$

If we set  $M(t) = m$ , we will find that (3.4) coincides with the formula (12) of Ref. [7] [17].

b) We now find the general solution of equation (2.1) corresponding to the linear invariant (3.2 a) at  $B_0 = 0$ . To this end we expand the initial wave function over the plane waves (3.3), i.e.

$$\psi(x,0) = \int_{-\infty}^{\infty} g(\lambda)e^{\frac{i}{\hbar}\lambda_1 x} d\lambda, \quad (3.6)$$

where  $g(\lambda)$  is an arbitrary weight function (Fourier transform of  $\psi(x,0)$ ). Then from (2.4), (3.4) and (3.6) we obtain the desired solution of equation (2.1)

$$\psi(x,t) = \int_{-\infty}^{\infty} g(\lambda)\psi_\lambda(x,t)d\lambda, \quad (3.7)$$

(3.7) is a generalization of the formula (13) of Ref. [7] to the case of the time-dependent mass. If we now choose  $g(\lambda) = \exp(i\lambda^3/3B^3)/2\pi$  and use the integral representation of the Airy function (A.12), then we find after integrating (3.7):

$$\begin{aligned} \psi(x,t) = & B \exp \left\{ -\frac{i}{\hbar A_0} \left[ C(t)x + \frac{1}{2A_0} \int_0^t \frac{C^2(t')}{M(t')} dt' \right] \right\} \times \\ & \times \exp \left\{ \frac{iB^3}{2\hbar^2 A_0^3} \int_0^t \frac{dt'}{M(t')} \left[ x + \frac{1}{A_0} \int_0^t \frac{C(t')}{M(t')} dt' - \frac{B^3}{6\hbar A_0^3} \left( \int_0^t \frac{dt'}{M(t')} \right)^2 \right] \right\} \times \\ & \times Ai \left( \frac{B}{\hbar A_0} \left[ x + \frac{1}{A_0} \int_0^t \frac{C(t')}{M(t')} dt' - \frac{B^3}{4\hbar A_0^3} \left( \int_0^t \frac{dt'}{M(t')} \right)^2 \right] \right). \end{aligned} \quad (3.8)$$

When  $M(t) = m$  one gets from the equation (3.8) the following formula [18]

$$\begin{aligned} \psi(x,t) = & B \exp \left\{ -\frac{i}{\hbar A_0} \left[ C(t)x + \frac{1}{2mA_0} \int_0^t C^2(t') dt' \right] \right\} \times \\ & \times \exp \left\{ \frac{iB^3 S}{2\hbar^2 A_0^3} \left[ x + \frac{1}{mA_0} \int_0^t C(t') dt' - \frac{B^3 S^2}{6\hbar A_0^3} \right] \right\} \times \\ & \times Ai \left( \frac{B}{\hbar A_0} \left[ x + \frac{1}{mA_0} \int_0^t C(t') dt' - \frac{B^3 S^2}{4\hbar A_0^3} \right] \right), \end{aligned} \quad (3.9)$$

where  $S = t/m$ .

One can easily check that the functions (3.4) and (3.8) satisfy the Schrödinger equation (2.1).

#### 4. MOMENTUM SPACE

We can solve the problem in the momentum  $p$ -space by evolution operator method. We write the Schrödinger equation (2.1) in the momentum space

$$i\hbar\partial_t \Phi(p,t) = \left[ \frac{p^2}{2M(t)} - i\hbar F(t)\partial_p \right] \Phi(p,t). \quad (4.1)$$

The evolution operator in the  $p$ -space has the simple form [15]:

$$U(p, t) = e^{-\frac{i}{\hbar} \int_0^t \frac{[p - \delta(t) + \delta(t')]}{2M(t')} dt'} e^{-\delta(t) \partial_p}. \quad (4.2)$$

We now can write a symbolic solution of (4.1) by using the time evolution operator for the system

$$\Phi(p, t) = U(p, t) \Phi(p, 0), \quad (4.3)$$

or equivalently

$$\Phi(p, t) = e^{-\frac{i}{\hbar} \int_0^t \frac{[p - \delta(t) + \delta(t')]}{2M(t')} dt'} \Phi(p - \delta(t), 0). \quad (4.4)$$

Here  $\Phi(p, 0)$  is an arbitrary initial wave function in  $p$ -space. In the particular case when  $M(t) = m$  from (4.4) follows the formula (35) of Ref. [6].

As a particular example in the momentum space we obtain Gaussian-type wave-packet (GWP) solution of (4.1). We consider the initial wave function in  $p$ -space, given by [6]

$$\Phi(p, 0) = \left( \frac{2\sigma^2}{\pi \hbar^2} \right)^{1/4} \exp \left[ -\frac{\sigma^2 (p - p_0)^2}{\hbar^2} - i \frac{(p - p_0) x_0}{\hbar} \right], \quad (4.5)$$

where  $p_0$  and  $x_0$  are the average values of the momentum and coordinate in this state. After some simple algebra, we obtain from (4.4) the wave function at  $t > 0$ :

$$\begin{aligned} \Phi(p, t) = & \left( \frac{2\sigma^2}{\pi \hbar^2} \right)^{1/4} \exp \left[ -\frac{i}{\hbar} \int_0^t \frac{p_c^2(t')}{2M(t')} dt' \right] \exp \left( -\frac{\sigma^2 (1 + it/T(t))}{\hbar^2} [p - p_c(t)]^2 \right) \times \\ & \times \exp \left( -\frac{i}{\hbar} [p - p_c(t)] x_c(t) \right), \end{aligned} \quad (4.6)$$

where the functions  $p_c(t)$  and  $x_c(t)$  are defined as follows (compare with [6]):

$$p_c(t) = p_0 + \delta(t), \quad x_c(t) = x_0 + \int_0^t \frac{p_c(t')}{M(t')} dt'. \quad (4.7)$$

Here the parameter

$$T(t) = \frac{\sigma^2 t}{\hbar s_2(t)} = \frac{\sigma^2 t}{\hbar} \bigg/ \int_0^t \frac{dt'}{2M(t')} \quad (4.8)$$

indicates a time-dependent measure of the spreading time of the GWP.

In the configuration  $x$ -space the function (4.6) takes a form

$$\begin{aligned} \psi(x, t) = & \frac{1}{(2\pi)^{1/4} \sqrt{\sigma(1 + it/T(t))}} \exp \left[ -\frac{i}{\hbar} \int_0^t \frac{p_c^2(t')}{2M(t')} dt' \right] \times \\ & \times \exp \left[ -\frac{[x - x_c(t)]^2}{4\sigma^2(t)} + \frac{i}{\hbar} p_c(t) x \right], \end{aligned} \quad (4.9)$$

where  $\sigma^2(t) = \sigma^2 [1 + it/T(t)]$ . When  $M(t) = m$  we have  $T(t) = T = \frac{2m\sigma^2}{\hbar}$ ,  $x_c(t) = x_0 + [p_0 t + \delta_1(t)]/m$  and the functions (4.6) and (4.9) coincide with the solutions (38) and (40) of Ref. [6], respectively.

In what follows we wish to calculate the uncertainty relation. After some calculation we find that the uncertainties in  $x$  and  $p$  in the state  $\psi(x, t)$  (4.9) (or  $\Phi(p, t)$  (4.6)) are

$$(\Delta x)^2 = |\sigma(t)|^2 = \sigma^2 \left[ 1 + \frac{t^2}{T^2(t)} \right], \quad (4.10 \text{ a})$$

$$(\Delta p)^2 = \hbar^2 / 4\sigma^2. \quad (4.10 \text{ b})$$

Thus, the uncertainty relation is expressed as

$$(\Delta x)(\Delta p) = \frac{\hbar}{2} \sqrt{1 + t^2/T^2(t)} \geq \frac{\hbar}{2}, \quad (4.11)$$

and, in general, does not attain its minimum value. For  $M(t) = m$ , the incertainty relation (4.11) reduces to that obtained in Ref. [6].

## 5. OSCILLATOR-LIKE SOLUTIONS

The time-dependent Schrödinger equation (2.1) has various solutions. Here we find the oscillator-like solutions for this equation. To this end we choose the initial wave function  $\psi(x, 0)$  in the form of the stationary harmonic oscillator wave function, i.e.

$$\psi_n(x, t) = c_n e^{-\frac{1}{2}\lambda^2 x^2} H_n(\lambda x), \quad \lambda = \sqrt{m\omega/\hbar}, \quad (5.1)$$

where  $H_n(x)$  is Hermite polynomial,  $c_n = c_0 / \sqrt{2^n n!}$  and  $c_0 = (m\omega/\pi\hbar)^{1/4}$ . Let us substitute (5.1) into (2.4) and calculate the action of the evolution operator on the initial wave function with the help of the formula (A9). As a result, we obtain the desired oscillator-like wave functions for a particle moving in the time-dependent linear potential

$$\begin{aligned} \psi_n(x, t) = & \frac{c_n}{\sqrt{\varepsilon(t)}} \left( \frac{\varepsilon^*(t)}{\varepsilon(t)} \right)^{n/2} \exp \left\{ \frac{i}{\hbar} [x\delta(t) - s_0(t)] \right\} \times \\ & \times \exp \left\{ -\frac{\lambda^2 [x - s_1(t)]^2}{2\varepsilon(t)} \right\} H_n \left( \frac{\lambda [x - s_1(t)]}{|\varepsilon(t)|} \right). \end{aligned} \quad (5.2)$$

For each fixed  $t$  the wave functions (5.2) are orthogonal and normalized.

$$\int_{-\infty}^{\infty} \psi_n^*(x, t) \psi_m(x, t) dx = \delta_{nm}. \quad (5.3)$$

Here the following notation is introduced  $\varepsilon(t) = 1 + 2i\hbar\lambda^2 s_2(t)$ .

In the particular case when  $M(t) = m$  we have  $\varepsilon(t) = 1 + i\omega t$ . In this case, by taking into account the explicit form of the functions  $s_i(t)$  ( $i=0, 1, 2$ ), given in (2.5), one gets the following expression for the oscillator-like wave functions:

$$\begin{aligned} \psi_n(x, t) = & \frac{c_n}{\sqrt{1 + i\omega t}} \exp[-in \arctan(\omega t)] \exp \left\{ \frac{i}{\hbar} [x\delta(t) - \delta_2(t)/m] \right\} \times \\ & \times \exp \left\{ -\frac{\lambda^2 [x - \delta_1(t)/m]^2}{2(1 + i\omega t)} \right\} H_n \left( \frac{\lambda [x - \delta_1(t)/m]}{\sqrt{1 + \omega^2 t^2}} \right). \end{aligned} \quad (5.4)$$



We should like to find the wave functions (5.2) also using the LR invariant method [9, 12]. For this purpose we choose those linear combinations of the invariants (3.1) which have the form of the annihilation and creation operators:

$$\begin{aligned} A(t) &= U(t)aU^{-1}(t) = \frac{1}{\sqrt{2}} \left[ \lambda \hat{x}_1(t) + \frac{i\varepsilon(t)}{\hbar\lambda} \hat{p}_1(t) \right], \\ A^+(t) &= U(t)a^+U^{-1}(t) = \frac{1}{\sqrt{2}} \left[ \lambda \hat{x}_1(t) - \frac{i\varepsilon^*(t)}{\hbar\lambda} \hat{p}_1(t) \right], \\ [A(t), A^+(t)] &= [a, a^+] = 1 \end{aligned} \quad (5.5)$$

Here  $a$  and  $a^+$  are the usual oscillator's annihilation and creation operators

$$a = \frac{1}{\sqrt{2}} \left( \lambda x + \frac{i}{\hbar\lambda} \hat{p} \right), \quad a^+ = \frac{1}{\sqrt{2}} \left( \lambda x - \frac{i}{\hbar\lambda} \hat{p} \right) \quad (5.6)$$

and  $\hat{x}_1(t) = \hat{x} - s_1(t)$ ,  $\hat{p}_1(t) = \hat{p} - \delta(t)$ .

One now can construct a following quadratic invariant for the Hamiltonian

$$\begin{aligned} H &= -\hbar^2 \partial_x^2 / 2M(t) - F(t)x : \\ \tilde{I}_2(t) &= A^+(t)A(t) + 1/2 = \\ &= \frac{1}{2} \left[ \lambda \hat{x}_1^2(t) + \frac{|\varepsilon(t)|^2}{\hbar^2 \lambda^2} \hat{p}_1^2(t) + \frac{i}{\hbar} (\varepsilon(t) - 1) (\hat{x}_1(t) \hat{p}_1(t) + \hat{p}_1(t) \hat{x}_1(t)) \right]. \end{aligned} \quad (5.7)$$

The operators  $A(t)$  and  $A^+(t)$  have the properties

$$A(t)\varphi_n(x, t) = \sqrt{n}\varphi_{n-1}(x, t), \quad A^+(t)\varphi_n(x, t) = \sqrt{n+1}\varphi_{n+1}(x, t), \quad (5.8)$$

where the states  $\varphi_n(x, t)$  are eigenstates of the invariant  $\tilde{I}_2(t)$ , i. e.

$$\tilde{I}_2(t)\varphi_n(x, t) = (n + 1/2)\varphi_n(x, t). \quad (5.9)$$

Here the ground state is defined, as usual, by the equation  $A(t)\varphi_0(x, t) = 0$ , whose normalized solution is

$$\varphi_0(x, t) = \frac{c_0}{\sqrt{\varepsilon(t)}} \exp \left\{ \frac{i\delta(t)}{\hbar} x - \frac{\lambda^2 [x - s_1(t)]^2}{2\varepsilon(t)} \right\}. \quad (5.10)$$

It can easily be shown by induction on  $n$  that the excited states of the operator  $\tilde{I}_2(t)$  have the following explicit form

$$\begin{aligned} \varphi_n(x, t) &= \frac{1}{\sqrt{n!}} [A^+(t)]^n \varphi_0(x, t) = \\ &= \frac{c_n}{\sqrt{\varepsilon(t)}} \left( \frac{\varepsilon^*(t)}{\varepsilon(t)} \right)^{n/2} \exp \left\{ \frac{i\delta(t)}{\hbar} x - \frac{\lambda^2 [x - s_1(t)]^2}{2\varepsilon(t)} \right\} \cdot H_n \left( \frac{\lambda [x - s_1(t)]}{|\varepsilon(t)|} \right). \end{aligned} \quad (5.11)$$

The relation between the solution (5.2) of the Schrodinger equation (2.1) and the eigenfunction (5.11) of the invariant  $\tilde{I}_2(t)$  is:  $\psi_n(x, t) = \exp[-is_0(t)/\hbar]\varphi_n(x, t)$ . The fact that the functions  $\psi_n(x, t)$  and  $\varphi_n(x, t)$  differ from each other by the time-dependent phase factor  $\exp(-is_0(t)/\hbar)$  can be understood as follows: both of the operators  $U(t)$  and  $U^{-1}(t)$  contain the same phase factor but with opposite phases, therefore these phases are canceled in the construction of the  $A$  and  $A^+$  invariants.

In the momentum representation the wave function (5.2) will have the form

$$\Phi_n(p, t) = c'_n \exp\left(-\frac{i}{\hbar} \int_0^t \frac{[p - \delta(t) + \delta(t')]}{2M(t')} dt'\right) \exp\left(-\frac{1}{2} \eta^2 [p - \delta(t)]^2\right) \times \\ \times H_n(\eta[p - \delta(t)]), \quad (5.12)$$

where  $\eta = (m\hbar\omega)^{-1/2}$ ,  $c'_n = c'_0 / (2^n n!)^{-1/2}$ ,  $c'_0 = (\pi m \hbar \omega)^{-1/4}$ .

Since each  $\psi_n(x, t)$  (5.2) satisfies the time-dependent Schrödinger equation (2.1), the general solution  $\psi(x, t)$  of the time-dependent Schrödinger equation (2.1) is a superposition of all  $\psi_n(x, t)$ :

$$\psi(x, t) = \sum_n c_n \psi_n(x, t), \quad (5.13)$$

where  $c_n$  are arbitrary constants.

## 6. Unitary equivalence between a particle in a time-dependent linear potential and a free particle

Our goal in this section is to show that a problem of a particle moving in a time-dependent linear potential is unitarily equivalent to a free particle problem. More precisely we expect this equivalence to be valid whatever the time-dependence of the mass and in particular for constant one. This unitary equivalence is simple to exhibit.

Rewrite the Schrodinger equation (2.1) for a particle in the time-dependent linear potential as

$$\hat{S}_L(t) \psi_L(x, t) = 0, \quad \hat{S}_L(t) = i\hbar \partial_t + \frac{\hbar^2}{2M(t)} \partial_x^2 + F(t)x. \quad (6.1)$$

We apply now the unitary transformation

$$\hat{S}_F(t) = U_1^{-1}(t) \hat{S}_L(t) U_1(t) = i\hbar \partial_t + \frac{\hbar^2}{2M(t)} \partial_x^2, \quad (6.2a)$$

$$\psi_F(x, t) = U_1^{-1}(t) \psi_L(x, t). \quad (6.2b)$$

Then the equation (6.1) takes the form

$$\hat{S}_F(t) \psi_F(x, t) = 0, \quad (6.3)$$

i.e. one gets the Schrödinger equation for a free particle. The unitary operator satisfying the conditions (6.2) is equal to

$$U_1(t) = e^{\frac{i}{\hbar} [x\delta(t) - s_0(t)]} e^{-s_1(t) \partial_x}. \quad (6.4)$$

Let us write the solution of the Schrödinger equation (6.3) for the free particle as

$$\psi_F(x, t) = U_2(t) \psi_F(x, 0) \equiv e^{i\hbar s_2(t) \partial_x^2} \psi_F(x, 0). \quad (6.5)$$

From this we can get different solutions for the free Schrödinger equation (6.3).

From the comparison of (2.3), (6.4) and (6.5) follows that  $U = U_1 U_2$ . As follows from the definition, the operator  $U_1$  (6.4) transforms each solution of the free Schrödinger equation into the solution of the Schrödinger

equation for the linear potential, whereas the operator  $U_1^{-1}(t) = e^{s_1(t)\partial_x} e^{-\frac{i}{\hbar}[x\delta(t)-s_0(t)]}$  performs the reverse transformation. For example, the action of the operator  $U_1(x, t)$  on the function (3) of Ref. [1] yields the function (15) of the same work and vice versa. To show this, we rewrite the functions (3) and (15) of Ref. [1], respectively, as

$$\psi_F^{BB}(x, t) = Ai \left[ \frac{B}{\hbar^{2/3}} (x - B^3 s_2^2(t)) \right] \exp \left[ \frac{i}{\hbar} B^3 s_2(t) \left( x - \frac{2}{3} B^3 s_2^2(t) \right) \right] \quad (6.6)$$

and

$$\begin{aligned} \psi_L^{BB}(x, t) = Ai \left[ \frac{B}{\hbar^{2/3}} (x - s_1(t) - B^3 s_2^2(t)) \right] \exp \left[ \frac{i}{\hbar} B^3 s_2(t) \left( x - s_1(t) - \frac{2}{3} B^3 s_2^2(t) \right) \right] \times \\ \times \exp \left[ \frac{i}{\hbar} (x\delta(t) - s_0(t)) \right], \end{aligned} \quad (6.7)$$

where  $s_i(t)$  ( $i=0, 1, 2$ ) are given in (2.6). It is evident now that

$$\begin{aligned} \psi_F^{BB}(x, t) &= U_1^{-1}(t) \psi_L^{BB}(x, t), \\ \psi_L^{BB}(x, t) &= U_1(t) \psi_F^{BB}(x, t). \end{aligned} \quad (6.8)$$

## 7. CONCLUSION

We have studied Schrödinger equation for a particle with time-dependent mass moving in the time-dependent linear potential with the help of the evolution operator method.

Our analysis has shown that the key of solving the time-dependent Schrödinger equation is to find an evolution operator  $U(t)$  of the system. This is explained by the following facts: 1) In this case, unlike LR invariant method, there is no further problem of finding the time-dependent phase; 2) The general representation for the wave function in terms of the evolution operator  $\psi(t) = U(t)\psi(0)$  allows us to get all kinds of solutions of the Schrödinger equation, including those known in the literature, and with much less efforts; 3) Since the time-dependent Schrödinger equation has infinitely many solutions, it is impossible to exhaust all the solutions of the time-dependent system. Nevertheless, we can always find any solution with the required properties because the unitary operator  $U(t)$  preserves all the properties of the initial wave function. For example, if the initial wave function is square-integrable, then such will be  $\psi(x, t)$ ; 4) The evolution operator allows us to find not only solutions of the time-dependent Schrödinger equation, but also to construct all kinds of invariants. By using the evolution operator the explicit form of the operators (invariants) for the initial momentum and the initial coordinate  $\hat{p}_0(t)$  and  $\hat{x}_0(t)$  was found. The other invariants are expressed through them.

Our analysis also shows that a complete set of LR invariants for the system under consideration is not restricted by the linear and quadratic invariants. We have also shown that the problem of a particle in the linear

potential is unitary equivalent to that of a free particle. This fact is in agreement with a possible way of further generalization of the dynamical symmetry concept, according to which one can study a combination of several systems with different Hamiltonians and to construct operators that transform the wave functions, describing the states of all of these different systems, into each other [19].

We agree with the point of view expressed by Luan et al [6] that if we treat the driving force as a time-dependent gravity, then an observer in the “free-fall frame” will not be able to feel the gravity. As a result, the frame effectively became an inertial one. This provides a physical picture for the unitary transformation (6.2) we have performed.

Further, we note that by following Ref. [20], where the coherent states (CS)  $|z, t\rangle_F$  are constructed as the eigenstates of the annihilation operator (of the linear invariant) for a free particle, we can also construct the CS  $|z, t\rangle_L$  for the system under consideration. Of course the CS  $|z, t\rangle_L$  can also be obtained from  $|z, t\rangle_F$  with the help of the action of the unitary operator  $U_1(t)$ , i.e.  $|z, t\rangle_L = U_1(t)|z, t\rangle_F$ .

We feel that the present paper may stimulate other efforts to search for simpler treatments and solutions of similar problems which until now have been treated only by complicated methods.

It was pointed out in Ref. [6] that in order to get the GWP solution it is necessary to use non-Hermitian linear invariant. This fact is obvious, since it is well known that the eigenfunctions of the annihilation operator – CS are square-integrable. Using the evolution operator method, we can get the solutions of the Schrödinger equation, not only being in a class of the normalizable to one, or to  $\delta$ -function solutions describing the space of states of a quantum system. For example, the action of the evolution operator on the singular functions (on the initial wave functions), yields the singular solutions of the time-dependent Schrödinger equation as well.

### Appendix

1. Action of the operator  $e^{\alpha\partial_x^2}$  on a function  $f(x)$  can be defined as follows

$$e^{\alpha\partial_x^2} f(x) = \frac{1}{\sqrt{4\pi\alpha}} \int_{-\infty}^{\infty} e^{-\frac{(x-x')^2}{4\alpha}} f(x') dx' \quad (\text{A.1})$$

or

$$e^{\alpha\partial_x^2} f(x) = \sum_{n=0}^{\infty} \frac{\alpha^n}{n!} f^{(2n)}(x) \quad (\text{A.2})$$

Examples:

$$\text{a) } e^{\alpha\partial_x^2} e^{Ax} = e^{Ax + \alpha A^2}, \quad (\text{A.3})$$

$$\text{b) } e^{\alpha\partial_x^2} e^{-\lambda x^2} = (1 + 4\alpha\lambda)^{-1/2} \exp\left[-\lambda x^2 / (1 + 4\alpha\lambda)\right], \quad (\text{A.4})$$

$$\text{c) } e^{\alpha\partial_x^2} e^{-\lambda x^2 + \gamma x} = (1 + 4\alpha\lambda)^{-1/2} \exp\left[-(\lambda x^2 - \gamma x - \alpha\gamma^2) / (1 + 4\alpha\lambda)\right], \quad (\text{A.5})$$

$$\text{d) } e^{\alpha\partial_x^2} Ai(Bx) = e^{\alpha B^3 x + \frac{2}{3}\alpha^3 B^6} Ai(Bx + \alpha^2 B^4), \quad (\text{A.6})$$

$$\text{e) } e^{\alpha\partial_x^2} e^{\beta x} Ai(Bx) = e^{\varphi(x)} Ai(Bx + 2\alpha\beta B + \alpha^2 B^4), \quad (\text{A.7})$$

$$\varphi(x) = (\beta + \alpha B^3)x + \alpha\beta(\beta + 2\alpha B^3) + \frac{2}{3}\alpha^3 B^6. \quad (\text{A.8})$$

$$\text{f) } e^{\alpha\partial_x^2} e^{-\frac{1}{2}\lambda^2 x^2} H_n(\lambda x) = (1 + 2\alpha\lambda^2)^{-1/2} \exp\left[-\frac{\lambda^2 x^2}{2(1 + 2\alpha\lambda^2)}\right] \left(\frac{1 - 2\alpha\lambda^2}{1 + 2\alpha\lambda^2}\right)^{n/2} H_n\left(\frac{\lambda x}{\sqrt{1 - 4\alpha^2 \lambda^4}}\right). \quad (\text{A.9})$$

To derive the formula (A.9) we used the following integral [21]

$$\int_{-\infty}^{\infty} e^{-p(x-y)^2} H_n(cx) dx = \sqrt{\frac{\pi}{p}} \left(\frac{p - c^2}{p}\right)^{n/2} H_n\left(cy \sqrt{\frac{p}{p - c^2}}\right), \quad y, \operatorname{Re} p > 0. \quad (\text{A.10})$$

2. In some calculations the integral

$$J = \int_{-\infty}^{\infty} e^{ikx} Ai(a + \alpha x) Ai(b + \beta x) dx \quad (\text{A.11})$$

with the real parameters and  $\beta > \alpha$  could be useful. To evaluate this integral we use the following integral representation for the Airy function

$$Ai(x) = \frac{1}{2\pi} \int_{-\infty}^{\infty} e^{i(ux + \frac{1}{3}u^3)} du. \quad (\text{A.12})$$

As a result we obtain

$$J = e^{ia_0} Ai(a_1) / \sqrt[3]{\beta^3 - \alpha^3}, \quad (\text{A.13})$$

where

$$\begin{aligned} a_0 &= c_0 - \frac{c_1 c_2}{3c_3} + \frac{2c_2^3}{27c_3^2}, \quad a_1 = \frac{1}{\sqrt[3]{3c_3}} (c_1 - \frac{c_2^2}{3c_3}), \\ c_0 &= -\frac{k}{\beta} \left(b + \frac{k^2}{3\beta^2}\right), \quad c_1 = a - \frac{\alpha}{\beta} b - \frac{\alpha k^2}{\beta^3}, \\ c_2 &= -\frac{\alpha^2}{\beta^2} k, \quad c_3 = \frac{1}{3} (1 - \frac{\alpha^3}{\beta^3}), \end{aligned} \quad (\text{A.14})$$

$$a_1 = \frac{1}{\sqrt[3]{\beta^3 - \alpha^3}} (a\beta - b\alpha - \frac{\alpha\beta}{\beta^3 - \alpha^3} k^2)$$

- 
- [1] *M.V. Berry, N.L. Balazs.* Am. J. Phys. **47**, 1979, 264.
- [2] *M.A. Gregorio, A.S. de Castro.* Am. J. Phys. **52** 1984, 557.
- [3] *V.V. Dodonov, V.I. Manko, O.V. Shakhmistova.* Phys. Lett. A **102**, 1984, 295.
- [4] *I. Guedes.* Phys. Rev. A **63**, 2001, 034102.
- [5] *M. Feng.* Phys. Rev. A **64**, 2002, 034101.
- [6] *P.-G. Luan, C.-Sh. Tang.* Phys. Rev. A **71**, 2005, 014101.
- [7] *H. Bekkar, F. Benamura, M. Maamache.* Phys. Rev. A **68**, 2003, 016101.
- [8] *G. Dattoli, K. Zhukovcky.* Linear potential, Airy wavepackets and Airy transform (unpublished).
- [9] *H.R. Lewis, W.B. Riesenfeld.* J.Math.Phys. **10**, 1969, 1458.
- [10] *R. Feynman, A.R. Hibbs.* Quantum Mechanics and Path Integrals (McGraw-Hill, New York, 1965).
- [11] *F.J. Dyson.* Phys. Rev. **75**, 1949, 1736.
- [12] *I.A. Malkin, V.I. Manko.* Dynamical Systems and Coherent States of Quantum Systems (Nauka, Moscow, 1979) (in Russian).
- [13] *N.M. Atakishiyev, R.M. Mir-Kasimov, Sh.M. Nagiyev.* Theor.Math.Phys. **44**, 1981, 592.
- [14] *N.M. Atakishiyev, Sh.M. Nagiyev, K.B. Wolf.* Theor.Math.Phys. **114**, 1998, 322.
- [15] *Sh.M. Nagiyev, K.Sh. Jafarova.* Phys. Lett. A **377**, 2013, 747.
- [16] There is a printing error in formula (2) of Ref. [1], i.e.,  $\partial^2 x / \partial x^2$  should be replaced by  $\partial^2 \psi / \partial x^2$ . Other printing error in the formula (15) of Ref. [1] was indicated in Ref.[5].
- [17] There is a printing error in formula (12) of Ref. [7], i.e.,  $-i\hbar/2m$  should be replaced by  $-i/2m\hbar$ .
- [18] There is a printing error in formula (15) of Ref. [7], i.e., formula (15) of Ref.[7] should be replaced by formula (3.9) of the present work.
- [19] *V.V. Dodonov, V.I. Manko.* In Invariants and the Evolution of Nonstationary Quantum systems, edited by M.A. Markov, Proceedings of Lebedev Physics Institute, vol. 183 (Nova Science, Commack, NY, 1989) p. 132.
- [20] *V.G. Bagrov, D.M. Gitman, A.S. Pereyra.* Physics-Uspekhi, **184**, 2014, №9, p.961.
- [21] *A.P. Prudnikov, Yu.A. Brychkov, O.I. Marichev.* Integrals and Series, vol.2, Special Functions, Gordon and Breach. New York 1988.

Received: 11.01.2016

## COMPUTERIZED DEVICE FOR DETERMINATION OF MECHANICAL PROPERTIES OF POLYMERS. SILK AS A PARADIGM

A.H. AYDEMIROVA, R.B. ASLANOV, O.K. GASIMOV

*Institute of Physics of NASA,  
AZ-1143, Baku, Azerbaijan, H.Javid ave., 131  
E-mail: a030010@rambler.ru*

Silk is widely utilized in various areas of industry that includes textile, medical, technological and etc. Mechanical properties of silk play an important role in many applications. In this work, we built a computerized device that can measure time-dependent mechanical properties of polymers. Silk was chosen as a paradigm. The device uses optical detection for mechanical deformation that increases sensitivity and precision of measurements compared to that of the previously used one. The pulleys with variable diameters act as an amplifier for deformation scale. Deformation of silk threads and time to rupture in constant stress conditions were monitored in real time using a home-built LabView program. Variable detection rates, which can be as low as data/1ms, can be used in the program. Mechanical properties of two kinds of silk samples were measured. The device clearly differentiates mechanical properties of the samples. The device can be used to study time-dependent mechanical properties of various types of polymers in fibrous as well as film forms.

**Keywords:** silk, mechanical strength, "LabView" programming, mechanical time-dependent instrument

**PACS:** 82.35.Lr

### INTRODUCTION

Silk is a typical material produced by various insects, such as *bombyx mori*, *nelphia* and etc. Silk is being utilized as a textile and suture materials thousand years ago [1]. Silk consists of two parallel fibroin fibers and gummy part sericin that holds them together [2]. Sericin of silk has useful properties, such as resistant to oxidation, antibacterial, UV resistant and absorbing and releasing moisture easily [3,4].

Molecular organization of silk fibers determines their unique physical and chemical properties of fibroin, such as strength, toughness, stiffness and etc. [2].

Fibroin has a simple amino acid composition. Glycine (Gly), alanine (Ala) and serine (Ser) that have the smallest side chains, comprises about 82% of total amino acids.

Silk fibroin is used in diverse forms, such as gels, powder, membranes and fibers [1]. Silk fibroin shows very good biocompatibility, biodegradability and oxygen and water vapor permeability properties. Therefore, silk fibroin is very valuable material for biomedical, cosmetic and pharmaceutical industries.

Every kind of silk might have been evolved to perform the special task. Silk fibers from different insects show diverse physicochemical properties that can be attributed to their morphology [3].

One of the most important characteristics of silk is a mechanical strength, which is time-dependent by nature. Therefore, reliable measurements of time-dependent mechanical properties of polymers are very important.

Here we describe computerized device for such measurements. It can be used for various types of polymers in fibrous as well as film forms

### MATERIAL AND METHOD

The experiments were carried out with two kinds of silk samples using home-built laboratory instrument that is described below. Two kinds of silk cocoons were

tested. The samples with the 10 mm silk threads with the diameters of about 50-80  $\mu\text{m}$  were used.

*Computerized instrument to measure time-dependent deformation and time to rupture under constant mechanical stress conditions of polymers.*

Schematic diagram of the device is shown in fig. 1.

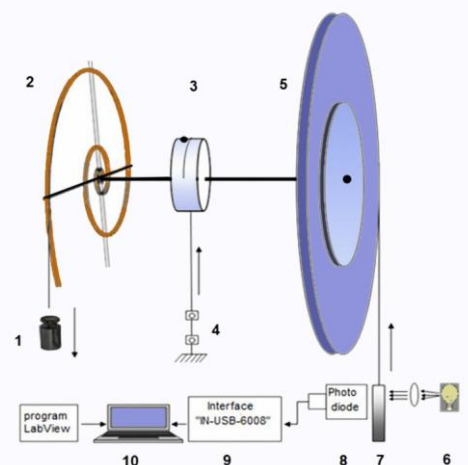


**Fig. 1** The computerized device to measure the time-dependent mechanical properties of polymer under constant stress conditions. 1 is load, 2 is varying arm pulley, 3 is transmitting block, 4 is sample, 5 is two radii disc, 6 is light source, 7 is linearly variable neutral density filter, 8 is photo diode, 9 is interface, 10 is computer.

For each load (1), varying arm pulley (2) provides a constant mechanical stress. Disk with two radiuses (5) permits increase deformation scales by a ratio of radiuses of disks (5) and (3). Linearly variable neutral density filter (LVNDF) fastened to the disk (5) provides optical detection of the sample deformation. The filter is compensated with an appropriate extra load that is not shown in the figure for simplicity. The vertical position of LVNDF and, therefore, deformation of the sample are determined by light intensity on a photodiode. Thus, the sample fixed by clamps undergoes deformation under



constant mechanical stress condition. Deformation rotates the disk (5) counter clockwise that lifts up the LVDNF. Consequently, light intensity passed via LVDNF and, therefore, output voltage of the diode is decreased. The method provides an accurate measurement of the deformation of the samples during the load time and under constant stress condition. Deformation values at various times are monitored on computer using the home-built LabView program. Sudden increase of the deformation determines the time to rupture (or mechanical lifetime) at constant mechanical stress.

The output values of the photodiode at various positions of LVDNF were calibrated with deformation in mm (See below). Analytical formula that describes this dependence was used in the LabView program to get original value for mechanical deformation in mm.

## RESULTS AND DISCUSSION

To determine time dependent deformation values, time to rupture of the samples under constant mechanical stress conditions, the output of photodiode depending on vertical position of LVDNF was calibrated. Because of optical linear density of LVDNF, this relation possesses exponential characteristic.

$$y = y_0 - A \cdot \exp\left(-\frac{x}{t}\right)$$

Dependence of vertical position of on output voltage of photodiode is shown in the fig. 2.

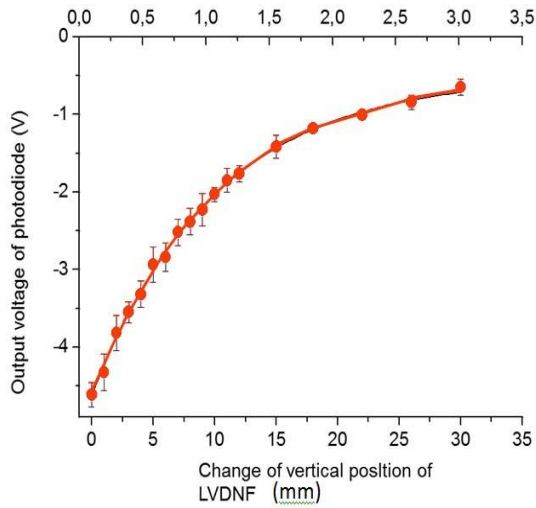


Fig. 2. Dependence of output voltage of photodiode on change vertical position of LVDNF. Solid circles are experimental data. Solid curve represents best fit of the experimental data to the exponential formula.

Data could be fit very well to the exponential formula with following parameters with,  $y_0 = -0.49$ ,  $A = 4.12$ , and  $t = 10.07$

This formula with the best fit parameters shown above was incorporated into the LabView program to show deformation in mm.

Dependences of the deformations of the silk threads on time at various constant mechanical stress values are shown in the fig. 3. Sudden increase in deformation

indicates the rupture of the silk thread. The deformation values do not depend on mechanical stress values. Besides that, very little changes in deformation values were observed during the lifetime of the samples. However, it is clear that the time to the rupture increases significantly in decreased mechanical stress values.

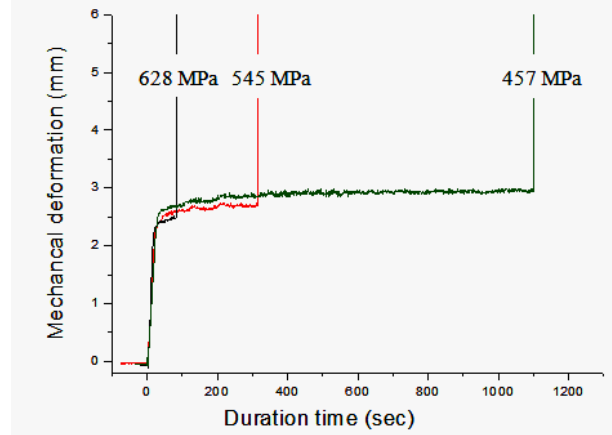


Fig. 3. Dependence of durability on mechanical stress for silk threads of 10 mm.

Consistent with other polymeric materials, logarithmic dependence is observed for the time to rupture and mechanical stress values (fig. 4).

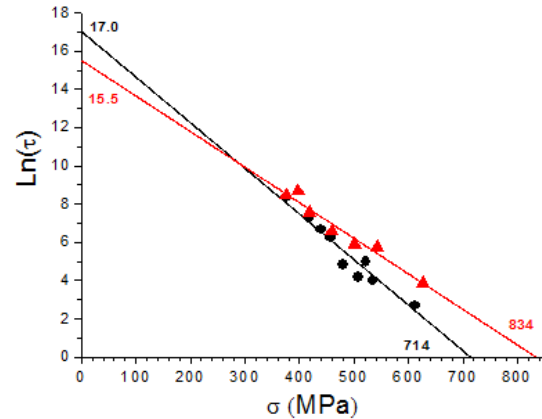


Fig. 4. Dependence of mechanical stress on durability (time to rupture).

This logarithmic dependence indicates that mechanical rupture is a process of Arrhenius type, goes through the energy of activation. This type of dependence observed for many polymeric materials has led to a formulation of thermo-fluctuation mechanism of destruction. At constant temperature, the dependence of time to rupture ( $\tau$ ) on applied constant mechanical stress ( $\sigma$ ) is given as below [5] :

$$\tau = Ae^{-\alpha\sigma} \quad (1)$$

where,  $A$  and  $\alpha$  - constant parameters. The Arrhenius nature of the formula (1) can be understood by the following consideration. Dependence of time to rupture on temperature at a given constant mechanical stress value is described by following equation [5,6]:

$$\tau = \tau_0 \exp\left(\frac{U_\sigma}{kT}\right) \quad (2)$$

$U_\sigma$  is an activation energy at constant mechanical stress values that can be described as

$$U_\sigma = U_0 - \gamma\sigma \quad (3)$$

Thus, mechanical stress ( $\sigma$ ) decreases the activation energy  $U_0$ . It follows that

$$\tau = \tau_0 \exp\left(\frac{U_0 - \gamma\sigma}{kT}\right) \quad (4)$$

where,  $\gamma$  is coefficient that depends on identity of the sample,  $k$  is the Boltzmann constant.

It can be easily recognized that the formulas (1) and (4) are equivalent via following definitions [5]:

$$A = \tau_0 \exp\frac{U_0}{kT} \quad (5)$$

$$\alpha = \frac{\gamma}{kT} \quad (6)$$

Thus mechanical rupture can be understood as thermal process. In thermal fluctuation, the molecules, the thermal energies of which are higher than  $(U_0 - \gamma\sigma)$  will be ruptured. Mechanical stress ( $\sigma$ ) just decreases the activation energy. The slope values of the graphs (fig. 4) indicate reveal structural information. Relatively higher value of 0.024 found for silk 1 (black data) compared to 0.019 of silk 2 (red data) indicates that mechanical stress more effectively decreases the energy of activation for mechanical rupture. The silk 2 can take higher stress value for one second 834 MPa versus 714 MPa, which indicates more mechanical strength (fig. 4). Thus, the device clearly can characterize mechanical-structural properties of various polymeric materials.

## CONCLUSION

A computerized device described above is suitable to measure time-dependent mechanical properties of polymers. Optical detection used in the system significantly increases both precision and accuracy of the measurements. Data registration time can be as low as 1 millisecond.

- 
- [1] So Hyun KIM, Young Sik NAM, Taek Seung LEE, and W. H. P. Silk Fibroin Nanofiber . Electrospinning, Properties, and Structure. Polym. J. **35**, 185–190 (2003).
  - [2] Chen, F., Porter, D. & Vollrath, F. Structure and physical properties of silkworm cocoons. J. R. Soc. Interface **9**, 2299–2308 (2012).
  - [3] Koh, L., Cheng, Y., Teng, C. & Khin, Y. Structures, mechanical properties and applications of silk fibroin materials. Prog. Polym. Sci. 1–25 (2015). doi:10.1016/j.progpolymsci.2015.02.001
  - [4] Mondal, M. K. T. and S. N. K. The silk proteins, sericin and fibroin in silkworm, Bombyx mori Linn., - a review. Casp. J. Environmental Sci. **5**, 63–76 (2007).
  - [5] Yumusak, C. & Alekberov, V. The effects of electrical discharge on the mechanical properties of Bombyx mori silk fibroin. Fibers Polym. **9**, 15–20 (2008).
  - [6] V.R. Regel, A.I. Slutsker, E.Y. Tomashevsky. Kineticheskaya priroda prochnosti tverdkh tel. (1974).

Received: 16.02.2016

## INTERNAL QUANTUM EFFICIENCY OF (11-22) InGaN/(In)GaN MULTIPLE QUANTUM WELLS

S. ABDULLAYEVA<sup>1,2</sup>, G. GAHRAMANOVA<sup>1,2</sup>, R. JABBAROV<sup>1,2</sup>, T. ORUJOV

<sup>1</sup>*Institute of Physics, Azerbaijan National Academy of Sciences, H. Javid av., 131, Baku 1143, Azerbaijan*

<sup>2</sup>*R&D Center for High Technologies Ministry of Communications and High Technologies of Azerbaijan*

Email: [gulnaz\\_gehremanova@hotmail.com](mailto:gulnaz_gehremanova@hotmail.com)

Temperature-dependent photoluminescence measurements and internal quantum efficiency of InGaN/(In)GaN multiple-quantum-well heterojunctions grown on (11-22) GaN/sapphire templates were investigated. The internal quantum efficiency of the InGaN quantum wells were calculated according to the temperature-dependent photoluminescence and ABC model.

**Keywords:** Quantum wells, semipolar (11-22) InGaN, internal quantum efficiency (IQE), ABC model.

**PACS:** 78.20.+e, 81.05.Ea, 81.10.+h

### 1. INTRODUCTION

InGaN/GaN multiple-quantum-well (MQW) based light emitting diodes (LEDs) and laser diodes (LDs) attract intense interests the performance of nitride based UV and visible LEDs and LDs [1, 2]. However, c-plane InGaN based QW LEDs suffer from the reduction in efficiency at high operating current density, i.e., “efficiency drop” [3–9]. Various possible explanations were proposed as the mechanism for the efficiency droop in high power nitride LEDs as follows: 1) decreased carrier localization at In-rich regions at high injection densities [1]; 2) carrier leakage [3]; 3) electron leakage [4]; 4) large Auger recombination at high carrier density [5, 6]; and 5) junction heating [7]. Specifically, the employment of thin layer of large bandgap material has been reported to have the potential of carrier leakage suppression and thus enhancement of IQE at high current density [8]. All this theoretical analysis have shown that the lattice-matched InGaN is the optimal material candidate for this thin barrier layer attributed to largest bandgap material available with lattice-matching to GaN. In the present work, we determine the IQE of GaInN/GaN MQWs in photoluminescence (PL) measurements; from the dependence of integrated PL intensity on excitation power and temperature dependent relative measurements [9–11].

### 2. EXPERIMENTS

The MOVPE growth was done in a commercial Aixtron-200/4 RF-S HT reactor using the standard precursors ammonia (NH<sub>3</sub>), trimethylgallium (TMGa), trimethylaluminum (TMAI), trimethylindium (TMIIn) and triethylgallium (TEGa). On the top of the (11-22) oriented GaN template, 2.8 nm thick InGaN quantum wells were grown at a temperature of about 720°C. The growth temperature for the 8 nm thick GaN barriers was 755°C [12].

### 3. METHODS AND RESULTS

Temperature dependent PL measurement have been calculated from low temperature to room temperature (14–300K) and the dominant wavelength was ~500 nm (fig.1,2). In comparison to the sample In<sub>0.15</sub>Ga<sub>0.85</sub>N/In<sub>0.01</sub>Ga<sub>0.99</sub>N with the In<sub>0.2</sub>Ga<sub>0.8</sub>N/GaN, a considerable higher PL intensity was observable at the low temperature and at 300K temperature this difference was lower. (fig.3). According to this PL measurements the IQE have been calculated by using a Eq.1 [15].

$$IQE = \frac{I_{Pl}(TK)}{I_{Pl}(14K)} \quad (1)$$

where,  $I_{Pl}$  is the PL intensity.

It was observed that at the low temperatures (11-22) In<sub>0.15</sub>Ga<sub>0.85</sub>N/In<sub>0.01</sub>Ga<sub>0.99</sub>N QWs demonstrated a higher IQE to compare with the (11-22) In<sub>0.2</sub>Ga<sub>0.8</sub>N/GaN QWs. For instance at 100K the IQE of In<sub>0.15</sub>Ga<sub>0.85</sub>N/In<sub>0.01</sub>Ga<sub>0.99</sub>N QWs and In<sub>0.2</sub>Ga<sub>0.8</sub>N/GaN QWs were 78% and 64% respectively (Fig.4). However, it can be easily seen that at the room temperature the IQE shows a higher value for In<sub>0.2</sub>Ga<sub>0.8</sub>N/GaN QWs in comparison with In<sub>0.15</sub>Ga<sub>0.85</sub>N/In<sub>0.01</sub>Ga<sub>0.99</sub>N QWs, 20% and 18% respectively (fig.3,4).

Next, we present a theoretical ABC model. According to the well-known ABC model, there are three main carrier-recombination mechanisms in a bulk semiconductor are Shockley–Read–Hall non-radiative recombination, expressed as  $A_n$ , bimolecular radiative recombination  $Bn^2$ , and Auger non-radiative recombination  $Cn^3$ , where A, B, and C are the proportional to  $n$ ,  $n^2$  and  $n^3$ , respectively, with  $n$  representing the carrier concentration [13].

Then, the IQE can be expressed as

$$IQE = \frac{Bn^2}{An + Bn^2 + Cn^3} \quad (2)$$

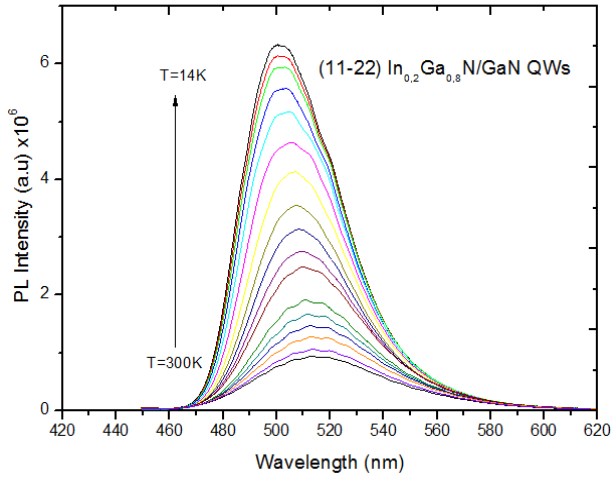


Fig. 1. The PL measurements of (11-22)  $\text{In}_{0.2}\text{Ga}_{0.8}\text{N}/\text{GaN}$  QWs.

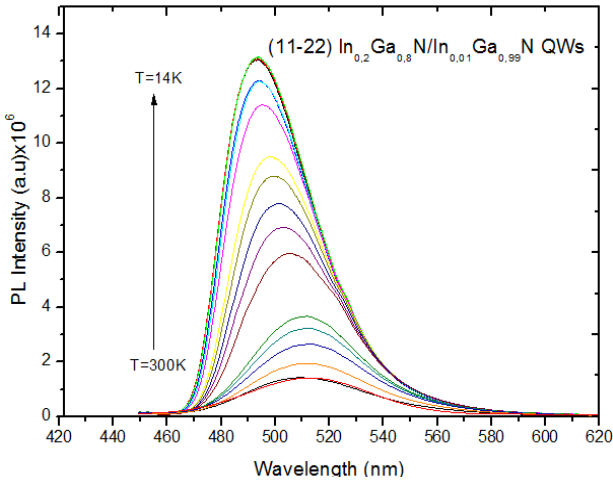


Fig. 2. The PL measurement of (11-22)  $\text{In}_{0.15}\text{Ga}_{0.85}\text{N}/\text{In}_{0.01}\text{Ga}_{0.99}\text{N}$  QWs.

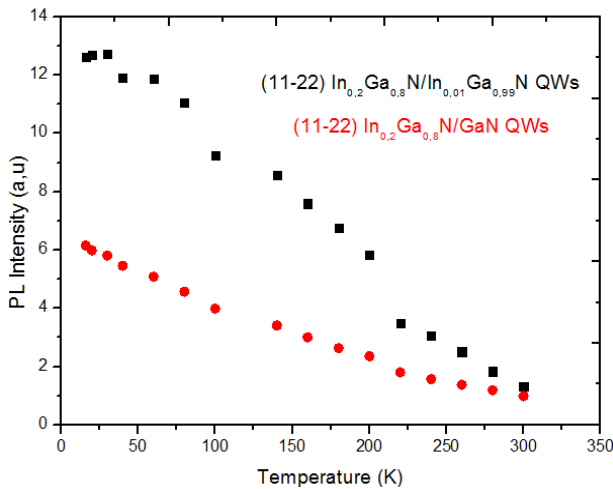


Fig. 3. The dependence of integrated PL intensity on temperature of (11-22)  $\text{In}_{0.15}\text{Ga}_{0.85}\text{N}/\text{In}_{0.01}\text{Ga}_{0.99}\text{N}$  QWs and  $\text{In}_{0.2}\text{Ga}_{0.8}\text{N}/\text{GaN}$  QWs.

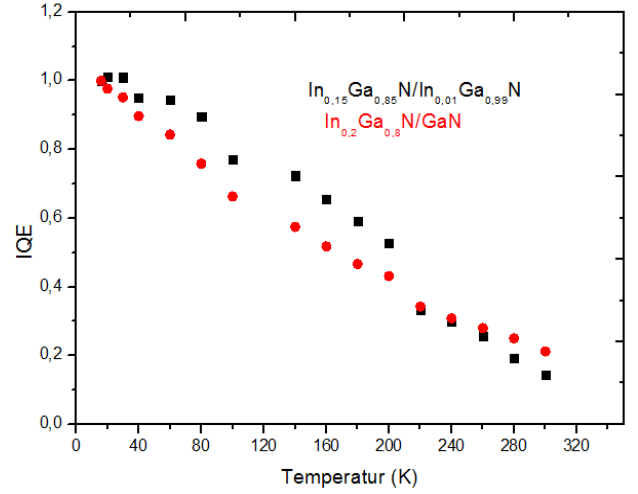


Fig. 4. The IQE of (11-22)  $\text{In}_{0.15}\text{Ga}_{0.85}\text{N}/\text{In}_{0.01}\text{Ga}_{0.99}\text{N}$  QWs and  $\text{In}_{0.2}\text{Ga}_{0.8}\text{N}/\text{GaN}$  quantum wells at different temperature.

The ratio of the integrated PL intensity  $I_{PL}$  and the power of the excitation source power  $P_{PL}$  is proportional to the IQE:

$$\frac{I_{PL}}{P_{PL}} = \eta_1 \frac{Bn^2}{An + Bn^2 + Cn^3} \quad (3)$$

with  $\eta_1$  denoting an unknown constant. The carrier generation rate  $G$  is proportional to the power of the excitation source. In steady state, the carrier generation rate is equal to the recombination rate,  $G = R$  and the IQE at steady state can be expressed as:

$$G = R = An + Bn^2 + Cn^3 \text{ or } G = \eta_2 P_{PL} \quad (4)$$

$$IQE = \frac{Bn^2}{G} \quad (5)$$

with  $\eta_2$  denoting an other unknown constant, the integrated PL intensity can be expressed as:

$$I_{PL} = \eta_2 Bn^2 \quad (6)$$

where  $\eta$  is a constant determined by the volume of the excited active region and the total collection efficiency of luminescence[14]. Combining Eq.3, 4, 5 and Eq.6, one can derive the relation between the parameters  $I_{PL}$  and  $P_{PL}$  as below[16]:

$$P_{PL} = A \sqrt{\frac{1}{B\eta_1\eta_2}} \sqrt{I_{PL}} + \frac{1}{\eta_1} I_{PL} + C \sqrt{\frac{\eta_2}{B^3\eta_1^3}} (\sqrt{I_{PL}})^3 \quad (7)$$

$P_{PL}$  is a cubic polynomial function of  $\sqrt{I_{PL}}$  with the constant term to be zero. By applying again a polynomial fit to the curve of  $P_{PL}$  versus  $\sqrt{I_{PL}}$ , one obtains the value of as the coefficient of the quadratic term with which the absolute value of  $\frac{1}{\eta_1}$  and the IQE can be calculated according to Eq.2.

The PL intensity of QWs are increased with increasing excitation source power (fig. 5). The IQE was obtained of (11-22)  $\text{In}_{0.2}\text{Ga}_{0.8}\text{N}/\text{GaN}$  QWs and (11-22)  $\text{In}_{0.15}\text{Ga}_{0.85}\text{N}/\text{In}_{0.01}\text{Ga}_{0.99}\text{N}$  QWs. At lower excitation power, it gets increased by 20 percentage points and reaches almost 100 %. Whereas the semi-polar InGaN/GaN layers show a constant IQE at higher excitation power, the efficiency of the InGaN/InGaN sample seems to decrease again (fig 6).

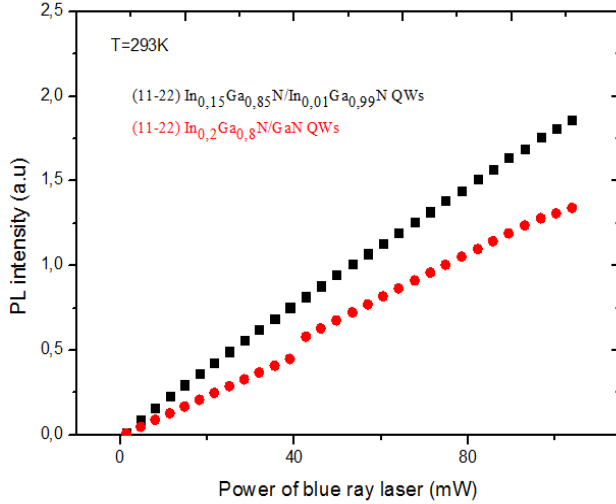


Fig. 5. The dependence of integrated PL intensity on temperature of (11-22)  $\text{In}_{0.15}\text{Ga}_{0.85}\text{N}/\text{In}_{0.01}\text{Ga}_{0.99}\text{N}$  (black) QWs and  $\text{In}_{0.2}\text{Ga}_{0.8}\text{N}/\text{GaN}$  QWs (red).

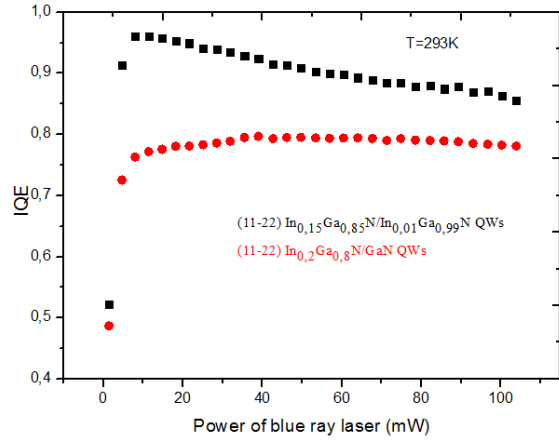


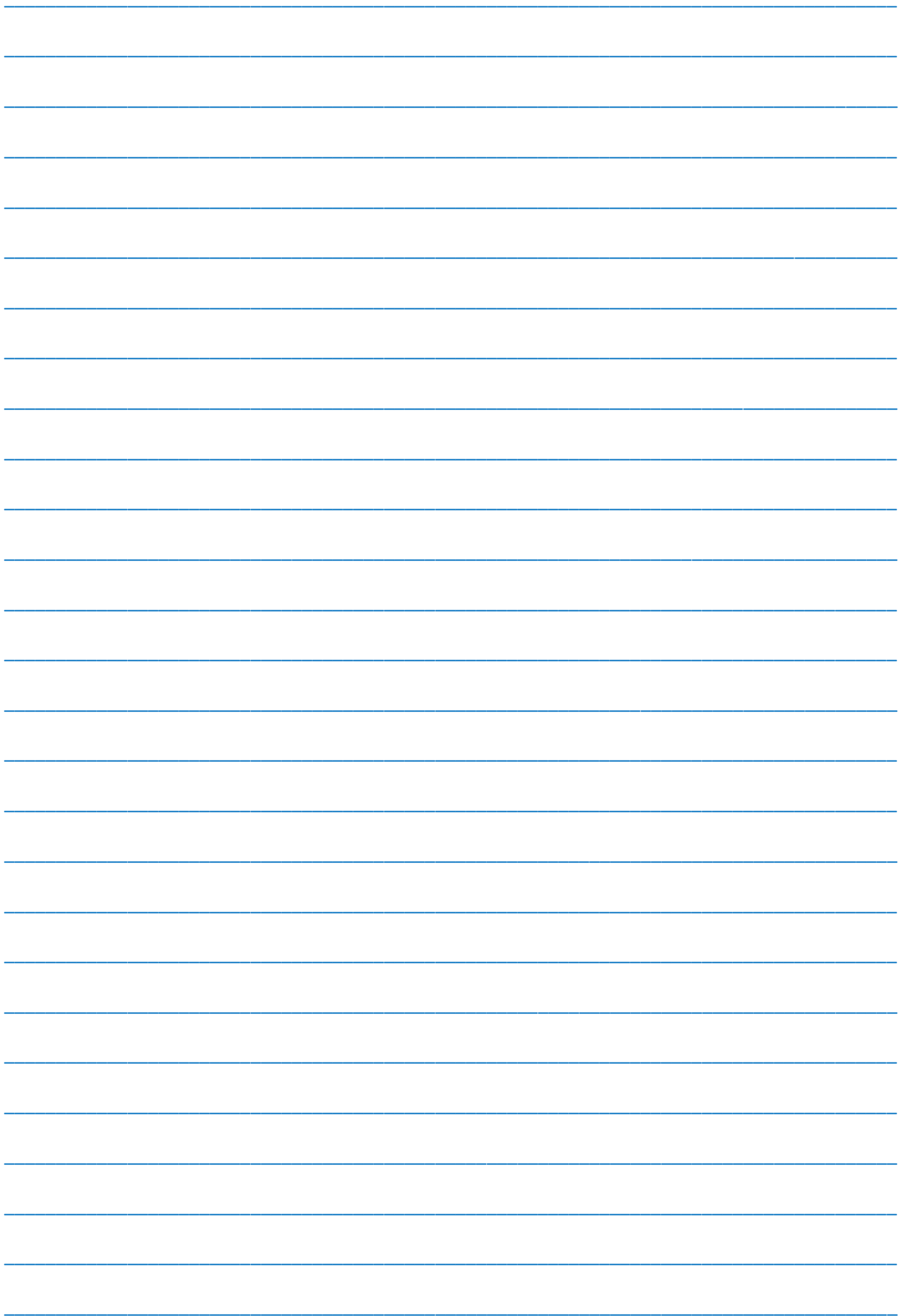
Fig. 6. The IQE at different excitation power.

#### 4. CONCLUSION

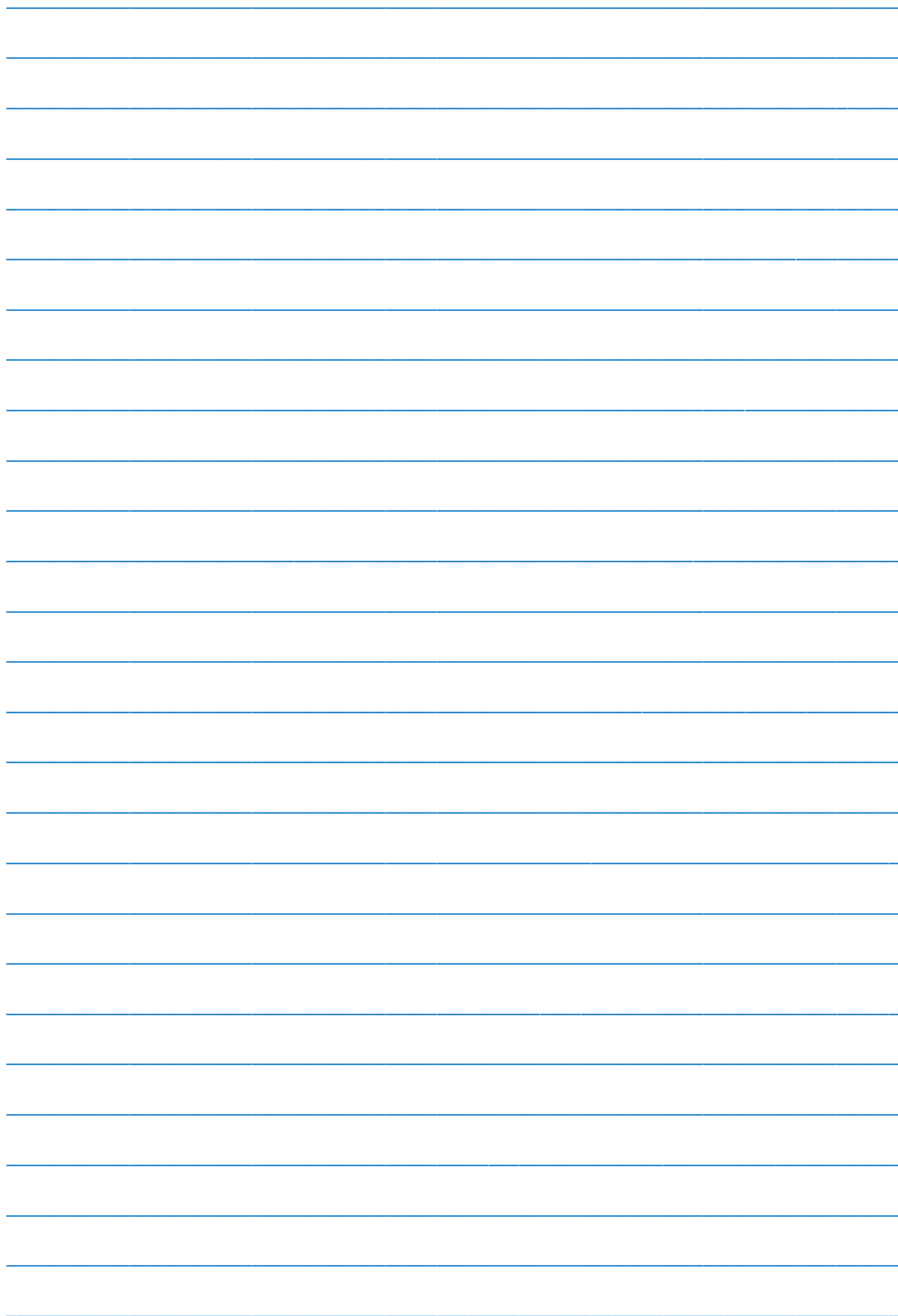
Semi-polar (11-22) InGaN/(In)GaN QWs were grown with 5 period 2.8nm InGaN QWs and 8nm barriers. According to the temperature dependent PL measurements it was observed that at the low temperatures (11-22)  $\text{In}_{0.15}\text{Ga}_{0.85}\text{N}/\text{In}_{0.01}\text{Ga}_{0.99}\text{N}$  QWs demonstrated a higher IQE to compare with the (11-22)  $\text{In}_{0.2}\text{Ga}_{0.8}\text{N}/\text{GaN}$  QWs. Using the ABC model the IQE was obtain of both samples. At lower excitation power, it gets increased by 20 percentage points and reaches almost 100 %. Whereas the semi-polar InGaN/GaN layers show a constant IQE at higher excitation power, the efficiency of the InGaN/InGaN sample seems to decrease again.

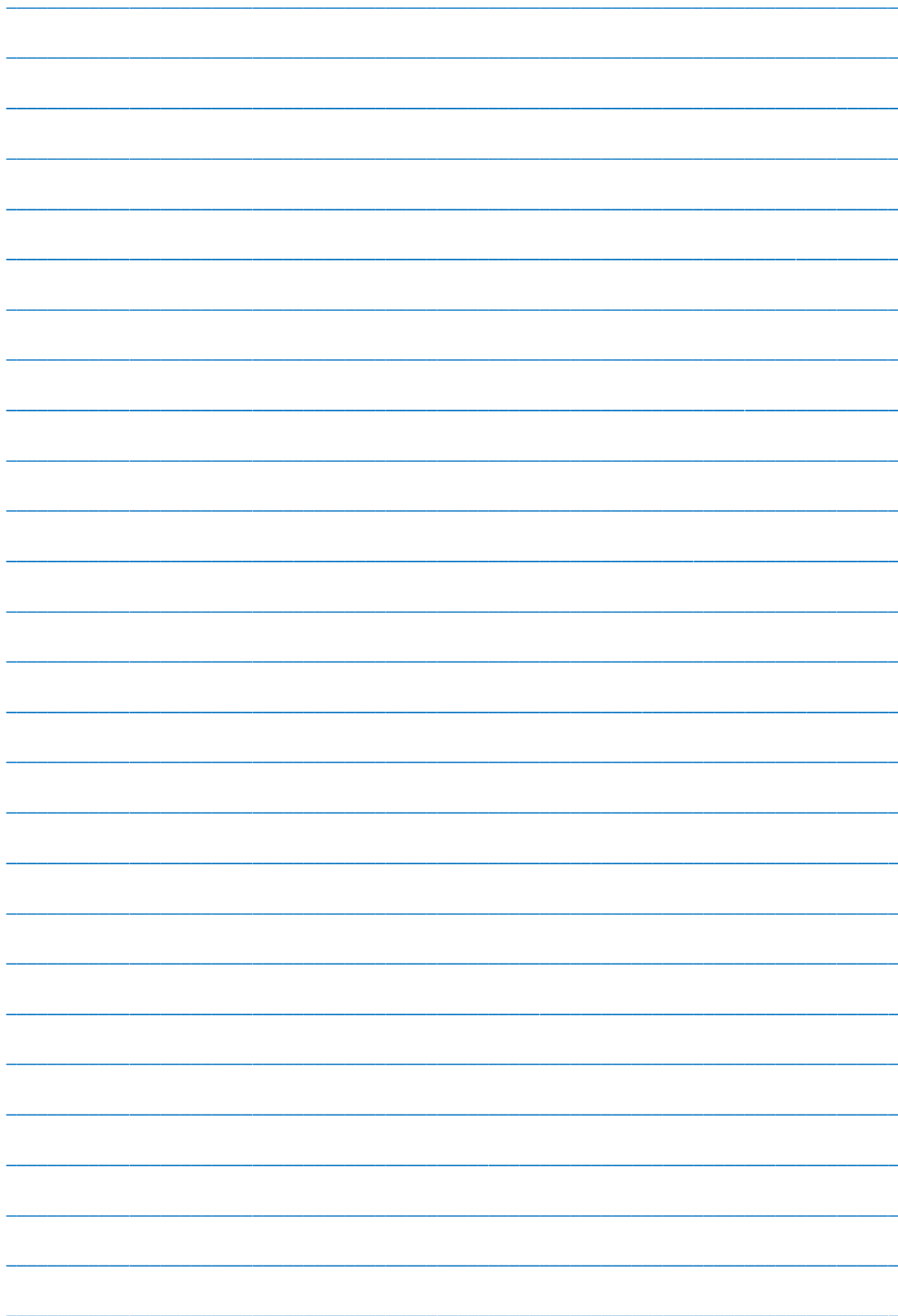
- [1] S.F. Chichibu, T. Azuhata, M. Sugiyama, T. Kitamura, Y. Ishida, H. Okumura, H. Nakanishi, T. Sota, and T. Mukai. J. Vacuum Sci. & Technol. B, vol. 19, pp. 2177–2183, Nov.-Dec. 2001.
- [2] X. Guo, Y.-L. Li, and E. F. Schubert. Appl. Phys. Lett., vol. 79, pp. 1936–1938, 2001.
- [3] M. F. Schubert, S. Chhajed, J.K. Kim, E.F. Schubert, D.D. Koleske, M.H. Crawford, S.R. Lee, A.J. Fischer, G. Thaler, and M.A. Banas. Appl. Phys. Lett., vol. 91, p. 231114, 2007.
- [4] X.F. Ni, Q. Fan, R. Shimada, U. Ozgur, and H. Morkoc. Appl. Phys. Lett., vol. 93, p. 171113, 2008.
- [5] Y.C. Shen, G.O. Mueller, S. Watanabe, N.F. Gardner, A. Munkholm, and M.R. Krames. Appl. Phys. Lett., vol. 91, p. 141101, Oct. 2007.
- [6] K.T. Delaney, P. Rinke, and C. G. V. d. Walle. Appl. Phys. Lett., vol. 94, p.191109, 2009.
- [7] A. Efremov, N. Bochkareva, R. Gorbunov, D. Lavrinovich, Y. Rebane, D. Tarkhin, and Y. Shreter. Semiconductors, vol. 40, pp. 605–610, 2006.
- [8] H. Zhao, G. Y. Liu, R. A. Arif, and N. Tansu. Solid-State Electron., vol. 54, pp. 1119–1124, Oct. 2010.
- [9] C.E. Martinez, N.M. Stanton, A.J. Kent, D.M. Graham, P. Dawson, M.J. Kappers, and C.J. Humphreys. J. Appl. Phys. 98, 053509, 2005.
- [10] S. Watanabe, N. Yamada, M. Nagashima, Y. Ueki, C. Sasaki, Y. Yamada, T. Taguchi, K. Tadatomo, H. Okagawa, and H. Kudo. Appl. Phys. Lett.83, 4906, 2003
- [11] D. Ding, S. R. Johnson, J. B. Wang, S.Q. Yu, and Y. H. Zhang. Proc. SPIE 6841, 68410D, 2007
- [12] Scholz F., Caliebe M., Gahramanova G., Heinz D., Klein M., Leute R.A., Meisch T., Wang J., Hocker M., and Thonke K. Phys. Status Solidi B 253, n.1, 13–22, 2015
- [13] Q. Dai, M.F. Schubert, M.H. Kim, J.K. Kim, E.F. Schubert, D.D. Koleske, M.H. Crawford, S.R. Lee, A.J. Fischer, G. Thaler, and M.A. Banas. Applied Physics Letters **94**, 111109, 2009
- [14] Hongping Zhao, Guangyu Liu, Jing Zhang, Ronald A. Arif, and Nelson Tansu. Journal of display technology, vol. 9, no. 4,2013
- [15] I.E. Titkov,; Sch. of Eng. & Appl. Sci., Aston Univ., Birmingham, UK ; Karpov, S.Yu. ; Yadav, A. ; Zerova, V.L. Quantum Electronics, IEEE journal, Vol. 50 , 0018-9197, p. 911-920, 2014
- [16] Junjun Wan, Tobias Meisch and Ferdinand Scholz. Phys. Status Solidi B:253, n. 01, p.174-179, 2016.

Received: 08.02.2016











[www.physics.gov.az](http://www.physics.gov.az)

*CONTENTS*


---

1.	Technology of aluminum deep purification by zone melting method using ultrasonic waves <b>A.I. Nadjafov, R.R. Babayeva</b>	3
2.	IR spectra of (Ni, Zn) ferrite micropowders <b>Sh.N. Aliyeva, A. Kerimova, T.R. Mehdiyev</b>	6
3.	Optimization of synthesis condition for high quality carbon nanotubes <b>S.H. Abdullayeva, N.N. Musayeva, C. Frigeri, A.B. Huseynov, R.B. Jabbarov, R.F. Hasanov</b>	11
4.	Vacancy formation energy for charged and neutral states in $\text{TlInS}_2$ <b>G.S. Orudzhev, N.A. Ismayilova</b>	15
5.	Investigation of phase transition in $\text{Cu}_4\text{Te}_{1.5}\text{Se}_{0.5}$ solid solution by high-temperature roentgenography method <b>N.A. Aliyeva, G.G. Guseynov, G.M. Agamirzoyeva, T.R. Mehdiyev</b>	19
6.	Thermorecombination waves extrinsic semiconductors with two types of charge carries <b>E.R. Gasanov, A.V. Islamzade</b>	23
7.	Elementary processes in kinetics of mechanical failure of PP-PELD polymer compositions <b>I.K. Aliyeva, P.B. Asilbeyli, T.M. Veliyev, E.S. Safiyev, A.A. Khadiyeva</b>	28
8.	Structural investigations of $\text{Zn}_{1.5}\text{In}_3\text{Se}_6$ polytype 3R by means of new electron-diffraction rotation methods <b>M.G. Kyazumov, L.V. Rustamova</b>	31
9.	Reexamination a time-dependent linear potential in the quantum mechanics <b>Sh.M. Nagiyev, K.Sh. Jafarova, A.I. Kazimova</b>	34
10.	Computerized device for determination of mechanical properties of polymers. Silk as a paradigm <b>A.H. Aydemirova, R.B. Aslanov, O.K. Gasymov</b>	46
11.	Internal quantum efficiency of (11-22) $\text{InGaN}/(\text{In})\text{GaN}$ multiple quantum wells <b>S. Abdullayeva, G. Gahramanova, R. Jabbarov, T. Orujov</b>	49